U.S. ?

UNIVERSITY OF MICHIGAN
JUL 22 1955
CHEMISTRY LIBRARY

Journal of Research

of the

National Bureau of Standards

MAY 1955

VOLUME 54 NUMBER 5

U. S. DEPARTMENT OF COMMERCE
Sinclair Weeks, Secretary
NATIONAL BUREAU OF STANDARDS
A. V. Astin, Director

MAY • 1955
VOLUME • 54
NUMBER • 5

JOURNAL OF RESEARCH

of the

NATIONAL BUREAU OF STANDARDS

PERIODICALS OF THE NATIONAL BUREAU OF STANDARDS

(Published monthly)

The National Bureau of Standards is engaged in fundamental and applied research in physics, chemistry, mathematics, and engineering. Projects are conducted in fifteen fields: electricity and electronics, optics and metrology, heat and power, atomic and radiation physics, chemistry, mechanics, organic and fibrous materials, metallurgy, mineral products, building technology, applied mathematics, data processing systems, cryogenic engineering, radio propagation, and radio standards. The Bureau has custody of the national standards of measurement and conducts research leading to the improvement of scientific and engineering standards and of techniques and methods of measurement. Testing methods and instruments are developed; physical constants and properties of materials are determined; and technical processes are investigated.

JOURNAL OF RESEARCH

The Journal presents research papers by authorities in the specialized fields of physics, mathematics, chemistry, and engineering. Complete details of the work are presented, including laboratory data, experimental procedures, and theoretical and mathematical analyses. Annual subscription: domestic, $4.00; foreign, $5.25.

TECHNICAL NEWS BULLETIN

Summaries of current research at the National Bureau of Standards are published each month in the Technical News Bulletin. The articles are brief, with emphasis on the results of research, chosen on the basis of their scientific or technologic importance. Lists of all Bureau publications during the preceding month are given, including Research Papers, Handbooks, Applied Mathematics Series, Building Materials and Structures Reports, Miscellaneous Publications, and Circulars. Each issue contains 12 or more two-column pages; illustrated. Annual subscription: domestic, $1.00; foreign, $1.35.

BASIC RADIO PROPAGATION PREDICTIONS

The Predictions provide the information necessary for calculating the best frequencies for communication between any two points in the world at any time during the given month. The data are important to all users of long-range radio communications and navigation, including broadcasting, airline, steamship, and wireless services, as well as to investigators of radio propagation and ionosphere. Each issue, covering a period of one month, is released three months in advance and contains 16 large pages, including pertinent charts, drawings, and tables. Annual subscription: domestic, $1.00; foreign, $1.25.

Order all publications from the Superintendent of Documents
U. S. Government Printing Office, Washington 25, D. C.

The printing of this publication has been approved by the Director of the Bureau of the Budget, May 12, 1953.

Journal of Research of the National Bureau of Standards Vol. 54, No. 5, May 1955 Research Paper 2586

Astigmatism of Skew Pencils in Optical Systems Containing Toric Surfaces[1]

Walter Weinstein[2]

A method is described for tracing skew rays through toric refracting surfaces and for determining the astigmatism of pencils around these rays.

1. Introduction

Toric refracting surfaces are used chiefly in two classes of optical systems, spectacle lenses, and anamorphotic photographic and projection objectives. In spectacles the toric surfaces are arranged to correct the axial astigmatism of the eye, and in anamorphotic systems two or more toric (possibly cylindrical) surfaces are included to give stigmatic imagery with different magnifications in different directions in the image plane.

When the axial pencil is refracted by a toric,[3] some astigmatism is introduced; if a pencil is incident obliquely, either centrally or eccentrically, astigmatism of different magnitude is introduced. It is therefore desirable in the case of both types of optical systems mentioned above to determine the astigmatism of obliquely incident pencils, in order to assess the imagery in the outer parts of the field. This is the problem which was studied in the work to be described.

The problem arose in connection with spectacle lenses and may be outlined as follows:

Figure 1 shows front and side views of a spectacle lens with toric surface; O is the center of the lens, C is the center of rotation of the eye, and P_1, P_2, P_3 are points of incidence of the chief rays of oblique pencils. Let the meridian and equatorial sections of the toric be, respectively, in the vertical and horizontal planes OP_1 and OP_3. Then the problem for chief rays passing through the axis and through P_1 and P_3 is trivial. The chief ray itself can be traced by the ordinary ray-tracing formulas for meridian rays and spherical surfaces, and the astigmatism can be determined by the usual methods for close sagittal and tangential fans, with the slight difference that the curvatures of the refracting surface in the two directions are not equal (see eq (8)).

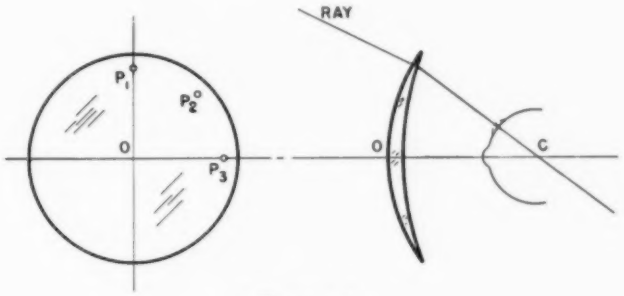

FIGURE 1.

If, however, the point of incidence of the chief ray does not lie in the meridian or equatorial section, as, for example, P_2 in figure 1, the problem becomes more complicated. In the first place, even if the incident chief ray intersects the axis of the system, the refracted ray in general does not, so that the chief ray must for complete generality be considered to be skew; thus the first part of the problem is to trace a skew chief ray through the toric.

[1] The work described in this paper was carried out while the author was a guest worker in the Optical Instruments Section, National Bureau of Standards, from January to July 1954.

[2] Present address: Imperial College, London, England.

[3] In what follows, "toric surface" will be abbreviated to "toric."

Second, with oblique incidence as at any of the points P_1, P_2, or P_3, astigmatism is produced in the refracted pencil for two reasons: (a) because the angle of incidence is not zero, as in the ordinary case of spherical surfaces, and (b) because the refracting surface has two different principal curvatures at the point of incidence. In the case of P_2 the principal directions of the astigmatism due to (a) are parallel and normal to the plane of incidence of the chief ray, i. e., approximately parallel and perpendicular to line, OP_2; the principal directions of the astigmatism due to (b) are, however, approximately parallel to OP_1 and OP_3. Thus the resultant astigmatic pencil will have its focal lines in some intermediate directions, and the determination of these directions further complicates the calculation.[4] It follows that the formal distinction between sagittal and tangential directions can no longer be made; however, for the configurations of chief ray and toric that occur in spectacle lenses the rotation of the focal lines is unlikely to be above 10°, so that there is little difficulty in relating the results for skew chief rays to those for rays in either principal section.

The results of such calculations would constitute a survey of the astigmatism of a toric spectacle lens at all obliquities and azimuths. They would help to answer questions such as the following: What is the best bending of a toric spectacle lens? What range of powers can be manufactured with a common back curvature without departing appreciably from the best bending? Is there any advantage in making both surfaces of a spectacle lens toric in shape? Such questions as these arise in the design of so-called best-form spectacle lenses. These have previously been designed on the basis of computations in the two principal sections only.[5] [6] However, an illustration is given by Henker [6] showing the quality of an image produced by a pencil outside the principal sections of a typical sphero-toric lens of the Punktal best-form series; this illustration suggests that there is still room for improvement in the image. The work to be described makes it possible to compute the imagery by skew pencils and so determine whether any improvements can in fact be made.

Section 2 is a recapitulation of the properties of astigmatic pencils that are required in deriving the astigmatism equations. In section 3 the equations of a toric are given, and other properties are derived, in section 4 the ray-tracing equations for the skew chief ray are derived, and in section 5 the astigmatism formulas are derived. Section 6 deals with the forms in which the input data must be given. In section 7 the mode of presentation of the results is discussed, the results of a numerical example are given, and the possible uses of the computation are discussed.

2. Astigmatic Pencils

For the purposes of the present paper a pencil will be considered to be made up of a narrow bundle of rays originating from a point in the object and surrounding a chief, or principal, ray, together with all the corresponding wave fronts. The wave fronts are surfaces of constant optical path length from the object point, and the rays are normals to the wave fronts.

With a rectangular coordinate system with the x axis along the principal ray, the equation of the wave front passing through the origin will take the form

$$x = c_{20}y^2 + c_{11}yz + c_{02}z^2 + \text{terms of higher degree in } y \text{ and } z; \tag{1}$$

linear terms are absent because the yz plane must be tangent to the wave front at the origin. Also it is possible to rotate the y and z axes about the x axis, so that the coefficient of the term in yz vanishes when the equation takes the form

$$x = \tfrac{1}{2}(c_r y^2 + c_s z^2) + \text{higher-degree terms.} \tag{2}$$

[4] This difficulty does not arise for points on the principal sections of the toric, such as P_1 and P_3, because then the directions of the focal lines are known by symmetry to be parallel and perpendicular to the principal sections.

[5] H. H. Emsley and W. Swaine, Ophthalmic lenses, 6th ed. (London, 1951).

[6] O. Henker, Introduction to the theory of spectacles (Translated by R. Kanthack) (Jena, 1924).

Effects depending on terms in y and z of higher degree than the second will be neglected. To this degree of approximation it is easily shown that all rays of the pencil; i. e., normals to the surface (2) intersect one line through the point $(1/c_r, 0, 0)$ parallel to the z axis and another line through the point $(1/c_s, 0, 0)$ parallel to the y axis, these being the two astigmatic focal lines. Thus this approximation takes account of astigmatism but not of aberrations such as spherical aberration and coma, which depend on higher powers of the aperture of the pencil. The coefficients have the significance that c_r is the curvature of the section of the wave front by the xy plane and c_s, that by the xz plane

Some results from differential geometry are now required. At any nonsingular point P of a surface the normal curvature (i. e., the curvature of the section of the surface by a plane through the normal) has a maximum and a minimum for two section planes which are at right angles to each other; furthermore, if these two planes, together with the tangent plane at P, are taken as coordinate planes, the equation of the surface in the neighborhood of P takes the form of eq (2), that is, the yz term is absent. The maximum and minimum normal curvatures are called the principal curvatures, and the corresponding section planes meet the tangent plane at P in lines that lie along the principal directions at P. Thus the principal directions are along the y and z axes for eq (2).

It is also known, by Euler's theorem, that if a normal section plane makes an angle α with the xy plane, the curvature in this section is

$$c(\alpha) = c_r \cos^2 \alpha + c_s \sin^2 \alpha. \tag{3}$$

From this it follows that these quantities are required to characterize an astigmatic pencil:

(a) The direction of the chief ray; this will be given by a unit vector, $\boldsymbol{Q}$, with components X, Y, and Z.

(b) The principal curvatures, c_r and c_s, of the wave front at a point on the chief ray.

(c) The principal directions on the wave front; these will be given by unit vectors $\boldsymbol{R}$ and $\boldsymbol{S}$, and from the above it follows that $\boldsymbol{Q}$, $\boldsymbol{R}$, and $\boldsymbol{S}$ are all perpendicular to each other.

3. Toric Surface

A toric surface is generated by the rotation of a circle (the generating circle, abbreviated to G. C.) about an axis in its plane but not passing through its center, as in figure 2, a and b. In optical applications the lens surface is, of course, only a cap-shaped portion of the whole surface, roughly centered on the point A. Such a surface is alined with a centered system of spherical surfaces by making the optical axis lie in the normal plane to the rotation axis, which contains the center of the G. C. The optical axis then meets the toric in the pole A.

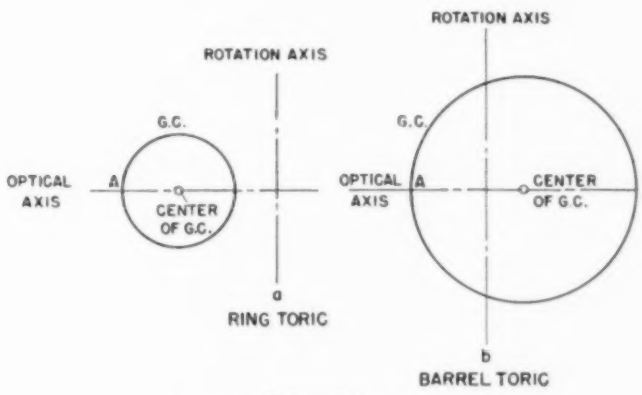

FIGURE 2.

The toric refracting surface has different powers (in the optical sense) in different sections through the optical axis: the powers are determined by the radius of the G. C. for the section in the plane of the rotation axis and by the distance from A to the rotation axis for that perpendicular to it; these are known as the meridian and equatorial sections, respectively.

It can be seen that for given powers in the principal sections there are two possible forms of toric surface: the radius of the G. C. can be either less than or greater than the distance from A to the rotation axis, the two forms being known, respectively, as ring- and barrel-shaped torics. The ring form seems to be used almost exclusively for spectacles in commercial practice, but to the best of the author's knowledge, this is merely because more rings than barrels of given curvatures can be surfaced in one operation, not for any optical advantage. The possibility of improvements from the use of the barrel shape seems not to be considered in the literature on "best-form" series.

3.1. Equations of the Toric

One can write down the equation of the toric surface by taking rectangular coordinate axes with the origin at the pole A of the toric refracting surface (fig. 3), the x axis along the optical axis, the y axis parallel to the rotation axis, and the z axis in the equatorial plane. Let r_y and r_z be the radii of curvature in the xy and xz sections, respectively. Take angular parameters, θ and ϕ, as in the figure, so that θ is the longitude and ϕ the latitude of a point on the toric. Then the parametric equations of the toric are

$$\left.\begin{aligned} x &= r_z - (r_z - r_y + r_y \cos\phi)\cos\theta \\ y &= r_y \sin\phi \\ z &= (r_z - r_y + r_y \cos\phi)\sin\theta \end{aligned}\right\}. \tag{4}$$

It can be seen that eq (4) represent a ring- or a barrel-shaped toric according as r_y is less than or greater than r_z in absolute magnitude,[7] in both cases the rotation axis is parallel to the y axis. When the rotation axis is to be parallel to the z axis the equations are obtained be interchanging y and z throughout, including subscripts, in eq (4); this is true also for the equations in the remainder of section 3.

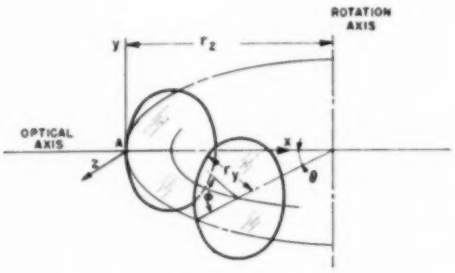

FIGURE 3.

An explicit equation can be obtained by eliminating θ and ϕ in eq (4) and solving for x:

$$x = r_z \pm \{[r_z - r_y \pm (r_y^2 - y^2)^{1/2}]^2 - z^2\}^{1/2}. \tag{5}$$

The ambiguous signs are due to the fact that there are four (possibly complex) values of x for any given y and z, since the toric is a quartic surface; the required solution is that which tends to zero as y and z tend to zero, so that the correct signs are, respectively, minus and plus. When these are inserted the result is unsuitable for numerical computation when y and

[7] Provided r_y and r_z have the same sign, which is generally the case in spectacle lenses.

z are small compared to r_y and r_z, as is generally the case. This difficulty can be circumvented by transforming the equation by means of conjugate surds in the usual way and using curvatures instead of radii, giving

$$x=\frac{F}{G\{G+[G^2-c_zF]^{1/2}\}}, \tag{6}$$

where

$$F=c_zz^2G^2+2c_yy^2G-c_y^2c_zy^4,\ G=1+(1-c_y^2y^2)^{1/2}.$$

In this form the equation of the toric is suitable for numerical computation with all relevant ranges of the variables.

3.2. Principal Directions and Curvatures

In considering the refraction of an astigmatic pencil through a toric, it is necessary to know the shape of the toric in the neighborhood of the point of incidence. Thus, as in section 2, the following are required:

(a) The direction of the normal at the point of incidence; this will be given by a unit vector, $\boldsymbol{U}$, with components, λ, μ, and ν.

(b) The principal curvatures, c_v and c_w, at the point of incidence.

(c) The principal directions at the point of incidence; these will be specified by unit vectors, $\boldsymbol{V}$ and $\boldsymbol{W}$, and again the vectors, $\boldsymbol{U}$, $\boldsymbol{V}$, and $\boldsymbol{W}$, form a trirectangular system. These quantities are easily determined for a current point (x,y,z); if the toric has principal curvatures, c_y and c_z, at the origin and if the rotation axis is parallel to the y axis, as in section 2.1, the results are

$$U=(\cos\phi\cos\theta,-\sin\phi,-\cos\phi\sin\theta), \tag{7}$$

$$\phi=\arcsin c_yy,\theta=\arcsin\frac{Gc_zz}{G-c_zc_yy^2},$$

$$\left.\begin{aligned} c_v&=c_y\\ c_w&=\frac{Gc_z\cos\phi}{G-c_yc_zy^2}\end{aligned}\right\}, \tag{8}$$

$$\left.\begin{aligned} V&=(\sin\phi\cos\theta,\ \cos\phi,-\sin\phi\sin\theta)\\ W&=(\sin\theta,\quad 0,\quad \cos\theta)\end{aligned}\right\}. \tag{9}$$

4. Tracing the Skew Chief Ray

Using the quantities defined in sections 2 and 3.2, the problem can be stated as follows:

Given $\boldsymbol{Q}$ and the coordinates of a point on the chief ray, the coordinates (x,y,z) of the point of incidence of the ray on the toric must be determined (transfer process); next $\boldsymbol{U}$ at the point of incidence must be found and $\boldsymbol{Q}'$, the direction of the refracted chief ray, determined (refraction process). The quantities c_r, c_s, $\boldsymbol{R}$, and $\boldsymbol{S}$ will be known for the incident pencil and c_v, c_w, $\boldsymbol{V}$, and $\boldsymbol{W}$ can be found, since the point of incidence is known; from these the quantities c_r', c_s', $\boldsymbol{R}'$, and $\boldsymbol{S}'$ for the refracted pencil must be determined. This last, the astigmatism calculation, will be described in section 5.

4.1. Transfer Process

The transfer problem is that of finding the intersection of a straight line with a toric. A direct approach would require the solution of an algebraic equation of the fourth degree; this would be a laborious process, so an iterative method was adopted. In addition to the general advantage of iterative methods, that mistakes in the early stages of the calculation are automatically eliminated at the cost of extra computing time, this method also selects the correct solution from the four possible solutions.

Let P_1 be a point on the ray near the required point of incidence.[8] A point P_1' on the toric is found with the same y and z coordinates and the tangent plane T_1 at P_1' is determined. The next approximation P_2 is taken at the intersection of the ray with T_1 and the cycle $P_2 \rightarrow P_2' \rightarrow T_2 \rightarrow P_3$ . . . repeated until the coordinates of P_n and P_{n+1} are the same to the required number of significant figures. These are then the coordinates of P, the point of incidence.

Let the coordinates of P_n be (x_n, y_n, z_n) and those of P_n' be (x_n', y_n, z_n); then x_n' is obtained by substituting y_n and z_n in eq (6). The equation of the plane T_n is $\lambda_n(x-x_n')+\mu_n(y-y_n)+\nu_n(z-z_n)=0$,
where λ_n, μ_n, and νz are given by eq (7) so that x_{n+1} is given by

$$\left.\begin{aligned} x_{n+1} &= x_n + \delta_n \\ \delta_n &= \frac{\lambda_n X (x_n' - x_n)}{\lambda_n X + \mu_n Y + \nu_n Z} \end{aligned}\right\}. \tag{10}$$

Also,

$$\left.\begin{aligned} y_{n+1} &= y_n + \frac{Y}{X}\delta_n \\ z_{n+1} &= z_n + \frac{Z}{X}\delta_n \end{aligned}\right\}. \tag{11}$$

This completes the iterative cycle. It can be shown to be a second-order iteration,[9] that is, δ_{n+1} is of order of magnitude δ_n^2, so that it is always rapidly convergent, provided the initial approximation is good enough.

The choice of the initial approximation depends on the available means of computation. If a high-speed automatic-computing engine is available, P_1 may be taken as the point where the ray meets the yz plane. Let (x_0, y_0, z_0) be the coordinates of the point P_0 where the ray leaves the previous refracting surface (or the entrance pupil);[10] then P_1 is given by

$$\left.\begin{aligned} x_1 &= 0, \\ y_1 &= y_0 - x_0 Y/X, \\ z_1 &= z_0 - x_0 Z/X \end{aligned}\right\}. \tag{12}$$

Starting from this approximation, some four or five iterations would probably be needed to reach a result correct to six significant figures.

If a desk computing machine is to be used, an appreciable saving in computing time can be effected by using an improved first estimate. It usually happens that chief rays directed at the same pupil have already been traced in the meridian and equatorial sections of the toric. Let the x coordinates of their points of incidence be x_y and x_z, respectively. The section of the toric by a plane through the x axis and making an angle α with the xy plane is approximately a circle, of curvature $c_y\cos^2\alpha + c_x \sin^2\alpha$, so that a chief ray in this plane will meet the toric at a point of which the x coordinate is approximately $x_y \cos^2\alpha + x_z \sin^2\alpha$. This P_1 is given by

$$\left.\begin{aligned} x_1 &= x_y \cos^2\alpha + x_z \sin^2\alpha \\ y_1 &= y_0 + (x_1 - x_0)Y/X \\ z_1 &= z_0 + (x_1 - x_0)Z/X \end{aligned}\right\}. \tag{13}$$

This approximation is usually so good that only one iteration is needed to obtain six significant figures in the coordinates of P.

[8] The method of obtaining P_1 will be discussed below.
[9] W. Weinstein, Proc. Phys. Soc. (London) [B] **65**, 731 (1952).
[10] (x_0, y_0, z_0) are taken in the coordinate system referring to the current surface, not that on which P_0 lies.

4.2. Refraction Process

The refraction calculation for the chief ray can now be carried out by well-known formulas. Let I be the angle of incidence and n the index of refraction of the medium in which the ray is incident; let primes denote corresponding refracted quantities. Then

$$\cos I = \boldsymbol{Q}\cdot\boldsymbol{U}, \tag{14}$$

$$\cos I' = +\left(1-\frac{n^2}{n'^2}(1-\cos^2 I)\right)^{1/2}, \tag{15}$$

$$\boldsymbol{Q}' = \frac{n}{n'}\boldsymbol{Q}+\left(\cos I' - \frac{n}{n'}\cos I\right)\boldsymbol{U}. \tag{16}$$

In eq (14) $\boldsymbol{Q}\cdot\boldsymbol{U}$ denotes the scalar product of $\boldsymbol{Q}$ and $\boldsymbol{U}$.

This completes the refraction process and the coordinates and direction cosines of the refracted ray are then used, with a suitable change of origin, for the incident ray at the next surface.

5. Astigmatism Calculation

In order to determine equations giving $\boldsymbol{R}'$, $\boldsymbol{S}'$, c_r', and c_s', in terms of known quantities, a general theorem is required. Referring to figure 4, let P be the point of incidence of the chief ray, and let B be the point of incidence of another ray of the pencil. Suppose the incident and refracted wavefronts through P to be constructed, and let the ray through B meet these in C' and C'', respectively.[11] Then, since the optical path length between two wavefronts is the same along any ray, it follows that $n\overline{C'B}=n'\overline{C''B'}$ or, if $\overline{C'B}$ is denoted by q,

$$\Delta(nq)=0.$$

Here the symbol, Δ, means that the refracted quantity minus the incident quantity is to be taken. This relationship is true for any relative positions of P and B and for any shape of refracting surface.

In order to use eq (17) for the present purpose, q and q' will be expressed in terms of the coordinates of the point B on the refracting surface and the parameters of the wavefronts. The resulting equation will give the normal curvature of the refracted wavefront in a section containing the ray through B and by differentiating with respect to the azimuth of B the maximum and minimum normal curvatures, c_r' and c_s', can be found. The same calculation gives the directions $\boldsymbol{R}'$ and $\boldsymbol{S}'$ of the principal sections.

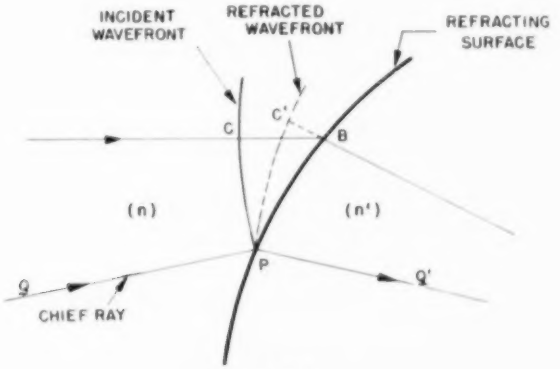

FIGURE 4.

[11] The part of the refracted wavefront shown in the diagram is virtual.

5.1. Normal Curvature of the Refracted Wavefront

Figure 5 shows the refracting surface near the point of incidence. Let P and B have the same significance as in figure 4 and let $\boldsymbol{V}$ and $\boldsymbol{W}$ be the unit vectors along the principal directions. Let B_1 be the projection of B on the $\boldsymbol{VW}$ plane; let α be the angle between PB_1 and $\boldsymbol{V}$, and let PB be denoted by p. Then the position of B relative to P will be given by p and α as coordinates.

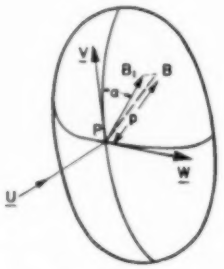

FIGURE 5.

In order to express q in terms of p and α, use is made of the fact that CB in figure 4 is a normal to the wavefront. It is found (see section 5.1, a) that

$$q=p(\boldsymbol{Q}\cdot\boldsymbol{V}\cos\alpha+\boldsymbol{Q}\cdot\boldsymbol{W}\sin\alpha)+\tfrac{1}{2}p^2\{\boldsymbol{Q}\cdot\boldsymbol{U}(c_v\cos^2\alpha+c_w\sin^2\alpha)-c_r(\boldsymbol{R}\cdot\boldsymbol{V}\cos\alpha+\boldsymbol{R}\cdot\boldsymbol{W}\sin\alpha)^2 -c_s(\boldsymbol{S}\cdot\boldsymbol{V}\cos\alpha+\boldsymbol{S}\cdot\boldsymbol{W}\sin\alpha)^2\}+\text{terms in } p^3, \tag{18}$$

and there is a similar equation for q'.

Substituting for q and q' in eq (17),

$$p\Delta n(\boldsymbol{Q}\cdot\boldsymbol{V}\cos\alpha+\boldsymbol{Q}\cdot\boldsymbol{W}\sin\alpha)+\tfrac{1}{2}p^2\Delta n\{\boldsymbol{Q}\cdot\boldsymbol{U}(c_v\cos^2\alpha+c_w\sin^2\alpha)-c_r(\boldsymbol{R}\cdot\boldsymbol{V}\cos\alpha+\boldsymbol{R}\cdot\boldsymbol{W}\sin\alpha)^2 -c_s(\boldsymbol{S}\cdot\boldsymbol{V}\cos\alpha+\boldsymbol{S}\cdot\boldsymbol{W}\sin\alpha)^2\}+\text{terms in } p^3=0. \tag{19}$$

Only terms up to and including the square of p are taken since, as explained in section 2, this degree of approximation takes account of astigmatism.

Equation 19 holds good for any values of p and α, so that the coefficients of different powers of p may be separately equated to zero. If this is done, the linear term yields an alternative form of Snell's law and on putting $\alpha=0$ and $\pi/2$, the equations

$$\Delta[n\boldsymbol{Q}\cdot\boldsymbol{V}]=\Delta[n\boldsymbol{Q}\cdot\boldsymbol{W}]=0 \tag{20}$$

are obtained. These could serve as a check on the refraction calculation.

Equating the coefficient of p^2 in eq (19) to zero and dividing through by $1-(\boldsymbol{Q}'\cdot\boldsymbol{V}\cos\alpha+\boldsymbol{Q}'\cdot\boldsymbol{W}\sin\alpha)^2$ gives

$$\frac{c_r'(\boldsymbol{R}'\cdot\boldsymbol{V}\cos\alpha+\boldsymbol{R}'\cdot\boldsymbol{W}\sin\alpha)^2+c_s'(\boldsymbol{S}'\cdot\boldsymbol{V}\cos\alpha+\boldsymbol{S}'\cdot\boldsymbol{W}\sin\alpha)^2}{1-(\boldsymbol{Q}'\cdot\boldsymbol{V}\cos\alpha+\boldsymbol{Q}'\cdot\boldsymbol{W}\sin\alpha)^2}$$

$$=\frac{nc_r(\boldsymbol{R}\cdot\boldsymbol{V}\cos\alpha+\boldsymbol{R}\cdot\boldsymbol{W}\sin\alpha)^2+nc_s(\boldsymbol{S}\cdot\boldsymbol{V}\cos\alpha+\boldsymbol{S}\cdot\boldsymbol{W}\sin\alpha)^2+(c_v\cos^2\alpha+c_w\sin\alpha)\Delta n\boldsymbol{Q}\cdot\boldsymbol{U}}{n'[1-(\boldsymbol{Q}'\cdot\boldsymbol{V}\cos\alpha+\boldsymbol{Q}'\cdot\boldsymbol{W}\sin\alpha)^2]}. \tag{21}$$

Now the equation of the refracted wavefront can be shown to be

$$x=\frac{[c_r'(\boldsymbol{R}'\cdot\boldsymbol{V}\cos\alpha+\boldsymbol{R}'\cdot\boldsymbol{W}\sin\alpha)^2+c_s'(\boldsymbol{S}'\cdot\boldsymbol{V}\cos\alpha+\boldsymbol{S}'\cdot\boldsymbol{W}\sin\alpha)^2](x^2+y^2)}{(\boldsymbol{R}'\cdot\boldsymbol{V}\cos\alpha+\boldsymbol{R}'\cdot\boldsymbol{W}\sin\alpha)^2+(\boldsymbol{S}'\cdot\boldsymbol{V}\cos\alpha+\boldsymbol{S}'\cdot\boldsymbol{W}\sin\alpha)^2},$$

taking the x, y, and z axes along $\boldsymbol{Q}'$, $\boldsymbol{R}'$, and $\boldsymbol{S}'$. Thus the left hand side of eq (21) is $c'(\alpha)$, the

normal curvature of the refracted wavefront in a section containing the point B with angular coordinate α on the toric.

a. Derivation of Equation (18)

Two auxiliary coordinate systems are required, each with origin at P, the point of incidence. One, the x, y, z system, has its axes respectively parallel to $\boldsymbol{Q}$, $\boldsymbol{R}$, and $\boldsymbol{S}$; the other, x', y', and z' has its axes parallel to $\boldsymbol{U}$, $\boldsymbol{V}$, and $\boldsymbol{W}$. The two are related by the equations

$$x=(\boldsymbol{Q}\cdot\boldsymbol{U})x'+(\boldsymbol{Q}\cdot\boldsymbol{V})y'+(\boldsymbol{Q}\cdot\boldsymbol{W})z', \quad y=(\boldsymbol{R}\cdot\boldsymbol{U})x'+(\boldsymbol{R}\cdot\boldsymbol{V})y'+(\boldsymbol{R}\cdot\boldsymbol{W})z',$$
$$z=(\boldsymbol{S}\cdot\boldsymbol{U})x'+(\boldsymbol{S}\cdot\boldsymbol{V})y'+(\boldsymbol{S}\cdot\boldsymbol{W})z'.$$

If the point B on the refracting surface (fig. 4) has polar coordinates (p, α), its coordinates in the x', y', z' system are [12]

$$x'=\tfrac{1}{2}(c_r\cos^2\alpha+c_w\sin^2\alpha)p^2+O(p^4), \quad y'=p\cos\alpha+O(p^3), \quad z'=p\sin\alpha+O(p^3).$$

Let B have coordinates (u, v, w) in the (x, y, z) system; then

$$u=\tfrac{1}{2}(\boldsymbol{Q}\cdot\boldsymbol{U})(c_r\cos^2\alpha+c_w\sin^2\alpha)p^2+(\boldsymbol{Q}\cdot\boldsymbol{V})p\cos\alpha+(\boldsymbol{Q}\cdot\boldsymbol{W})p\sin\alpha+O(p^3),$$

$$v=(\boldsymbol{R}\cdot\boldsymbol{V})p\cos\alpha+(\boldsymbol{R}\cdot\boldsymbol{W})p\sin\alpha+O(p^2),$$

$$w=(\boldsymbol{S}\cdot\boldsymbol{V})p\cos\alpha+(\boldsymbol{S}\cdot\boldsymbol{W})p\sin\alpha+O(p^2).$$

Let (x, y, z) be the coordinates of C in the x, y, z system, so that

$$x=\tfrac{1}{2}(c_ry^2+c_sz^2)+O(y^3,z^3).$$

The direction cosines of the normal to the wavefront at C are, to the approximation $O(y^2,z^2)$, $(1,-c_ry,-c_sz)$, and since CB is a ray, or wavefront normal, it follows that

$$u=x+q, \quad v=y-c_ryq, \quad w=z-c_szq.$$

There are now enough relations to eliminate x, y, z, u, v, and w. The resulting equation involving p, q, and α can be solved for q, remembering that terms which are $O(p^3,q^3)$ can be neglected, since only astigmatism is in question. The solution for q is found to be eq (18).

5.2. The Principal Curvatures of the Refracted Wavefront

The principal curvatures c_s' and c_r' are the maximum and minimum values of $c'(\alpha)$. Since all quantities on the right of eq (21) are known with the exception of α, c_r' and c_s' can be obtained in the usual way by differentiating with respect to α and equating to zero. Let

$$a=\tfrac{1}{2}[nc_r((\boldsymbol{R}\cdot\boldsymbol{V})^2+(\boldsymbol{R}\cdot\boldsymbol{W})^2)+nc_s((\boldsymbol{S}\cdot\boldsymbol{V})^2+(\boldsymbol{S}\cdot\boldsymbol{W})^2)+(c_r+c_w)\Delta n\boldsymbol{Q}\cdot\boldsymbol{U}], \tag{22}$$

$$b=\tfrac{1}{2}[nc_r((\boldsymbol{R}\cdot\boldsymbol{V})^2-(\boldsymbol{R}\cdot\boldsymbol{W})^2)+nc_s((\boldsymbol{S}\cdot\boldsymbol{V})^2-(\boldsymbol{S}\cdot\boldsymbol{W})^2)+(c_r+c_w)\Delta n\boldsymbol{Q}\cdot\boldsymbol{U}], \tag{23}$$

$$c=nc_r(\boldsymbol{R}\cdot\boldsymbol{V})(\boldsymbol{R}\cdot\boldsymbol{W})+nc_s(\boldsymbol{S}\cdot\boldsymbol{V})(\boldsymbol{S}\cdot\boldsymbol{W}), \tag{24}$$

$$d=\tfrac{1}{2}((2-(\boldsymbol{Q}'\cdot\boldsymbol{V})^2-(\boldsymbol{Q}'\cdot\boldsymbol{W})^2), \tag{25}$$

$$e=\tfrac{1}{2}((\boldsymbol{Q}'\cdot\boldsymbol{V})^2-(\boldsymbol{Q}'\cdot\boldsymbol{W})^2), \tag{26}$$

$$f=-(\boldsymbol{Q}'\cdot\boldsymbol{V})(\boldsymbol{Q}'\cdot\boldsymbol{W}). \tag{27}$$

The equation for α is

$$(ea-bd)\sin^2\alpha+(dc-af)\cos^2\alpha=(bf-ec),$$

[12] The expression $O(p^n)$ used in this section denotes terms of order of magnitude p^n.

and the two solutions are

$$\alpha_1=\frac{\gamma-\beta}{2},\quad \alpha_2=\frac{\pi}{2}-\frac{\gamma+\beta}{2}, \tag{28}$$

where [13]

$$\beta=\arcsin\frac{dc-af}{+[(ea-bd)^2+(dc-af)^2]^{1/2}} \tag{29}$$

and

$$\gamma=\arcsin\frac{bf-ec}{[(ea-bd)^2+(dc-af)^2]^{1/2}}. \tag{30}$$

The values of c_s' and c_r' are then obtained by putting $\alpha=\alpha_1$ and α_2 in the right hand side of eq (21).

5.3. Principal Directions on the Refracted Wavefront

In figure 6, let P be the point of incidence, PB the refracting surface, and PC' the refracted wavefront. Let $\boldsymbol{Q}'$ be the unit vector along the chief ray and let $C'B$ be another ray of the astigmatic pencil. Let the projections of C' and B on the tangent planes to the wavefront and refracting surface be C_1' and B_1 respectively. Then $\boldsymbol{V}\cos\alpha+\boldsymbol{W}\sin\alpha$ is a vector in the direction PB_1, so that a unit vector in the direction PC_1' is given by

$$\frac{\boldsymbol{V}\cos\alpha+\boldsymbol{W}\sin\alpha-\boldsymbol{Q}'(\boldsymbol{Q}'\cdot\boldsymbol{V}\cos\alpha+\boldsymbol{Q}'\cdot\boldsymbol{W}\sin\alpha)}{[1-(\boldsymbol{Q}'\cdot\boldsymbol{V}\cos\alpha+\boldsymbol{Q}'\cdot\boldsymbol{W}\sin\alpha)^2]^{1/2}}. \tag{31}$$

Thus, the vectors $\boldsymbol{R}'$ and $\boldsymbol{S}'$ are obtained by putting $\alpha=\alpha_1$ and α_2 in the expression (31). It should be noticed that in this derivation it was assumed that the points C' and B lie on a plane through $\boldsymbol{Q}'$, i. e., that the ray through C' intersects the chief ray. This is not strictly true in general, but the error depends on terms in the equation of the wavefront of the third degree in the aperture, so that astigmatism calculations are not affected.

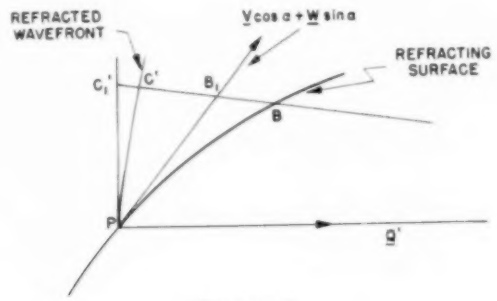

FIGURE 6.

This completes the refraction computation for astigmatism. The $\boldsymbol{R}'$ and $\boldsymbol{S}'$ vectors are transferred without change to be the new $\boldsymbol{R}$ and $\boldsymbol{S}$ vectors at the next surface. In order to transfer the curvatures the distance L between surfaces along the chief ray is required; this is easily found to be $(x-x_0)/X$, in the notation of section 4.1. Then the new curvatures are given by

$$\left.\begin{aligned}(1/c_r)_{+1}&=(1/c_r)'-L\\(1/c_s)_{+1}&=(1/c_s)'-L\end{aligned}\right\}. \tag{32}$$

[13] Of the possible solutions for β, one must be chosen which satisfies

$$\beta=\arccos\frac{ea-bd}{+[(ea-bd)^2+(dc-af)^2]^{1/2}}+\text{a multiple of } 2\pi.$$

6. Input Data

If the wavefront incident on the first surface is not already astigmatic, some arbitrary directions for $\boldsymbol{R}$ and $\boldsymbol{S}$ must be assigned. Similarly if a refracting surface is spherical, directions for $\boldsymbol{V}$ and $\boldsymbol{W}$ must be assigned.

These pairs of vectors must form trirectangular sets with $\boldsymbol{Q}$ and $\boldsymbol{U}$, respectively, but subject to this condition they can be chosen to suit computational convenience. Choosing $\boldsymbol{R}$ to be coplanar with $\boldsymbol{Q}$ and the y axis, it is found that

$$\left.\begin{aligned} \boldsymbol{R} &= \frac{(-XY, 1-Y^2, -YZ)}{(1-Y^2)^{1/2}} \\ \boldsymbol{S} &= \frac{(Z, 0, -X)}{(1-Y^2)^{1/2}} \end{aligned}\right\}. \tag{33}$$

Since Y^2 is rarely greater than 0.1, the vectors so defined are well determined numerically. In a similar way $\boldsymbol{V}$ and $\boldsymbol{W}$ can be taken as

$$\left.\begin{aligned} \boldsymbol{V} &= \frac{(-\lambda\mu, 1-\mu^2, -\mu\nu)}{(1-\mu^2)^{1/2}} \\ \boldsymbol{W} &= \frac{(\nu, 0, -\lambda)}{(1-\mu^2)^{1/2}} \end{aligned}\right\}. \tag{34}$$

It is also necessary to choose between ring and barrel shapes for the toric surfaces. In the equations of section 3.1 the rotation axis of the toric is taken parallel to the y axis and the toric will be ring or barrel shape according as c_y is numerically geater or less than c_z. Thus, if it is required to have a barrel shape with $|c_y| > |c_z|$ or a ring shape with $|c_y| < |c_z|$, the equations must be changed so that the rotation axis is parallel to the z axis. This can be done by interchanging y and z in the symbols and subscripts of eq (4) to (8), inclusive, as mentioned in section 3.1.

7. Presentation of Results

7.1. A Numerical Example

In the application to spectacle lenses the results are presented in the form of a diagram giving the astigmatism of a number of pencils and the directions of the principal sections on the wave front. An example is given in figure 7.

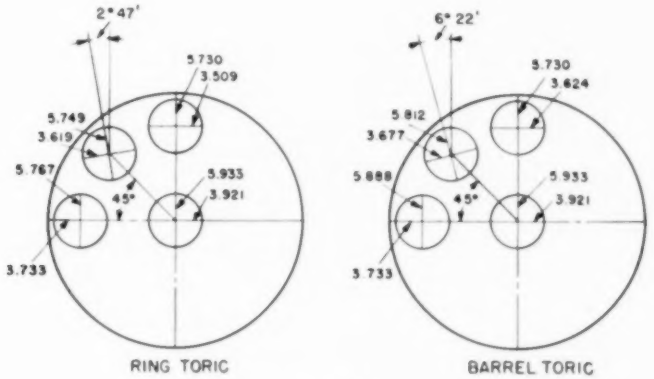

FIGURE 7.

The wavefront curvatures are marked on the appropriate sections, in diopters with respect to the vertex sphere. The apparent rotation of the principal sections of the wavefront can be found from the consideration that the vertical plane containing the chief ray contains the direction which is apparently vertical to the eye. This plane is the plane through $\boldsymbol{Q}$ and parallel to the y axis. From this it can be shown that the angle, A, through which the $\boldsymbol{R}$ and $\boldsymbol{S}$ vectors appear to be turned is given by

$$\tan A = \frac{r_2}{s_2}, \tag{35}$$

where r_2 and s_2 are the y components of $\boldsymbol{R}$ and $\boldsymbol{S}$.

The nominal powers of the lens in this example were 5.5 diopters in the vertical section and 3.62 diopters in the horizontal section. The curvatures of the front (toric) surface were $+0.2199$ cm^{-1} and $+0.1839$ cm^{-1}, that of the back (spherical) surface was -0.1147 cm^{-1}, the center thickness was 0.48 cm and the refractive index was taken as 1.523. The chief ray was made to intersect the axis 27 mm behind the lens at an angle of 30°. The results for both ring and barrel shapes with the same nominal curvatures are given.

Computations have also been done on the prescriptions of a number of lenses and measurements have been made on these with a vertex power measuring instrument. The agreement is satisfactory within the limits of experimental error.

7.2. Discussion

In the numerical example given above the rotation of the focal lines in intermediate azimuths is negligible; this may be expected to be the case for all but very heavily cylindrical spectacle lenses of best-form type. It can also be seen that the variation of astigmatism over the field is less for the barrel than for the ring shape (0.14 D and 0.21 D, respectively). This, of course, is not a general conclusion, but it suggests that further computation would be desirable. It is possible that for heavy cylinders a considerable improvement might be obtained by using barrel shapes, but this might be outweighed by the increased manufacturing costs. This would depend also on visual tolerances for astigmatism; it seems that more experimental work is required on this subject.

A different question is that of the accuracy with which tories are produced. The principal curvatures check within the limits of accuracy of a lens gage, and the sagittal curvatures change or remain constant along the meridan or equatorial sections, respectively, to the same accuracy. However, this may not be enough to prove that the lens surface is a true toric to an accuracy which justifies the calculations for chief rays in intermediate azimuths. The mode of manufacture is certainly such as to produce a very close approximation to a toric if the surfacing machine really acts in the intended manner, but it is quite possible that distortions and nonuniform wear in the tools and machine parts may cause departures from the toric shape. No measurements other than checks on the principal curvatures seem to have been made. A detailed check on the x coordinates of a network of points would be needed.

Thanks are due to my friends and colleagues of the Optical Instruments Section for their interest in this work, in particular O. N. Stavroudis and Loyd Sutton; the latter did the numerical computations and checked the mathematics.

Washington, June 29, 1954.

Journal of Research of the National Bureau of Standards Vol. 54, No. 5, May 1955 Research Paper 2587

Osculatory Interpolation in the Complex Plane

Herbert E. Salzer[1]

Tables of coefficients to facilitate osculatory n-point interpolation ($n=2(1)7$) in the complex plane are given.

The writer has described in a previous article [1] [2] a new method for osculatory interpolation that can be applied also in the complex plane when one has an analytic function $f(z)$, $z=x+iy$, which is known for arguments z_k at equal intervals along any straight line in the z-plane. However, for the tabular arguments $z_k=x_k+iy_k$ in the form of a Cartesian grid of length h, greater accuracy may be had by basing the Hermite osculatory interpolation formula upon values of $f(z_k)$ and $f'(z_k)$ at points z_k, which are closer together and not necessarily lying upon a straight line (except, of course, in the 2-point case). For a detailed discussion of the Hermite osculatory interpolation formula, the reader is referred to the previous article [1]. This present paper merely aims to supplement that article which was intended primarily for real functions, by giving here the corresponding auxiliary quantities, a_k and b_k, which are suited better for complex interpolation. Whereas the quantities, a_k and b_k, for real interpolation were tabulated up to the 11-point case (21st-degree accuracy), this present tabulation for complex interpolation does not go beyond the 7-point case (13th-degree accuracy), which is more than adequate for most of the practical problems that would arise.

To interpolate for $f(z)$, where $z=z_0+Ph$ and $P\equiv p+iq$ is now complex, we choose the $z_k=z_0+kh$ for k equal to certain small complex integers and such that z_0 will always be the lower left corner point of the configuration of points, z_0 and z_k. Also, in almost every example, $|p|\leq 1$, $|q|\leq 1$, so that the point z is usually not outside the square whose corners are z_0, z_1, z_i, and z_{1+i}. For each of the n-point formulas, $n=2(1)7$, the points z_k are chosen to lie in the following configurations:

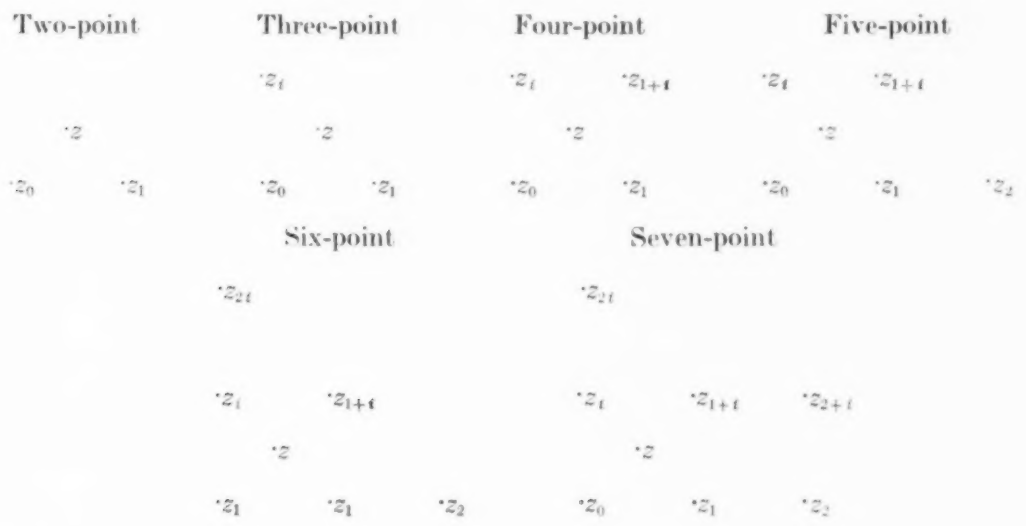

[1] Present address: Diamond Ordnance Fuze Laboratory, Department of Defense.
[2] Figures in brackets indicate the literature references at the end of this paper.

Hermite's n-point osculatory interpolation formula for $f(z)\equiv f$, in terms of $f(z_k)\equiv f_k$ and $'(z_k)\equiv f'_k$, is expressible in the concise form

$$f\sim\sum_k(\alpha_k f_k+h\beta_k f'_k)/\sum_k\alpha_k, \tag{1}$$

where

$$\alpha_k\equiv a_k/(P-k)^2+b_k/(P-k) \tag{2}$$

and

$$\beta_k\equiv a_k/(P-k), \tag{3}$$

the summation being taken for k corresponding to the n-points z_k of the configuration. The dependence of α_k, β_k, a_k, and b_k upon n is understood. The auxiliary quantities, a_k and b_k, are tabulated below for $n=2(1)7$ for each of the above n-point configurations of points z_k. The actual definitions of a_k and b_k are as follows:

$$a_k=C(n)\Big/\left\{\prod_j{}'(k-j)\right\}^2, \tag{4}$$

and

$$b_k=-2C(n)\left\{\frac{d}{dP}\prod_j{}'(P-j)\right\}_{P=k}\Big/\left\{\prod_j{}'(k-j)\right\}^3, \tag{5}$$

where the product is taken for j corresponding to the $n-1$ points $z_j\neq z_k$ of the configuration, and where for each n, $C(n)$ is chosen as the least integer which allows the quantities, a_k and b_k, to appear as complex integers.

Table of a_i and b_i

Two-point

a_0	1	b_0	2
a_1	1	b_1	-2

Three-point

a_0	-2	b_0	$-4+4i$
a_1	i	b_1	$1-3i$
a_2	$-i$	b_2	$3-i$

Four-point

a_0	i	b_0	$3+3i$
a_1	$-i$	b_1	$-3+3i$
a_2	$-i$	b_2	$3-3i$
a_{1+i}	i	b_{1+i}	$-3-3i$

Five-point

a_0	$125i$	b_0	$375+500i$
a_1	$-500i$	b_1	$-1500+500i$
a_2	$-20+15i$	b_2	$117-44i$
a_i	$80-60i$	b_i	$508+44i$
a_{1+i}	-250	b_{1+i}	$500-1000i$

Six-point

a_0	$-500i$	b_0	$-2000-2000i$
a_1	$1280+960i$	b_1	$1856-6208i$
a_2	$-30-40i$	b_2	$83+269i$
a_i	$-1280+960i$	b_i	$-6208+1856i$
a_{1+i}	$-2000i$	b_{1+i}	$6000+6000i$
a_{2i}	$30-40i$	b_{2i}	$269+83i$

Seven-point

a_0	$-80-60i$	b_0	$-648+64i$
a_1	$480-640i$	b_1	$-3264-2048i$
a_2	$30+40i$	b_2	$-3-329i$
a_i	$-320+240i$	b_i	$-1872+704i$
a_{1+i}	$-2000i$	b_{1+i}	$6000+2000i$
a_{2+i}	$80i$	b_{2+i}	$-240-448i$
a_{2i}	10	b_{2i}	$27+57i$

Formulas (1), (2), and (3) for complex osculatory interpolation, which utilize the Cartesian grid, will be especially useful in connection with such tables for complex arguments as (1) logarithm of the gamma function, $\log\Gamma(z)$, together with its derivative the psi function, $\Psi(z)$,

(2) Bessel functions of the first or second kind giving $J_0(z)$ and $J_1(z)=-J_0'(z)$, $Y_0(z)$ and $Y_1(z)=-Y_0'(z)$, or linear combinations of them, (3) probability integral $\int_0^z e^{-u^2}\,du$ with its integrand, (4) miscellaneous tables of integrals of the more elementary functions where the first derivative or the integrand, although not tabulated, is easy to calculate, namely, the function $\int_z^\infty (e^{-u}/u)du$ and (5) tables of solutions of important linear differential equations, together with their first derivatives [2]. In all such tables, and in many others, the user will find these complex osculatory interpolation formulas to be particularly convenient. They are especially suitable in those cases where the grid length h is too large for sufficiently accurate complex interpolation, using either tables of complex interpolation coefficients [3, 4] or formulas corresponding to (1), (2), and (3) above [5], where the tables or formulas involve the use of only the functional values f_i.

Illustration.—To demonstrate the use of these tables in formulas (1) to (3), consider an example from [2], where the modified Hankel functions $h_j(z)\equiv(\frac{2}{3}z^{\frac{1}{2}})^{\frac{1}{3}}H_{\frac{1}{3}}^{(j)}(\frac{2}{3}z^{\frac{1}{2}})$, $j=1, 2$, and their first derivatives are tabulated over a Cartesian grid of length $h=0.1$ in the complex plane. Suppose that it is required to find h_1 (1.24579 316+0.96155 803i), using the four-point osculatory interpolation formula and the tabulated values of h_1, h_1' at $z_0=1.2+0.9i$, $z_1=1.3+0.9i$, $z_i=1.2+1.0i$, $z_{1+i}=1.3+1.0i$ [2, pp. 21, 23]. Employing (2), (3) and a_i, b_i from these tables, since $P=0.45793\ 16+0.61558\ 03i$, one finds that

$$\alpha_0=i/(0.45793\ 16+0.61558\ 03i)^2+(3+3i)/(0.45793\ 16+0.61558\ 03i),$$
$$\alpha_1=-i/(-0.54206\ 84+0.61558\ 03i)^2+(-3+3i)/(-0.54206\ 84+0.61558\ 03i),$$
$$\alpha_i=-i/(0.45793\ 16-0.38441\ 97i)^2+(3-3i)/(0.45793\ 16-0.38441\ 97i),$$
$$\alpha_{1+i}=i/(-0.54206\ 84-0.38441\ 97i)^2+(-3-3i)/(-0.54206\ 84-0.38441\ 97i),$$
$$\beta_0=i/(0.45793\ 16+0.61558\ 03i),\ \beta_1=-i/(-0.54206\ 84+0.61558\ 03i),$$
$$\beta_i=-i/(0.45793\ 16-0.38441\ 97i),\ \beta_{1+i}=i/(-0.54206\ 84-0.38441\ 97i),$$

from which one obtains.

$$\alpha_0=7.09824\ 5538-1.29187\ 9023i,\qquad \beta_0=1.04576\ 6212+0.77794\ 7889i,$$
$$\alpha_1=6.63654\ 0823+0.51581\ 3695i,\qquad \beta_1=-0.91498\ 3814+0.80571\ 7487i,$$
$$\alpha_i=9.82415\ 3465-1.10147\ 8051i,\qquad \beta_i=1.07536\ 0453-1.28099\ 9733i,$$
$$\alpha_{1+i}=8.43081\ 1380+1.81986\ 9385i,\qquad \beta_{1+i}=-0.87048\ 2793-1.22746\ 3667i,$$

Then for (1) we employ the following tabulated values of h_1 and h_1':

$$f_0=0.19018\ 585-0.19313\ 840i,\qquad f_0'=0.14952\ 614+0.33229\ 461i,$$
$$f_1=0.20311\ 754-0.15966\ 418i,\qquad f_1'=0.10901\ 235+0.33659\ 231i,$$
$$f_i=0.15891\ 089-0.17847\ 850i,\qquad f_i'=0.14376\ 041+0.29375\ 232i,$$
$$f_{1+i}=0.17143\ 575-0.14888\ 108i,\qquad f_{1+i}'=0.10669\ 347+0.29764\ 346i,$$

and also

$$\sum_k \alpha_k=31.98975\ 121-0.05767\ 399i,$$

so that we have

$$h_1(1.24579\ 316+0.96155\ 803i)\equiv f\sim[\alpha_0 f_0+\alpha_1 f_1+\alpha_i f_i$$
$$+\alpha_{1+i}f_{1+i}+0.1\{\beta_0 f_0'+\beta_1 f_1'+\beta_i f_i'+\beta_{1+i}f_{1+i}'\}]/\sum_k \alpha_k,$$

whose terms are

$$
\begin{aligned}
&[(7.09824\ 5538-1.29187\ 9023i)(0.19018\ 585-0.19313\ 840i)\\
&\quad+(6.63654\ 0823+0.51581\ 3695i)(0.20311\ 754-0.15966\ 418i)\\
&\quad+(9.82415\ 3465-1.10147\ 8051i)(0.15891\ 089-0.17847\ 850i)\\
&\quad+(8.43081\ 1380+1.81986\ 9385i)(0.17143\ 575-0.14888\ 108i)\\
&\quad+0.1\{(1.04576\ 6212+0.77794\ 7889i)(0.14952\ 614+0.33229\ 461i)\\
&\quad+(-0.91498\ 3814+0.80571\ 7487i)(0.10901\ 235+0.33659\ 231i)\\
&\quad+(1.07536\ 0453-1.28099\ 9733i)(0.14376\ 041+0.29375\ 232i)\\
&\quad+(-0.87048\ 2793-1.22746\ 3667i)(0.10669\ 347+0.29764\ 346i)\}]\\
&\quad\div(31.98975\ 121-0.05767\ 399i),
\end{aligned}
$$

or after multiplying,

$$
\begin{aligned}
&[(1.10047\ 4414-1.61664\ 0896i)+(1.43035\ 4817-0.95484\ 7040i)\\
&\quad+(1.36457\ 4820-1.92843\ 7032i)+(1.71628\ 6592-0.94319\ 7631i)\\
&\quad+0.1\{(-0.10213\ 8505+0.46382\ 6021i)+(-0.37094\ 2846-0.22014\ 3359i)\\
&\quad+(0.53089\ 0903+0.13173\ 2581i)+(0.27247\ 1703-0.39005\ 5868i)\}]\\
&\quad\div(31.98975\ 121-0.05767\ \ 399i)\\
&=(5.64471\ 8767-5.44458\ 6662i)/(31.98975\ 121-0.05767\ \ 399i),
\end{aligned}
$$

or finally,

$$0.17676\ 025-0.16987\ 916i,$$

which is correct to within a unit in the last place, as was seen from the independent calculation of $h_1(1.24579\ 316+0.96155\ 803i)$ from the Taylor series around $z_0=1.2+0.9i$.

---

[1] H. E. Salzer, New formulas for facilitating osculatory interpolation, J. Research NBS **52**, 211 (1954) RP2491.

[2] Harvard Computation Laboratory, Tables of the modified Hankel functions of order one-third and of their derivatives (Harvard University Press, Cambridge, Mass., 1945).

[3] A. N. Lowan and H. E. Salzer, Coefficients for interpolation within a square grid in the complex plane, J. Math. Phys. **23**, 156 (1944).

[4] H. E. Salzer, Coefficients for complex quartic, quintic, and sextic interpolation within a square grid, J. Math. Phys. **27**, 136 (1948).

[5] H. E. Salzer, Formulas for complex Cartesian interpolation of higher degree, J. Math. Phys. **28**, 200 (1949).

Washington, August 6, 1954.

Journal of Research of the National Bureau of Standards Vol. 54, No. 5, May 1955 Research Paper 2588

Macromethods For Reducing Aldonic Lactones To Sugars: The Preparation of L-Glucose[1]

Harriet L. Frush and Horace S. Isbell

Two macroprocedures are described for the efficient reduction of lactones of aldonic acids by sodium amalgam in the presence of an oxalate buffer. One employs a stainless-steel flask equipped with a stirrer that sweeps the bottom of the flask; the other, a high-speed "blender." Either method is suitable for the preparation of rare sugars in relatively large quantities. By the procedures described, L-glucose has been prepared from L-glucono-δ-lactone in 88-percent yield, for use as carrier in the preparation of L-glucose-1-C^{14}.

1. Discussion

Synthesis of sugars by the cyanohydrin method of Kiliani and Fischer has been, and still remains, of great importance to carbohydrate chemistry. Originally, the process was tedious and the yields were low. Thus, in the classical synthesis of L-glucose from L-arabinose the over-all yield was only 3 percent [1].[2] Although the technique of reduction by sodium amalgam has since been improved [2, 3, 4], the procedure has nevertheless been laborious and somewhat variable as to results. For use in the synthesis of C^{14}-labeled sugars on a semimicroscale, a convenient procedure was recently developed for the sodium-amalgam reduction of millimole quantities of aldonic lactones in yields as high as 85 to 90 percent [5, 6]. The reduction is carried out in a closed system. Accurate *p*H control is obtained by using an excess of a slightly soluble acid salt (sodium acid oxalate) as a buffering agent. This avoids the necessity for continual adjustment of *p*H by titration of the alkali formed in the reaction. The method has now been adapted to macropreparations with equally successful results. Two procedures were found to be convenient for the reduction of a 5- or 10-g quantity of lactone. The simpler and more rapid procedure involves treatment of the lactone with sodium amalgam and excess sodium acid oxalate in a high-speed "blender" partially filled with ice. The maximum yield of sugar from the lactone compares favorably with that obtained in the semimicro apparatus [7], and requires approximately the same proportion of amalgam; the reaction is complete in 15 min. For the preparation of C^{14}-labeled sugars, however, the procedure is complicated by the formation of mist, or spray, that is difficult to confine to the apparatus. The second procedure for reduction makes use of a stainless-steel flask equipped with a stirrer that sweeps the bottom of the flask. The amount of sodium amalgam necessary for maximum yield of the sugar was found to depend somewhat on the efficiency of stirring, and, in the apparatus employed, was 2 or 3 times as large per mole of lactone as that required in the blender. However, the two procedures give comparable results, and both are suitable for the macroreduction of any aldonic lactone.[3]

2. Experimental Procedures

2.1. Reduction of L-Glucono-δ-Lactone to L-Glucose in a High-Speed Blender

Approximately 500 ml of ice slush was agitated with 55 g of sodium acid oxalate and 10 g of L-glucono-δ-lactone in a high-speed blender having stainless-steel blades. After a few seconds, 130 g of 5-percent sodium amalgam pellets [8] was added quickly; agitation was continued for 15 min, during which time the temperature rose to 33° C. The mercury was then separated, and the solution was neutralized with dilute sodium hydroxide solution until a faint but permanent pink color was obtained in the presence of phenolphthalein indicator. The solution was evaporated under reduced pressure to a volume of about 100 ml and treated with 5 volumes of methanol. The precipitated salts were separated, washed with a little methanol, and discarded. The filtrate was concentrated under reduced pressure to about 50 ml, and again treated with 5 volumes of methanol. Precipitated salts were removed by filtration, and the solution, after concentration under reduced pressure to about 50 ml, was deionized by passage through 60 ml of mixed cation and anion exchange resins in a column having a layer of cation exchange resin at the bottom.[4] The neutral solution and washings from the column were evaporated under reduced pressure to a thin sirup (about 10 ml), which was diluted with an equal amount of methanol, and then with 2-propanol almost to the point of turbidity. The solution gave 8.92 g of crystalline L-glucose in three crops, corresponding to 88.3 percent of the theoretical yield.

[1] Part of a project on the development of methods for the synthesis of radioactive carbohydrates sponsored by the Atomic Energy Commission.

[2] Figures in brackets indicate the literature references at the end of this paper.

[3] The aldonic lactones vary considerably in ease of reduction and in the tendency of the sugar to be reduced further to the corresponding sugar alcohol. Consequently, the optimum amount of amalgam to be used must be determined for each lactone reduced.

[4] Equivalent quantities of Amberlite 1R-120-H, analytical grade, Rohm & Haas Co., Philadelphia, Pa., and Duolite A-4, Chemical Process Co., Redwood City, Calif. The layer of cation exchange resin at the bottom of the column gives rise to an acid reaction in the effluent when insufficient mixed resin is used.

2.2. Reduction of D-Glucono-δ-Lactone-1-C^{14} on a Relatively Large Scale in a Stainless-Steel Flask

Eighty grams of sodium acid oxalate, 7 g of crude D-glucono-δ-lactone-1-C^{14} having an activity of 5,330 μc, and 500 ml of ice water were placed in a two-necked, 1-liter, stainless-steel flask equipped with an efficient stirrer.[5] The solution was stirred vigorously and 180 g of 5-percent sodium amalgam pellets was added at one time. After 2 hr of stirring at ice-bath temperature, the mercury was separated; the reaction mixture was made alkaline to phenolphthalein and then carefully neutralized with oxalic acid.[6] The crystalline sodium salts were separated and washed with methanol. The combined aqueous solution and methanol wash liquor were concentrated under reduced pressure to about 250 ml, after which a crop of crystalline sodium oxalate was separated by filtration, washed with methanol, and discarded. The filtrate was concentrated to about 20 ml at a temperature less than 40° C, and another crop of salts was separated. The resulting solution was concentrated under reduced pressure at 30° C to a sirup that was then diluted with 5 volumes of methanol. The mixture was filtered, and the residue was washed with 30 ml of methanol in 3 portions. Finally, the methanol solution was diluted with an equal volume of ethanol, and the salts that precipitated were separated by filtration and washed with methanol. The filtrate was concentrated to remove most of the alcohol; the resulting solution was diluted with 50 ml of water and was passed over a column containing 100 ml of mixed cation and anion exchange resins. The column was washed with water, the combined solution [7] and washings were evaporated to 50 ml under reduced pressure at a temperature less than 40° C, and the solution was then freeze-dried. The residue was taken up at once in 15 ml of methanol and brought to crystallization by the addition of 2-propanol to the point of incipient turbidity. The crystalline D-glucose-1-C^{14} that formed, after separation and recrystallization, weighed 5.47 g and contained 3,954 μc of carbon-14. By use of nonradioactive carrier, an additional 658 μc of crystalline α-D-glucose-1-C^{14} was obtained. Thus the radiochemical yield was 4,612 μc, or 84.3 percent of the theoretical.[8] By elution with 10-percent aqueous acetic acid of the mixed resin used for the purification of the sugar, crude D-gluconic acid-1-C^{14} with an activity of 645 μc was recovered.

[5] The stirrer consisted of a stainless-steel rod fitted with a curved vane, 7 cm long, that conformed in shape to the flask and swept the bottom.

[6] The solution must be kept neutral during the steps that follow to avoid undesirable reactions.

[7] The *p*H of the solution at this point must be close to 7; otherwise, additional resin must be used.

[8] In reductions of pure nonradioactive D-glucono-δ-lactone, yields of approximately 90 percent were obtained.

3. References

[1] E. Fischer, Ber. deut. chem. Ges. **23,** 2618 (1890).
[2] M. Steiger, Helv. Chim. Acta **19,** 180 (1936).
[3] F. J. Bates and associates, Polarimetry, saccharimetry and the sugars, NBS Circular 440, p. 465 (1942).
[4] N. Sperber, H. E. Zaugg, and W. M. Sandstrom, J. Am. Chem. Soc. **69,** 915 (1947).
[5] H. S. Isbell, U. S. Patent 2,632,005 (1953).
[6] H. S. Isbell, J. V. Karabinos, H. L. Frush, N. B. Holt, A. Schwebel, and T. T. Galkowski, J. Research NBS **48,** 163 (1952) RP2301.
[7] H. L. Frush and H. S. Isbell, J. Research NBS **50,** 133 (1953) RP2400.
[8] H. L. Frush and H. S. Isbell, J. Research NBS **51,** 307 (1953) RP2458.

WASHINGTON, January 21, 1955.

Journal of Research of the National Bureau of Standards Vol. 54, No. 5, May 1955 Research Paper 2589

Stress-Strain Relationships in Yarns Subjected to Rapid Impact Loading: 1. Equipment, Testing Procedure, and Typical Results [1]

Walter K. Stone, Herbert F. Schiefer, and George Fox [2]

Equipment is described for elongating yarns by longitudinal impact at velocities ranging from 10 to 100 meters per second. The rate of straining at impact varies from about 100,000 to 500,000 precent per minute.

A procedure is discussed for obtaining load-elongation curves for loading and for unloading of the specimen and for loading to rupture in a time interval of only a few milliseconds. The results of a typical loading and unloading test are presented.

1. Introduction

Textile materials in processing and use are subjected ever more frequently to higher rates of straining. For example, in high-speed industrial sewing the thread is subjected to impact velocities ranging from 1 to 10 m/sec as often as 5,000 times per minute. This results in high-frequency cyclic accelerations of the thread, which may equal several million centimeters per second per second. These high accelerations of the thread produce forces that approach, and may even exceed, the breaking strength of the thread. Similar conditions may be attained in high-speed processing of fibers, such as carding and combing or the weaving and knitting of yarns into fabrics; in the cord of an airplane tire during landing; in the safety line when a structural worker attached to it falls; and in the fabric, shroud lines, and webbing during the opening of a parachute.

The present work was undertaken to provide basic information on the behavior of textile materials when strained at very high rates; to relate the results to the molecular structure of the fibers and to the geometry of the yarns and fabrics; and finally, to indicate the applications of this information to safety engineering, to industrial processing of textiles, to the development of fibers of improved impact properties, and to industrial and military end uses of textile structures for specific performance requirements.

This is the first of a series of papers on rapid impact testing. In this paper equipment and procedures for this purpose are described and typical results are presented.

The stress-strain behavior of textile and other materials has been thoroughly investigated at rates of straining ordinarily referred to as "static" tensile testing. The velocity of the moving head of the testing machine in static testing is usually between about 0.1 and 10 inches per minute (4×10^{-5} and 4×10^{-3} m/sec). The corresponding rates of straining range from about 1 to 100 percent per minute for textile materials. In impact testing, usually made by dropping a mass a known height or by allowing a pendulum to swing freely through 90 to 180 degrees to rupture the specimen, the velocity at impact is usually limited by room dimensions to values between 1,000 and 20,000 in./min. (0.4 and 8 m/sec). The corresponding rates of straining range from about 10,000 to 200,000 percent per minute. Although excellent work has been reported in this velocity range [1 to 10],[3] the information concerning the stress-strain behavior of textile and other materials is not as complete as for static testing. The information at higher impact velocities, 20,000 to 10,000,000 in./min (8 to 4,000 m/sec) or rates of straining ranging from about 200,000 to 100,000,000 percent per minute, is incomplete. Much of the published work in this velocity range is theoretical or has been confined to very small strains [11 to 35]. Meredith [7] has recently published excellent stress-strain relationships for viscose rayon, acetate, silk, and nylon yarns for rates of straining between 0.05 and 70,000 percent per minute. The rates of straining obtainable with the equipment described in this paper are between about 100,000 and 1,000,000 percent per minute for textile materials. Even this maximum rate of straining is considerably below the rates of straining that prevail when textile materials are tested at their critical velocities.[4] These rates of straining are estimated to range from about 10,000,000 to 100,000,000 percent per minute.

2. Equipment and Testing Procedure

Equipment has been constructed at the National Bureau of Standards for applying longitudinal impacts, at velocities up to 100 m/sec, to one end of a specimen of textile fiber, yarn, cord, or other materials having similar dimensions. The rates of straining range from 100,000 to 500,000 percent per minute. A high-speed motion-picture camera and mirrors are used to photograph simultaneously the

[1] This work was sponsored by the Office of the Quartermaster General, Department of the Army, and was presented in part at the September 1953 and 1954 meetings of The Fiber Society, and also at the November 1954 meeting of the Society of Rheology.

[2] Present address, Lehigh University, Bethlehem, Pa.

[3] Figures in brackets indicate the literature references at the end of this paper.

[4] The concept of critical velocity was suggested by von Kármán [32, 33] and has been discussed by Hoppmann [27] and by Andersson and Steenberg [11].

positions of the head and tail ends of the specimen during the first few milliseconds from the time of impact. The stress-strain behavior of the specimen is then derived from the photographic record.

The specimen to be tested is usually ⅔ m long, but can be varied in length. One end is fastened to a head mass, hereafter termed "head," which is impacted. The other end is fastened to a tail mass, hereafter termed "tail." The head and tail, with a specimen of yarn attached to them, are shown in figure 1.

The manner of attaching the specimen is important. The specimen must not be damaged, high stress concentration must be avoided, and slippage must be minimized. An effective way of attaching a specimen is shown in figure 1. A small hole is drilled in the end of the head and the tail in such a way that it terminates in a helical groove on the surface. The bottom of the groove is coated with a rubber-like high-friction compound. The end of a specimen is threaded through the hole, wound in the groove, and snubbed under the shoulder of a recessed screw. It is apparent that as the longitudinal tension in the specimen is increased during an impact test the radial pressure of the specimen against the groove is also increased. The longitudinal stress is thus effectively transferred between the specimen and the head or tail through the increased contact friction. The effective length of the specimen is equal to the distance between the inner ends of the head and tail plus 1 cm at each end for the helical groove.

The tail and attached specimen are inserted in a tube, as shown in figure 2. The right portion of this tube is made of transparent plastic, so that the tail and a portion of the specimen are visible. The head is fitted into the left end of the tube. Two disks are attached to the middle portion of the tube to serve as the bearing shaft when the tube is inserted in the impact equipment for a test.

A portion of the impact equipment is shown in figure 3. The upper view shows the tube, with the head in a vertical position. Directly below the head and tube a portion of a heavy disk is visible. The disk can be rotated counterclockwise. Two lugs, called hammers, are attached to the disk. They are visible to the left of the head in the upper view of figure 3. In a test the speed of the disk may be adjusted to values between 5 and 50 rps. The peripheral speed of the hammers ranges from about 10 to 100 m/sec. A stroboscope is used to measure the speed of the disk.

The upper view of figure 3 shows the hammers in a position where a sector (not shown) attached to the disk closes an electric contact in a triggering circuit. When this circuit is closed a solenoid releases a spring-loaded cam. This cam rotates the tube containing the tail, specimen, and head through 90 degrees in less time than is required for one rotation of the hammers, even when the disk rotates at a speed as high as 50 rps. With the head in a horizontal position, lower view of figure 3, the head will be struck by the hammers of the disk for the impact test of the specimen attached to the head.

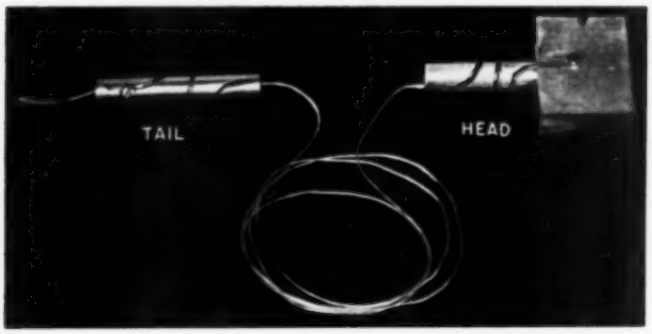

FIGURE 1. *Yarn specimen fastened to head and tail for an impact test.*

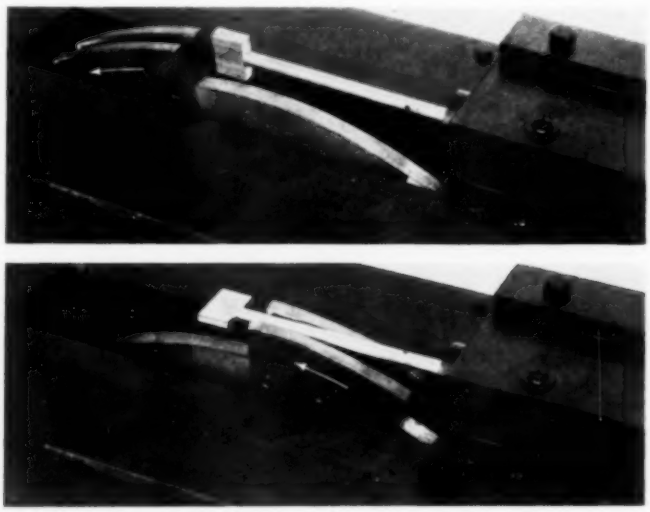

FIGURE 3. *A portion of the impact equipment.*

Upper view shows the head in a vertical position and hammers at the instant when a contact in the triggering circuit is closed by the disk. Lower view shows the head in a horizontal position and the hammers at the instant prior to impact of the head.

FIGURE 2. *Tube containing yarn specimen and attached tail, with the head attached to left end of tube.*

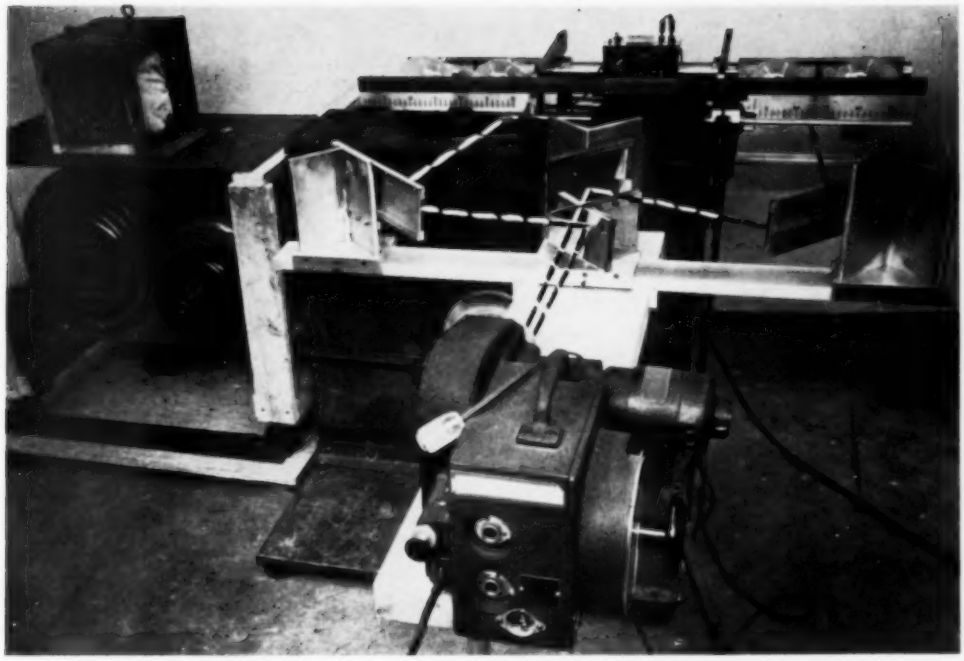

FIGURE 4. *Assembly of impact-testing equipment.*

Variable-speed motor at the left, with catch box above it; high-speed camera in the foreground; photoflood bulbs, scales, tube containing head, specimen, and tail in the background; mirror system in the center; broken lines to indicate paths of light beams from the head and tail.

The assembly of the impact-testing equipment is shown in figure 4. A 5-hp variable-speed motor, used for rotating the disk at high speed, is shown at the left. Directly above it is a box in which the head is caught after impact. The tube containing the head, specimen, and tail is shown to the right of the box. Two scales, ruled in centimeters on transparent plastic, are shown directly above the tube. Photoflood bulbs are mounted directly in back of the tube. A high-speed motion-picture camera is shown in the foreground. A system of mirrors is mounted between the tube and camera. The paths of representative light beams from the head and tail are indicated by the broken lines. The mirrors are mounted on a metal base and can be readily adjusted to different horizontal positions. The mirrors can also be adjusted in their inclination so that the image of the tail and its scale appear above the image of the head and its scale in the field of view of the camera. The head and tail are photographed in silhouette, as shown in figure 5.

After adjusting the speed of the disk to the desired value for a test, and with the head, specimen, and tail in position, the motor of the camera and the photoflood bulbs are turned on. When the film has attained the desired speed, the camera closes an electric contact in the triggering circuit of the solenoid. This contact is in series with the solenoid, a series of batteries (alternating current of 60 cycles is not reliable for this purpose), and the contact on the disk referred to previously. The contact on the disk is closed the next time the hammers reach

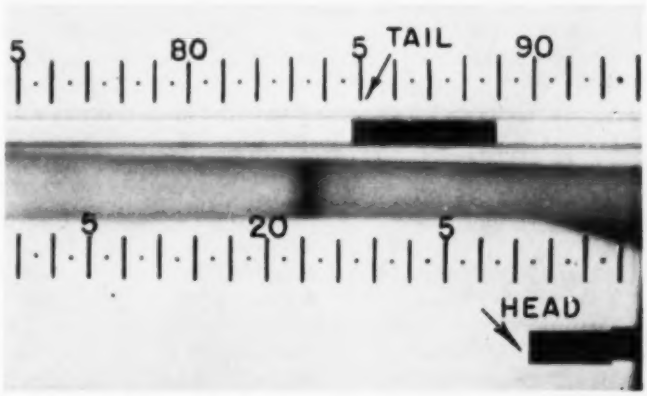

FIGURE 5. *Camera field view of specimen ends before impact.*

the position shown in the upper view of figure 3. At this time the solenoid is energized and actuates a trigger to release the spring-loaded cam. The cam rotates the tube and head into a horizontal position (bottom view of fig. 3). The head will be struck by the hammers on the next rotation of the disk for the impact test. The motions of the head and tail after impact are recorded by the high-speed camera.

After impact, the head is thrown to the left (fig. 4) and is caught in the box above the variable-speed motor. The tail is usually caught in the box. In some tests it remains in the tube or is thrown out of the rear of the plastic tube by the reaction from the specimen after rupture has occurred.

3. Behavior of Specimen After Impact

A few microseconds after impact, the head will attain a velocity exceeding that of the manner, and therefore will move in free flight ahead of the hammer. The sudden impact of the head produces a strain in the specimen where it is attached to the head. This strain depends on the impact velocity and on the material being tested. This strain and a tension approximately proportional to it will be propagated along the specimen toward the tail. When the strain reaches the tail it will be reflected and the reflected strain propagated toward the head. The strain and tension at the tail are approximately doubled upon reflection.

The propagation of the strain along the specimen and the successive reflections at the head and the tail will continue. At each reflection the strain and the tension are increased. The increased tension will cause a deceleration of the head and an acceleration of the tail. This process will continue until the rupture strain is reached and the specimen breaks, or until the velocity of the tail equals that of the head, at which time the specimen will be at maximum average strain and under maximum average tension, but both are below the rupture values. After this time the tension in the specimen will continue to decelerate the head and to accelerate the tail, so that the velocity of the tail will exceed that of the head. As soon as the velocity of the tail exceeds that of the head the strain will be relieved and the tension in the specimen will be decreased. This process of strain release and propagation is probably similar to that occurring during the increase of the strain, and will continue until all of the recoverable strain is relieved, at which time the tension will have been reduced to zero and the specimen will become slack. The specimen is thus loaded to a maximum tension and extension and then unloaded to zero tension and a set or extension in a total time of several milliseconds. Part of the set may be reduced by delayed recovery.

The propagation of the strain pulse after impact and subsequent reflections at the tail and head are indicated schematically in figure 6, A to H. Before impact, the specimen is represented in A by a series of adjoining circular springs. After impact, in B, the circular spring next to the head is deformed into an ellipse, and the strain pulse is indicated by the adjacent cross-hatched circle and ellipse. The arrow indicates the direction of strain propagation. C and D show the arrival and reflection of the strain pulse at the tail. At this moment the tail is set in motion, and the ellipse before reflection is deformed to one of greater eccentricity after reflection. E indicates the arrival of the reflected strain pulse at the head. After reflection at the head, the strain pulse is shown in F as traveling toward the tail about midway between the head and tail. In G the strain pulse is shown as traveling toward the head after reflection at the tail and the high strain is indicated by the highly eccentric ellipses. After the next reflection at the head it is assumed that the rupture

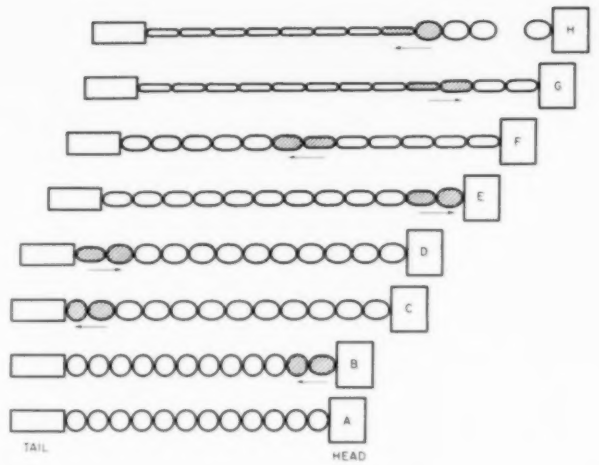

FIGURE 6. *Schematic representation of strain propagation in specimen, indicated by adjoining circular springs, after impact of the head at an instant between A and B.*

Cross-hatched circle and ellipse represent the strain pulse.

strain is attained, and the ruptured specimen is shown in H. After rupture, the strain is released. This condition is represented in H by the reconversion (recovery) of the ellipses of high eccentricity to ellipses of low eccentricity or to circles for complete recovery. The propagation of the strain-release pulse is indicated by the arrow. The ruptured end will snap toward the tail with a very high velocity, and the momentum acquired by the specimen, when the strain-release pulse reaches the tail, may be sufficient to stop the tail or to reverse its motion.

4. Tests on a Nylon Yarn

A specimen of nylon yarn was fastened at one end to a head weighing 19.82 g and at the other end to a tail of 4.85 g, the length between fastenings being 65 cm. The head was impacted at a velocity of 30 m/sec.

The motions of the head and tail were recorded photographically by means of high-speed motion pictures taken at a rate of 2,630 frames per second. The sequence of pictures is shown in figure 7, beginning with two frames before impact, upper left-hand corner, and ending after release of the strain, lower right-hand corner. It can be seen that before impact in frames 1 and 2 the positions of the head and tail remain stationary relative to the fixed centimeter scale, which is photographed on each frame. After impact, which occurred between frames 2 and 3, the head moves relative to the fixed scale until it finally disappears from the field of view of the camera. The tail, on the other hand, moves very little for several frames after impact. It then speeds up until in frame 10 it moves the same amount as the head. Thereafter it moves further per frame than the head; after frame 16 the distance moved per frame is maximum and essentially constant.

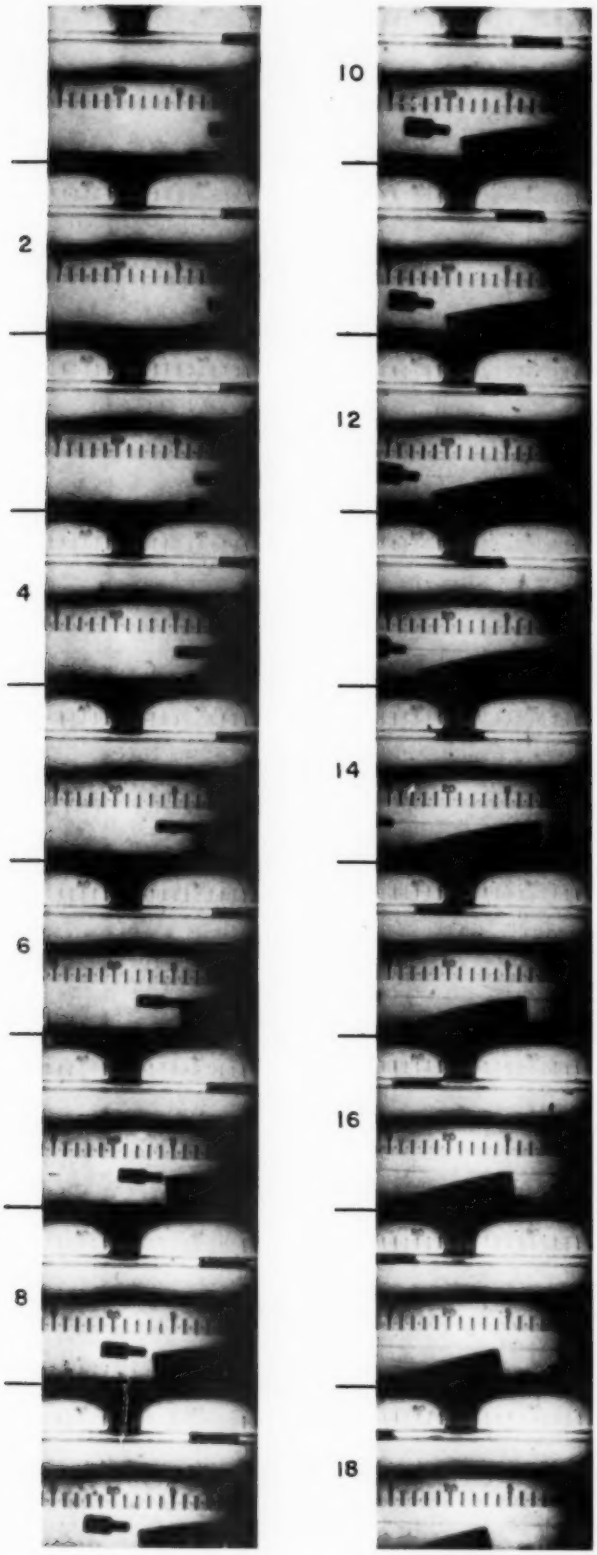

FIGURE 7. *Film strips showing motion of head and tail.*

Impact occurs between frames 2 and 3, maximum tension between frames 10 and 11.

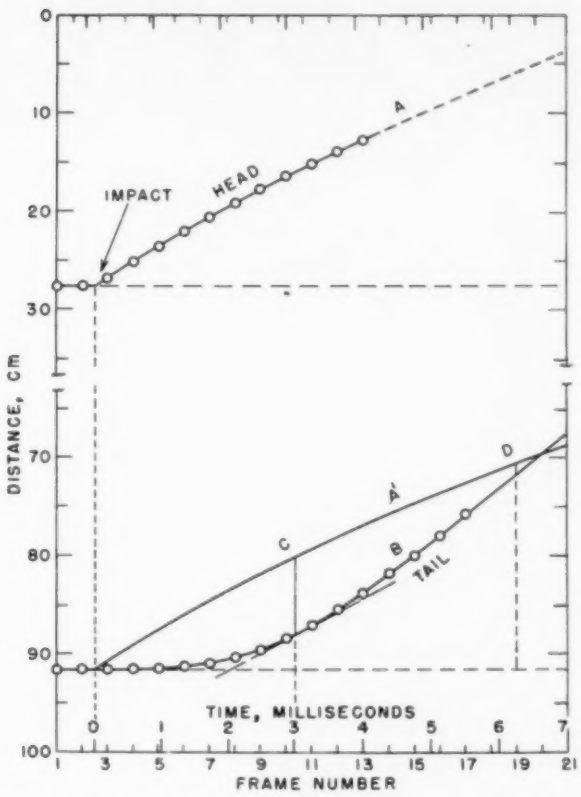

FIGURE 8. *Position of head and of tail on successive frames in an impact test of a nylon yarn.*

The positions of the head and of the tail on each frame were carefully measured, relative to the fixed scale, with a precision micrometer. These positions are plotted in figure 8 against frame number and also against time in milliseconds. The resulting curves will hereafter be referred to as distance-frame or distance-time curves. Zero time refers to the instant of impact and is obtained by extrapolating the distance-frame curve, A, of the head after impact back to the distance-frame curve of the head before impact. The point of intersection of these two curves is taken as the instant of impact.

The distance-time curve of the head is slightly concave downward, indicating that the head is slowing down. The slope of this curve at any point (time) is equal to the velocity of the head at that time. The velocity-time curve of the head is plotted in figure 9. Immediately after impact the velocity of the head is about 45 m/sec. At 4 msec after impact it is reduced to 30 m/sec.

The distance-time curve of the tail, B of figure 8, is concave upward, indicating that its velocity increases with time. At 3 msec the slope of the distance-time curve for the tail is equal to that for the head, indicating that the velocities of the head and the tail are equal. The velocity-time curve of the tail is also plotted in figure 9. The velocity of the tail is zero before impact, then increases slowly immediately after impact. It increases most rapidly at 3

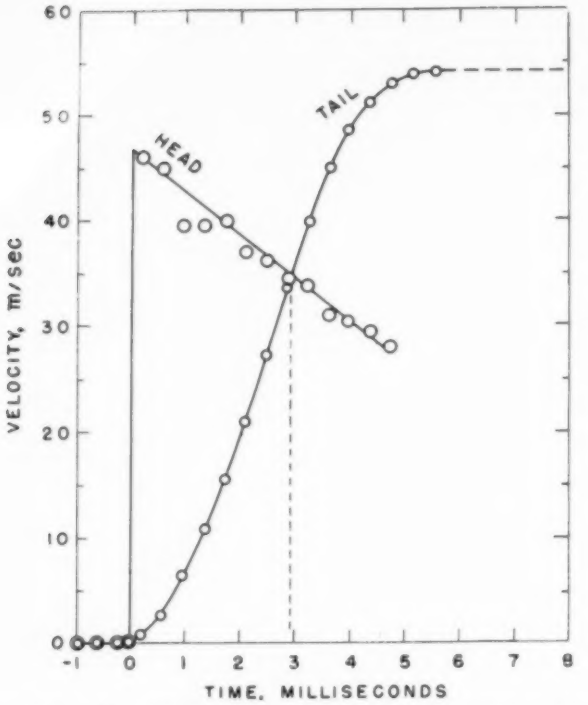

FIGURE 9. *Velocity of head and of tail after impact in a test of a nylon yarn.*

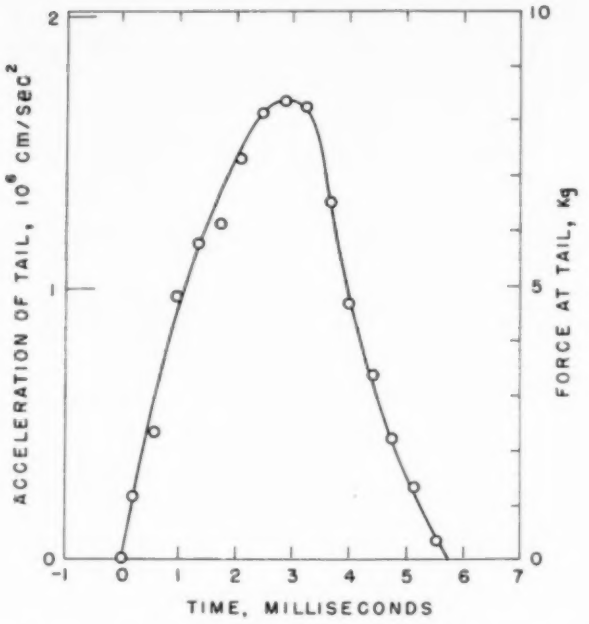

FIGURE 10. *Acceleration of tail and force at tail after impact in a test on nylon yarn.*

msec after impact when it attains the head velocity of 35 m/sec. It then increases less rapidly becoming essentially a constant, 54 m/sec, at 5 msec.

The slope of the velocity-time curve for the tail-figure 9, at any point (time) is equal to the accelera, tion of the tail. This acceleration is plotted against time in figure 10. The maximum value is more than a million centimeters per second per second. Because the force on the tail (and thus on the specimen at the tail) at any time is equal to the mass times its acceleration, the curve in figure 10 is also a force-time curve of the specimen at the tail. The ordinate scale given at the right side of figure 10 is in force units (kilograms). The curve in figure 10 thus indicates the force that the tail exerts on the specimen during loading and unloading. The total time for loading and unloading is only 6 msec in this test.

From figure 9 it is seen that the deceleration of the head at 3 msec after impact is approximately equal to one-fourth of the acceleration of the tail. As the mass of the head is about four times that of the tail it is evident that the force at the head is essentially equal to that at the tail.

In figure 8 the vertical distance between the distance-frame curve for the head, A, and the distance-frame curve for the tail, B, at any frame (time) is equal to the length of the specimen at that time. The extension of the specimen at any time is given by the distance between the two curves at this time minus the distance between the two curves before impact. This extension is indicated graphically by the distance between curves A′ and B, where A′ is the distance-frame curve for the head, A, after it was shifted down to A′ so that the portion before impact coincided with the similar portion of the curve B before impact. It can be seen that the extension (distance between curves A′ and B) increases for times up to 3 msec, and then decreases. It is zero again at 6.7 msec (frame 20). At this time, after impact, the head and the tail have moved the same total distance; that is, the length of the specimen (distance between head and tail) is again the same as before impact. If the specimen had recovered completely from its extension, it would have been under zero strain and zero tension at this instant. It was observed, however, that the specimen was already slack in frame 19 (6.3 msec after impact). The distance between the two curves at frame 19; namely, at D, figure 8, therefore represents the extension that remained after the specimen was completely unloaded. Part of this extension may have been recovered subsequently by delayed recovery. The extension during loading and unloading, expressed as a percentage of the specimen length before impact, and termed "elongation," is plotted against time in figure 11. This elongation at any given time is the average elongation of the specimen. Actually, the elongation is not constant along the specimen, but shows a sharp increment at the strain-wave front.

From the force-time curve in figure 10 and the elongation-time curve in figure 11 it is possible to plot simultaneous values of force and elongation. The result is a load-elongation curve for loading and also for unloading, as shown in figure 12. The energy to maximum load is then readily obtained, as well as the energy recovered during unloading. The difference between these values, if converted into heat and assumed to be uniformly distributed throughout the specimen, would be sufficient to raise the tempera-

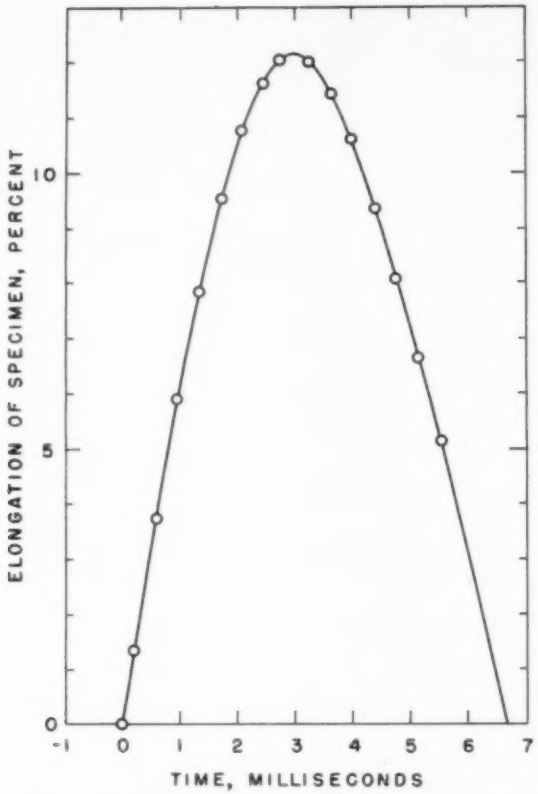

FIGURE 11. *Average elongation of specimen after impact in a test on nylon yarn.*

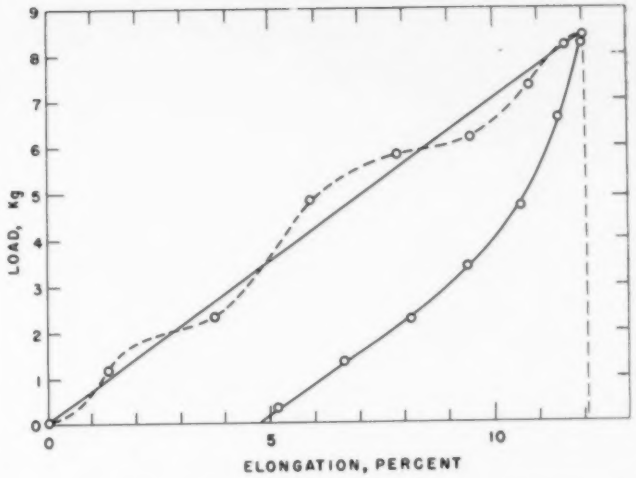

FIGURE 12. *Load at tail plotted against average elongation for loading and unloading of a nylon yarn in an impact test.*

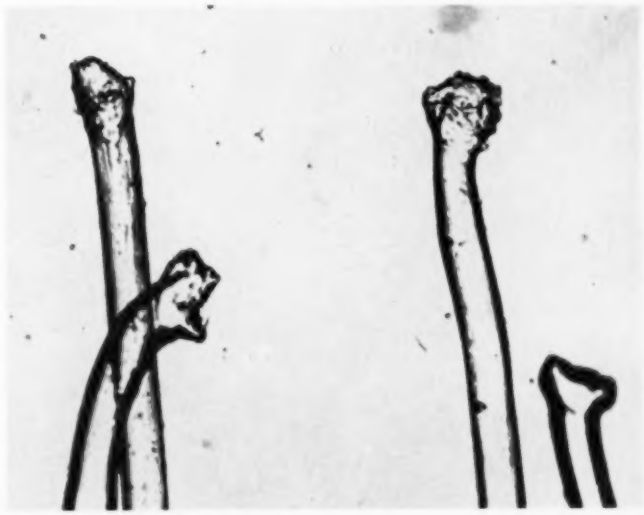

FIGURE 13. *Magnified view of ruptured filaments of nylon showing fused ends.*

ture of the specimen about 10° C. Actually, this hysteresis energy is not converted uniformly into heat throughout the specimen. For example, in another test in which the maximum strain was sufficient to rupture the specimen the fiber tips were fused, as shown in figure 13, which is evidence of high heat concentration at the point of rupture. This fused condition possibly results from the relatively low heat dissipation in nylon and the high localized energy released by bond rupture.

The points for the loading curve, broken line in figure 12, appear to lie systematically above and below the solid straight line that is drawn through them. The straight line indicates that at this high impact velocity the nylon specimen essentially obeyed Hooke's law during loading. However, the scatter of the points about the straight line is too consistent to be ascribed to experimental errors. It appears that this scattering of the points about the straight line is experimental evidence that the force at the tail varies in a stepwise manner. Each step in load indicates the arrival and reflection of a strain wave at the tail. It is significant to note that the individual points of the velocity-time curve for the head, figure 9, show evidence that the deceleration of the head, and thus the force at the head, also varies in a stepwise manner. An analysis of these variations indicates that the time for the strain pulse to travel from the head to the tail, or 0.65 m, is about 3×10^{-4} sec. The velocity of strain propagation is therefore about 2,200 m/sec. The strain at impact, given by the ratio of the velocity of the head at impact to the velocity of strain propagation, is thus about 2 percent. More detailed strain analyses for impact loading are given in subsequent papers [36, 37].

5. References

[1] J. B. Dickson, Functional properties in textile design, J. Textile Inst. **44**, P514 (1953).
[2] J. B. Dickson and L. A. Davieau, Impact tester for textiles, ASTM Bull. 198, 85 (1954).
[3] G. Glaser, Zur dynamischen Festigkeit von Bergseilen, Melliand Textilber. **24**, 337, 377 (1943).
[4] E. R. Kaswell, Low temperature properties of textile materials, Am. Dyestuff Reptr. **38**, P127 (1949).
[5] H. Leaderman, Impact testing of textiles, Textile Research J. **13**, 21 (1943).
[6] W. J. Lyons and I. B. Prettyman, Use of the ballistic pendulum for impact testing of tirecord, Textile Research J. **23**, 917 (1953).

[7] R. Meredith, The effect of rate of extension on the tensile behavior of viscose and acetate rayons, silk, and nylon, J. Textile Inst. **45**, T30 (1953).
[8] S. B. Newman and Helen G. Wheeler, Impact strength of nylon and sisal ropes, J. Research NBS **35**, 41 (1945) RP1679.
[9] H. F. Schiefer, W. D. Appel, J. F. Krasny, and G. G. Richey, Impact properties of yarns made from different fibers, Textile Research J. **23**, 489 (1953).
[10] A. H. Stang, M. Greenspan, and S. B. Newman, Dynamic tensile tests of parachute webbing, J. Research NBS **36**, 411 (1946) RP1710.
[11] O. Andersson and B. Steenberg, Paper under impact conditions, Svensk Papperstidn. **53**, 1 (1950).
[12] O. Andersson, An impulse method for measuring the impact strength of paper, Svensk Papperstidn. **56**, 403 (1953).
[13] O. Andersson, A note on the application of mechanical models to studies of tensile properties of paper, Svensk Papperstidn. **56**, 587 (1953).
[14] O. Andersson and L. Sjöberg, Tensile studies of paper at different rates of elongation, Svensk Papperstidn. **56**, 615 (1953).
[15] J. W. Ballou and S. Silverman, Determination of Young's modulus of elasticity for fibers and films by sound velocity measurements, Textile Research J. **14**, 282 (1944).
[16] W. R. Campbell, Determination of dynamic stress-strain curves from strain waves in long bars, Proc. Soc. Exptl. Stress Anal. **10**, 113 (1952).
[17] W. R. Campbell, Dynamic stress-strain curves for mild steel using the tangent modulus procedure, J. Wash. Acad. Sci. **43**, 102 (1953).
[18] J. D. Campbell, An investigation of the plastic behavior of metal rods subjected to longitudinal impact, J. Mech. and Phys. of Solids **1**, 113 (1953).
[19] D. S. Clark and D. S. Wood, The time delay for the initiation of plastic deformation at rapidly applied constant stress, Proc. ASTM **49**, 717 (1949).
[20] J. D. Cole, C. B. Dougherty, and J. H. Huth, Constant strain waves in strings, J. Appl. Mechanics **20**, 519 (1953).
[21] J. W. Craggs, Wave motion in plastic-elastic strings, J. Mech. and Phys. of Solids **2**, 286 (1954).
[22] H. DeVries, On the elastic and optical properties of cellulose fibers (Drukkerij Fa Schotanus & Jens, Utrecht, Holland, 1953).
[23] B. A. Dunnell and J. H. Dillon, The measurement of dynamic modulus and energy losses in single textile filaments subjected to forced longitudinal vibrations, Textile Research J. **21**, 393 (1951).
[24] W. George, The measurement and physical interpretation of the mechanical strength of filaments, Textile Research J. **21**, 847 (1951).
[25] R. D. Glauz and E. H. Lee, Transient wave analysis in a linear time-dependent material, J. Appl. Phys. **25**, 947 (1954).
[26] W. Hamburger, The application of sonic techniques to the investigation of the effect of visco-elastic behavior upon stress-strain relationships in certain high polymers, Textile Research J. **18**, 705 (1948).
[27] W. H. Hoppmann, The velocity aspect of tension-impact testing, Proc. ASTM **47**, 533 (1947).
[28] H. Kolksy, An investigation of the mechanical properties of materials at very high rates of loading, Proc. Phys. Soc. [B] **62**, 676 (1949).
[29] E. H. Lee and I. Kanter, Wave propagation in finite rods of visco-elastic material, J. Appl. Phys. **24**, 1115 (1953).
[30] R. Sips, Propagation phenomena in elastic-vicose media, J. Polymer Sci. **6**, 285 (1951).
[31] B. Steenberg, Behavior of paper under stress and strain, Pulp & Paper Mag. Can. **50**, 207 (1949).
[32] T. von Kármán, On the propagation of plastic deformation in solids, OSRD Repo). No. 360, PB20276 (1942 rt
[33] T. von Kármán, The propagation of plastic deformation in solids, J. Appl. Phys. **21**, 987 (1950).
[34] W. J. Lyons, Some theoretical considerations of dynamic property data on textile specimens, J. Appl. Phys. **21**, 520 (1950).
[35] D. S. Villars, Ultra speed tensile of rubber and synthetic elastomers, J. Appl. Phys. **21**, 565 (1950).
[36] Frank L. McCrackin, Herbert F. Schiefer, Jack C. Smith, and Walter K. Stone, Stress-strain relationships in yarns subjected to rapid impact loading: 2. Breaking velocities, strain energies, and theory neglecting wave propagation, J. Research NBS **54**, 277 (1955) RP2590.
[37] Jack C. Smith, Frank L. McCrackin, and Herbert F. Schiefer, Stress-strain relationships in yarns subjected to rapid impact loading: 3. Effect of wave propagation, J. Research NBS **55** (in press).

WASHINGTON, December 17, 1954.

Journal of Research of the National Bureau of Standards Vol. 54, No. 5, May 1955 Research Paper 2590

Stress-Strain Relationships in Yarns Subjected to Rapid Impact Loading: 2. Breaking Velocities, Strain Energies, and Theory Neglecting Wave Propagation[1]

Frank L. McCrackin, Herbert F. Schiefer, Jack C. Smith, and Walter K. Stone

The behavior of a yarn specimen fastened at one end to a head mass and at the other end to a small tail mass is analyzed for longitudinal impact of the specimen at the head. The analysis leads to a basic formula for "limiting breaking velocity," which is a characteristic property of the material and independent of the dimensions of the specimen. A simple procedure is described for obtaining its value. The values for cotton, nylon, and undrawn nylon yarns tested at room temperature are found to be 130, 228, and 550 meters per second, respectively. The practical application of the limiting breaking velocity to safety engineering is shown by an example on safety lines. Formulas are derived for computing energy to any strain under impact loading, and the computed values are found to agree with those obtained from the area under the impact load-extension curves.

1. Introduction

The first paper of this series [1][2] describes equipment and procedures for studying the stress-strain behavior of a yarn specimen subjected to tensional impact. In a typical test, a 65-cm specimen was attached at one end to a head mass and at the other end to a tail mass. The head was impacted at velocities between 10 and 100 m/sec, and subsequent behavior was recorded by high-speed photography.

The behavior of the yarn specimen after longitudinal impact is treated theoretically in this paper, neglecting wave-propagation effects. The results are compared with those obtained experimentally for several materials. The practical application of this work to safety engineering is indicated.

2. Theory

Figure 1 represents a test specimen terminated by a head and a tail. The equations of motion of these masses are derived in terms of the following symbols:

L = Length of specimen before impact.
w = Mass of specimen.
nw = Mass of tail.
mw = Mass of head.
x_{10} = Position of tail before impact, relative to a fixed origin, 0.
x_{20} = Position of head before impact, relative to a fixed origin, O.
t = Time after impact.
x_1 = Position of tail at time, t, relative to a fixed origin, O.
x_2 = Position of head at time, t, relative to a fixed origin, O.
x_c = Position of center of mass of the system at time, t, relative to a fixed origin, O.
ϵ = Strain in specimen.
F = Force acting on specimen at time, t.
v_0 = Velocity of head immediately after impact.

It is assumed here that $\frac{1}{2}w$ is concentrated at the head and the remaining $\frac{1}{2}w$ is concentrated at the tail of the specimen. Thus the problem actually treated is that of a mass-less specimen to which a head mass $(m+\frac{1}{2})w$ and a tail mass $(n+\frac{1}{2})w$ are attached.

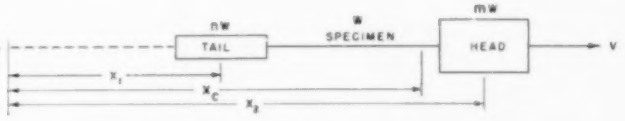

FIGURE 1. *Schematic drawing of test specimen for impact loading.*

The force equations, neglecting air friction,[3] are

$$F=(n+\tfrac{1}{2})w\frac{d^2x_1}{dt^2}, \tag{1}$$

and

$$F=-(m+\tfrac{1}{2})w\frac{d^2x_2}{dt^2}. \tag{2}$$

From definition of the center of mass, we obtain $(n+\frac{1}{2})wx_1+(m+\frac{1}{2})wx_2=(n+m+1)wx_c$.

Differentiating and eliminating w gives

$$(n+\tfrac{1}{2})\frac{dx_1}{dt}+(m+\tfrac{1}{2})\frac{dx_2}{dt}=(n+m+1)\frac{dx_c}{dt}. \tag{3}$$

Because $\epsilon L=(x_2-x_1)-(x_{20}-x_{10})$, we obtain by differentiation

$$\frac{dx_1}{dt}-\frac{dx_2}{dt}=-L\frac{d\epsilon}{dt}. \tag{4}$$

Solving eq (3) and (4) for dx_1/dt and dx_2/dt gives

$$\frac{dx_1}{dt}=\frac{dx_c}{dt}-\frac{(m+\frac{1}{2})L}{n+m+1}\frac{d\epsilon}{dt}, \tag{5}$$

and

$$\frac{dx_2}{dt}=\frac{dx_c}{dt}+\frac{(n+\frac{1}{2})L}{n+m+1}\frac{d\epsilon}{dt}. \tag{6}$$

[1] This work was sponsored by the Office of the Quartermaster General, Department of the Army, and was presented in part at the September 1953 and 1954 meetings of The Fiber Society, and also at the November 1954 meeting of the Society of Rheology.

[2] Figures in brackets indicate the literature references at the end of this paper.

[3] The force on the tail due to air friction was calculated to be approximately 1 percent of the yarn tension.

At maximum strain $\epsilon=\epsilon_m$ and $d\epsilon/dt=0$, therefore, $dx_1/dt=dx_2/dt=dx_c/dt$. That is, for a typical loading and unloading test under impact conditions, the velocity of the tail mass at the instant of maximum strain is equal to the velocity of the head, and both are equal to the velocity of the center of the total mass. As the total momentum imparted by the hammer to the head immediately after impact is $(m+\frac{1}{2})wv_0$, it follows from conservation of momentum that $dx_c/dt=(m+\frac{1}{2})v_0/(n+m+1)=$constant, which is also the velocity of the head and of the tail at maximum strain. The velocity of the head, therefore, decreases from v_0 immediately after impact to $(m+\frac{1}{2})v_0/(n+m+1)$ at the time of maximum strain. It is seen that this decrease is equal to $(n+\frac{1}{2})v_0/(n+m+1)$ and thus depends upon the values of n and m.

From eq (5) and (1), or (6) and (2), it follows that

$$\frac{d^2\epsilon}{dt^2}=-\frac{n+m+1}{(n+\frac{1}{2})(m+\frac{1}{2})}\frac{F}{Lw}.$$

Integration gives

$$\left(\frac{d\epsilon}{dt}\right)^2=-\frac{2}{Lw}\frac{n+m+1}{(n+\frac{1}{2})(m+\frac{1}{2})}\int_0^{\epsilon}Fd\epsilon+C.$$

At $t=0$, $\epsilon=0$, and $d\epsilon/dt=v_0/L$. Therefore, $C=v_0^2/L^2$ and

$$\left(\frac{d\epsilon}{dt}\right)^2=\frac{v_0^2}{L^2}-\frac{2}{Lw}\frac{n+m+1}{(n+\frac{1}{2})(m+\frac{1}{2})}\int_0^{\epsilon}Fd\epsilon. \tag{10}$$

At the maximum strain $\epsilon=\epsilon_m$ and $d\epsilon/dt=0$. It follows, therefore, that

$$\log v_0=-\tfrac{1}{2}\log\frac{(n+\frac{1}{2})(m+\frac{1}{2})}{n+m+1}+\log\sqrt{\frac{2L}{w}\int_0^{\epsilon_m}Fd\epsilon}. \tag{11}$$

In an impact test the specimen will break if the impact velocity, v_0, is large enough that the rupture strain, ϵ_r, is attained. The minimum breaking velocity, v_n, for a given n is the velocity just sufficient to cause the specimen to break when $\epsilon_r=\epsilon_m$. Under these conditions we have

$$\log v_n=-\tfrac{1}{2}\log\frac{(n+\frac{1}{2})(m+\frac{1}{2})}{n+m+1}+\log\sqrt{\frac{2L}{w}\int_0^{\epsilon_r}Fd\epsilon}. \tag{12}$$

Equation (12) expresses the minimum breaking velocity as a function of n. If ϵ_r and the shape of the stress-strain curve are both independent of the rate of straining, the expression under the radical sign is a constant having the dimensions of velocity squared. At high rates of straining the value of ϵ_r is less than that obtained at conventional testing rates. Also, the slope of the stress-strain curve is greater at higher rates of straining. However, for rates of straining of the same order of magnitude, these changes are small, and their effects compensate each other. Consequently, the area under the stress-strain curve should be essentially constant for the rates of straining considered here. Under these conditions a plot of $\log v_n$ versus $\log(n+\frac{1}{2})(m+\frac{1}{2})/(n+m+1)$ would be a straight line of slope $-\frac{1}{2}$.

By extrapolating from impact test data to the point at which $\log(n+\frac{1}{2})(m+\frac{1}{2})/(n+m+1)=0$, a characteristic velocity, v_b, is obtained; namely,

$$v_b=\sqrt{\frac{2L}{w}\int_0^{\epsilon_r}Fd\epsilon}. \tag{13}$$

If we let $\rho=$density of the specimen and $\sigma=$stress, eq (13) reduces to the form

$$v_b=\sqrt{\frac{2}{\rho}\int_0^{\epsilon_r}\sigma d\epsilon}. \tag{14}$$

It is thus seen that v_b is a quantity characteristic of the material itself, except for a possible dependence on the rate of straining.

Equation (14) can be rearranged in the form

$$\tfrac{1}{2}\rho v_b^2=\int_0^{\epsilon_r}\sigma d\epsilon, \tag{15}$$

which states that the kinetic-energy density in the specimen when traveling at velocity v_b is just equal to the strain-energy density required to break the specimen. We thus see that if the specimen is impacted at a velocity greater then v_b, it will always be broken. For this reason, we call v_b the limiting breaking velocity.

Von Kármán [2] derived a critical velocity, v_c, at which a filament will break immediately upon impact

$$v_c=\int_0^{\epsilon_r}\sqrt{\frac{1}{\rho}\frac{d\sigma}{d\epsilon}}d\epsilon. \tag{16}$$

This equation was obtained from a consideration of plastic and elastic wave propagation in a material for which the stress-strain curve is concave downward, and the stress is independent of the rate of straining.

The results calculated from eq (14) and (16) differ slightly. However, in the special case when Hooke's law is obeyed both eq (14) and (16) reduce to

$$v'=\epsilon_r\sqrt{\frac{E}{\rho}}. \tag{17}$$

This formula may be expressed in terms of the more familiar textile quantities of tenacity and percent elongation at rupture, namely,

$$v'=29.7\sqrt{\text{tenacity}\times\text{elongation}}, \tag{18}$$

where v' is in meters per second, tenacity is in grams per denier, and elongation is in percent.

Meredith [3] has obtained evidence that at high rates of straining the load-extension curves of some materials become more Hookean. These formulas thus assume considerable importance and by means of eq (18), estimates of the critical velocities of yarns may be computed from their tenacities and elongations at rupture under impact testing conditions.

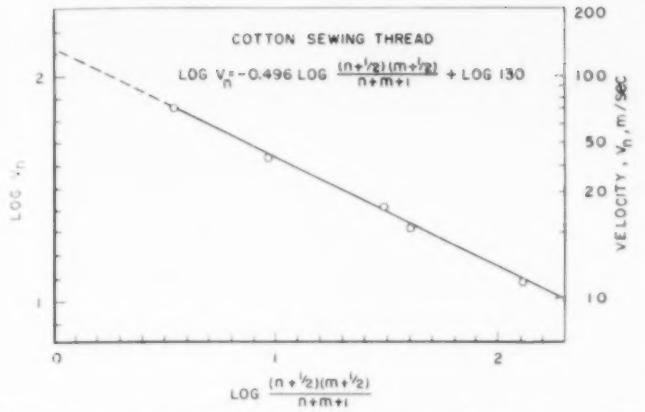

FIGURE 2. *Relationship between impact velocity to rupture, v_n, and head-tail mass parameter, $(n+\frac{1}{2})\ (m+\frac{1}{2})/(n+m+1)$, for cotton sewing thread.*

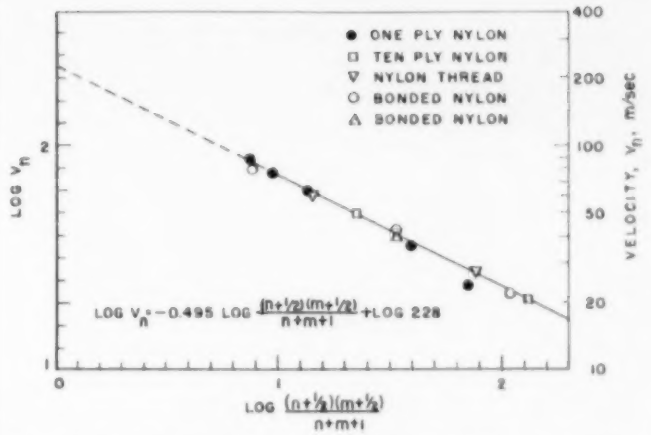

FIGURE 3. *Relationship between impact velocity to rupture, v_n, and head-tail mass parameter, $(n+\frac{1}{2})\ (m+\frac{1}{2})/(n+m+1)$, for nylon yarns and threads.*

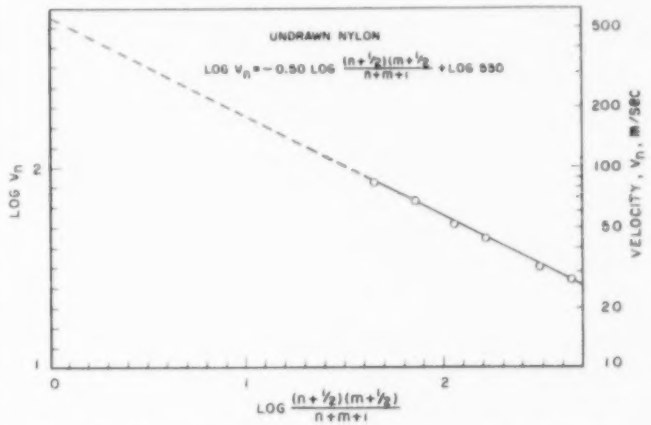

FIGURE 4. *Relationship between impact velocity to rupture, v_n, and head-tail mass parameter, $(n+\frac{1}{2})\ (m+\frac{1}{2})/(n+m+1)$, for undrawn nylon.*

In a subsequent paper [4] the behavior of the specimen after longitudinal impact is treated by a theory that considers the effects of wave propagation. This treatment shows that the results given in this paper for nonwave theory are valid when the tail mass is greater than $40w$. For tail masses less than $40w$, the effects of wave propagation may become appreciable and must be considered in the theoretical treatment.

3. Experimental Results

Experimental values of v_n corresponding to different values of n were obtained on a number of different materials. These values of log v_n are plotted in figures 2, 3, and 4 against $\log(n+\frac{1}{2})(m+\frac{1}{2})/(n+m+1)$. These plots are straight lines having the empirical equations

$$\log v_n = -0.496 \log \frac{(n+\frac{1}{2})\,(m+\frac{1}{2})}{n+m+1} + \log 130$$

for cotton thread

$$\log v_n = -0.495 \log \frac{(n+\frac{1}{2})\,(m+\frac{1}{2})}{n+m+1} + \log 228$$

for nylon yarn and threads

$$\log v_n = -0.500 \log \frac{(n+\frac{1}{2})\,(m+\frac{1}{2})}{n+m+1} + \log 550$$

for undrawn nylon.

It should be noted that the slope of each line represented by these equations is very close to $-\frac{1}{2}$ in accordance with eq (12) for log v_n.

4. Design of Safety Lines

The empirical equation derived for log v_n has many practical applications. Consider, for example, a safety line of length, L, that connects a construction worker to a rigid point of the structure. Under these conditions, m is infinite. The maximum free fall of the worker would be $2L$, and the maximum free-fall velocity $2\sqrt{gL}$. As m becomes infinite, eq (12) reduces to

$$\log v_n = -\tfrac{1}{2} \log(n+\tfrac{1}{2}) + \log v_b. \qquad (19)$$

Making the assumption (which must be checked by experiment) that the safety line behaves under impact like the single yarn considered in the derivation of eq (19), substituting $v_n = 2\sqrt{gL}$ and solving for n, one obtains

$$n = \frac{v_b^2 - 2gL}{4gL}.$$

If v_b is 200 m/sec for the material of the safety line, $L=10$m, and $g=9.8$ m/sec^2, the computed value of n is 101. If the weight of the worker, nw, is 202 lb, the minimum weight of 10 m of safety line, w, to just support the worker at impact is 2 lb, according to this computation.

This weight is approximately that of a rope ½ in. in diameter [5]. A nylon rope 7/16 in. in diameter has a static breaking strength of 4,000 lb [6], or 20 times

the weight of the worker. However, under the dynamic conditions just assumed, a nylon rope with $v_b=200$ m/sec would have no factor of safety whatever according to this computation.

If v_b for the material of the safety line is 100, $n=25$, and for the same weight of worker, w would have to be 8 lb. This weight is approximately that of a rope about 1 in. in diameter [5]. A manila rope 1 in. in diameter has a static breaking strength of 11,000 lb, or 50 times the estimated weight of the worker. Again, under dynamic conditions, this manila rope would not provide a reasonable factor of safety according to this computation. Results obtained by Newman [6] showed that a $\frac{9}{16}$-in.-diam sisal rope 10 ft long broke when a weight of 142 lb was dropped a height of only 20 ft.

5. Energy of Straining

The energy per unit length, Q, to stress the specimen to a strain ϵ is given from eq (10) by the equation

$$Q=\int_0^{\epsilon} F d\epsilon=\frac{Lw}{2}\frac{(n+\frac{1}{2})(m+\frac{1}{2})}{n+m+1}\left[\left(\frac{v_0}{L}\right)^2-\left(\frac{d\epsilon}{dt}\right)^2\right], \quad (20)$$

where $d\epsilon/dt$ is the slope of the strain-time curve at the strain ϵ. If the specimen is not ruptured but is loaded to a maximum strain, ϵ_m, and then unloaded, the energy, Q_m, to the maximum strain, ϵ_m, is given by the equation

$$Q_m=\int_0^{\epsilon_m} F d\epsilon=\frac{Lw}{2}\frac{(n+\frac{1}{2})(m+\frac{1}{2})}{n+m+1}\left(\frac{v_0}{L}\right)^2, \quad (21)$$

since $(d\epsilon/dt)_{\epsilon=\epsilon_m}$ is zero. If the specimen is ruptured, the energy, Q_r, to the rupture strain, ϵ_r, is given by the equation

$$Q_r=\int_0^{\epsilon_r} F d\epsilon=\frac{Lw}{2}\frac{(n+\frac{1}{2})(m+\frac{1}{2})}{n+m+1}\left[\left(\frac{v_0}{L}\right)^2-\left(\frac{d\epsilon}{dt}\right)^2_{\epsilon=\epsilon_r}\right] \quad (22)$$

The value of $(d\epsilon/dt)_{\epsilon=\epsilon_r}$ will be zero, if the impact velocity of the head is just sufficient to produce rupture. Above this velocity $(d\epsilon/dt)_{\epsilon=\epsilon_r}$ is a positive quantity.

By means of eq (20), (21), and (22), it is possible to compute Q, Q_m, and Q_r from the conditions of a test. For Q_m it is only necessary to know the velocity, v_0, of the head at impact. For Q and Q_r, the value of $d\epsilon/dt$ and $(d\epsilon/dt)_{\epsilon=\epsilon_r}$ must be known in addition to the value of v_0. The values of v_0, $d\epsilon/dt$, and $(d\epsilon/dt)_{\epsilon=\epsilon_r}$ are readily obtained from the positions of the head and of the tail on the high-speed motion pictures taken during the test. The energy values computed by means of these equations for different materials and impact testing conditions are plotted in figure 5 against those derived from the area of the impact-load–extension curves. The plotted points fall near a straight line having a slope equal to 1.

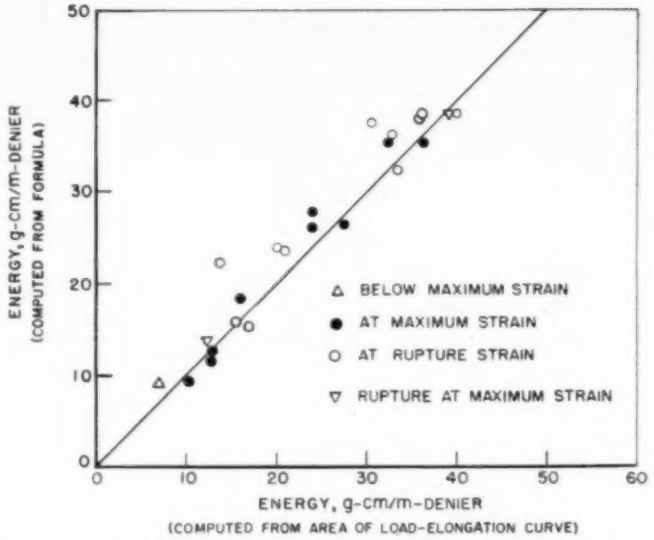

FIGURE 5. *Energy values computed from formulas plotted against those based upon the area under the impact load-extension curves.*

6. Summary and Conclusions

The theoretical treatment given in this paper for longitudinal impact of a yarn leads to a formula for the limiting breaking velocity that is a characteristic property of the material and is independent of the dimensions of the specimen. A specimen impacted at a velocity greater than its limiting breaking velocity will always be broken. A simple procedure is described for obtaining this limiting breaking velocity from impact-test data, and results are given for cotton, nylon, and undrawn nylon yarns. The potential importance of the limiting breaking velocity to safety engineering is indicated by its application to estimates of margin of safety of rupture of safety lines for construction workers. The theoretical treatment also leads to formulas for obtaining energy to any given strain, including rupture strain, under different impact conditions. These values agree reasonably well with those obtained from the area under the impact-load-extension curves.

7. References

[1] Walter K. Stone, Herbert F. Schiefer, and George Fox, Stress-strain relationships in yarns subjected to rapid impact loading: 1. Equipment, testing procedure, and typical results, J. Research NBS **54,** 269 (1955) RP2589.

[2] T. von Kármán and P. Duwez, Propagation of plastic deformation in solids, J. Appl. Phys. **21,** 987 (1950).

[3] R. Meredith, The effect of rate of extension on the tensile behavior of viscose and acetate rayons, silk, and nylon, J. Textile Inst. **45,** T30 (1954).

[4] Jack C. Smith, Frank L. McCrackin, and Herbert F. Schiefer, Stress-strain relationships in yarns subjected to rapid impact loading: 3. Effect of wave propagation, J. Research NBS **55** (in press).

[5] Sanford B. Newman and John H. Curtiss, A statistical analysis of some mechanical properties of manila rope, J. Research NBS **39,** 551 (1947) RP1847.

[6] Sanford B. Newman and Helen G. Wheeler, Impact strength of nylon and sisal ropes, J. Research NBS **35,** 417 (1945) RP1679.

WASHINGTON, December 17, 1954.

Journal of Research of the National Bureau of Standards Vol. 54, No. 5, May 1955 Research Paper 2591

Waterdrop Collisions With Solid Surfaces

Olive G. Engel

An approach is described to the difficult problem of the dynamics of an impinging water sphere. The flow in the impact plane is traced chemically. The stages in the collapse of the water mass and of its radial flow are shown in photographs that were taken with a high-speed motion-picture camera. Empirical determinations of the time dependence of the impact force and of the radial flow velocity are reported. The possible occurrence of cavitation in the radial flow is considered. A semiempirical analysis based upon various simplifying assumptions leads to equations for the maximum impact pressure and for the rate of spread of the water after the collision.

1. Introduction

Erosion by waterdrop impact has recently received attention because of the damage that is done to high-speed aircraft on flying through rain. The problem is not new. Similar erosion is produced in steam turbines by the waterdrops in wet steam.

The destructive force causing this erosion results from the collision of the solid surface with the waterdrop. At high impact velocities a waterdrop acts as though it were a hard sphere. Unlike a sphere of hard material, it undergoes an outward radial flow of very high velocity as a result of the collision.

The question as to the order of magnitude of the pressure that is developed in collisions of waterdrops against solid surfaces has been discussed since the first studies of this erosion were begun approximately 30 years ago. Efforts have been made both to calculate the pressure from theoretical considerations and to measure it experimentally.

2. Behavior of a Liquid Drop on Collision With a Flat Solid Surface

The process of collision of one solid against another solid is well known in elasticity theory. The collision of small solids with a body of liquid has also been investigated in water-entry problems. The collision of liquid drops against a solid surface, however, has been studied very little. Some preliminary work for the purpose of obtaining a better understanding of waterdrop-to-solid collisions is described in this paper. This work includes (1) a chemical mapping of the radial water flow in the impact plane, (2) the use of high-speed motion-picture photography to "stop" the motion of the drop sufficiently during the collision so that the stages in the transition from vertical to radial flow can be observed, and (3) the use of schlieren photography to study details in the radial flow. The following discussion applies to the case of collision of a waterdrop with a flat solid surface.

2.1. Map of the Radial Water Flow

Worthington [1] [1] with the aid of spark photography made a study of the forms assumed by drops of liquids (mainly milk and mercury) after a vertical fall from heights up to 11 in. onto a horizontal surface. A tendency toward formation of radial arms was found by Worthington to increase both with the height of fall and with the size of the drop.

The radial flow of a waterdrop was mapped chemically at the National Bureau of Standards. To accomplish this, a very small crystal of sodium dichromate held on the point of a needle was placed in the bottom surface of a waterdrop just before it fell from a flat-nosed pipet. The solution of this oxidizing agent is heavier than water and remained in the bottom of the drop. The drop was then allowed to fall onto a glass plate covered with a filter paper that was previously wet with acidified starch and potassium iodide solutions. A typical starch-iodide print of the radial flow from a waterdrop that fell approximately 1.5 ft is shown in figure 1. The water that struck first, and which contained the sodium dichromate, washed to the periphery of the flow, as can be seen by the stronger starch-iodide color there. The water that struck last essentially did not flow.

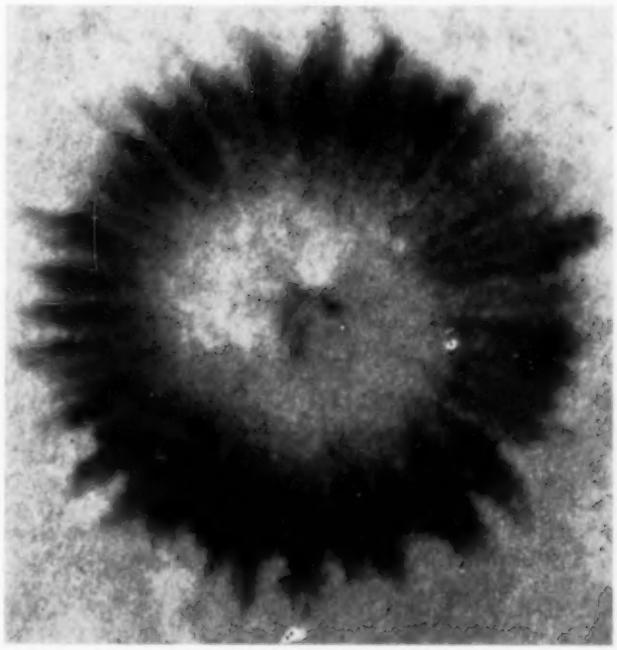

FIGURE 1. *Starch-iodide trace of the radial flow of a waterdrop after collision with a solid surface.*

[1] Figures in brackets indicate the literature references at the end of this paper.

The radial arms in the structure show that the flow was channeled. It is conceivable that these channels are a result of the viscous drag between the solid surface and the flowing liquid, as was suggested by Worthington [2]. On the other hand, the observation of Worthington that the number of channels increases both with the size and with the height of fall of the drop suggests that the number of them may be related to the kinetic energy of the drop.

2.2. Stages in the Collapse of a Waterdrop After Collision

High-speed motion pictures can stop sufficiently the movement of a waterdrop after it has collided with a solid surface so that the horizontal flow can be observed. Figures 2, 3, 6, 7, and 9 are enlargements from high-speed moving pictures that were taken by T. C. Hellmers, Jr., and Harold Goodman, both of the Diamond Ordnance Fuze Laboratory, and by Warren P. Richardson of the NBS Technical Reports Section. The camera used is capable of taking 15,000 frames per second. The operating velocity at which any incident is photographed can be computed from the 60-cycle timer marks along the border of the film.

The steps in the collision and flow of a waterdrop after free fall through distances of about 1.5 ft and of about 20 ft are shown in figures 2 and 3, respectively. For the waterdrop collisions shown in these figures a very small crystal of sodium dichromate was placed in the bottom surface of the drop, and the drop was allowed to fall against a glass plate covered with a filter paper that was previously wet with acidified starch and potassium iodide solutions. A waterdrop oscillates between a vertical and a horizontal elongation as it falls. The collision shown in figure 2 occurred while the drop was elongated vertically; that shown in figure 3 occurred while the drop was elongated horizontally. It can be concluded from these pictures that the head of liquid of the drop, before it enters into radial flow, shows an ability to resist a change of shape during collision with a solid. This may be a result of its inertia, or of its viscosity, or surface tension.

2.3. Schlieren Pictures of Impinging Waterdrops

To accelerate waterdrops to their terminal velocity in air by free fall under the force of gravity, a tube was installed in a staircase well to extend through three stories of the Industrial Building of the National Bureau of Standards. This tube served the purpose of shielding the waterdrops from air currents so that they could be made to fall with little deviation on a predetermined spot on a glass plate located at the lower exit of the tube. A flat-nosed pipet, from which the drops originated, was mounted at the top of the tube.

If the solid surface against which the waterdrop is allowed to impinge is a glass plate, the stages in the radial flow of the drop can be photographed through the plate itself. A complete schlieren system was found to produce pictures from which the most infor-

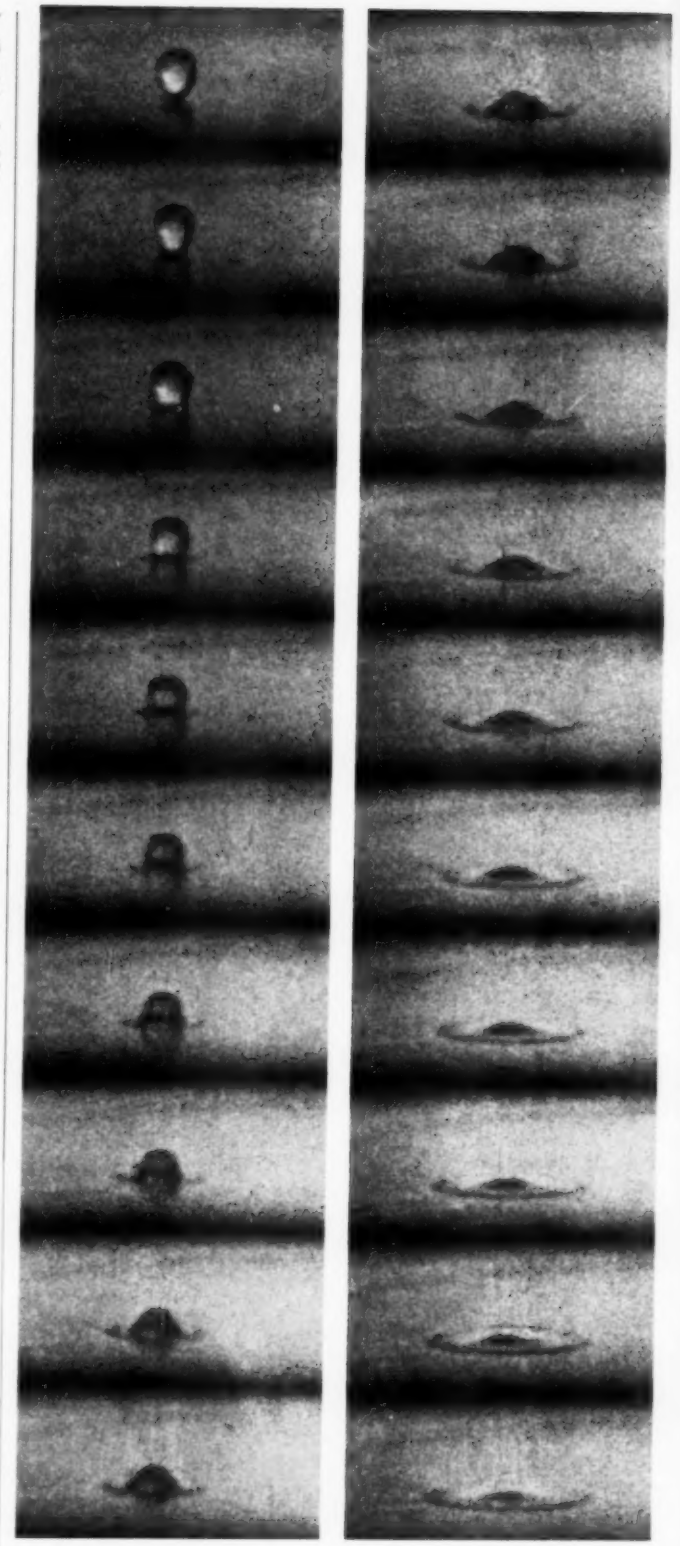

FIGURE 2. *Stages in the flow of a waterdrop that fell from a height of approximately 1.5 feet.*

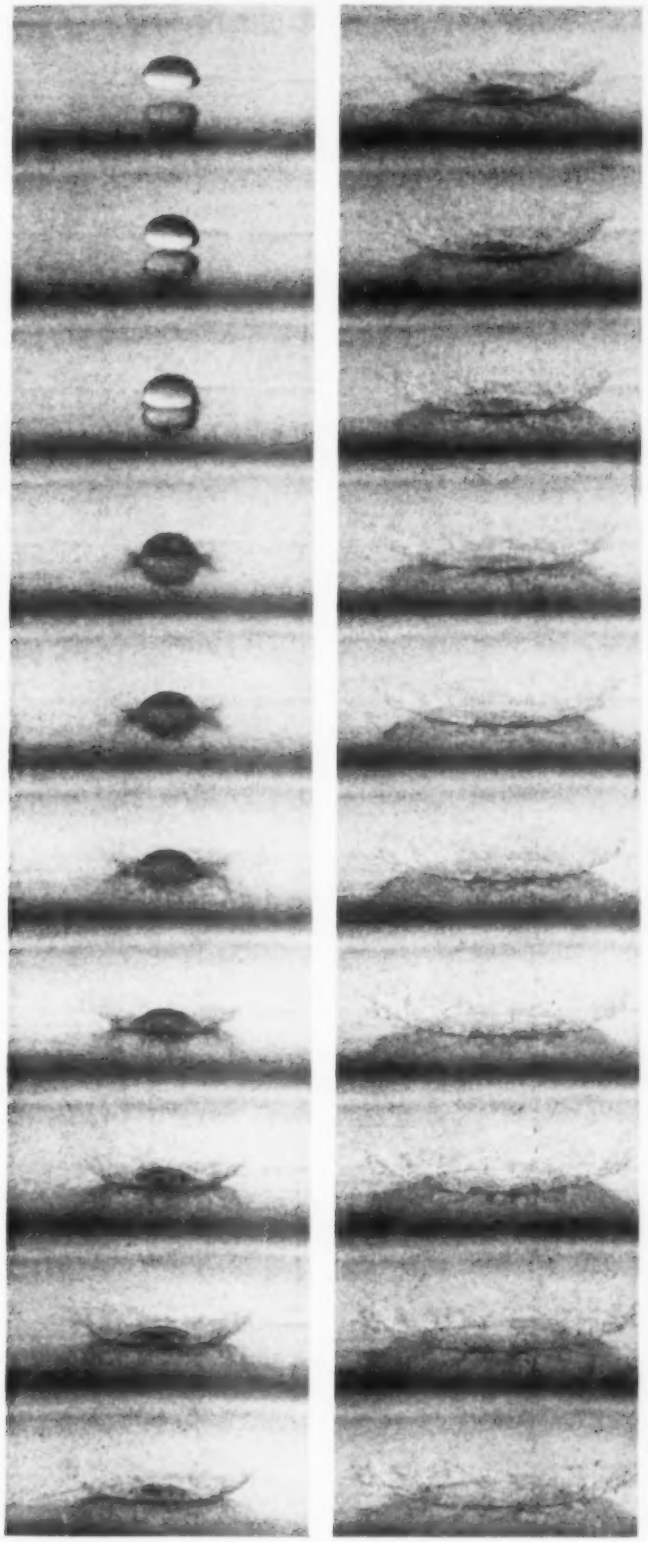

FIGURE 3. *Stages in the flow of a waterdrop that fell from a height of approximately 20 feet.*

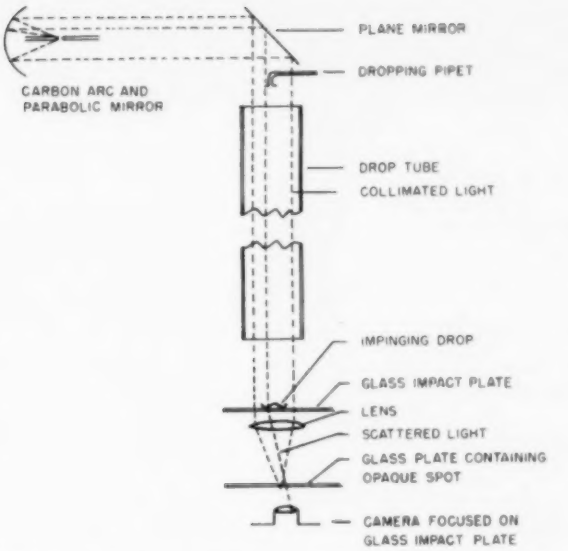

FIGURE 4. *Elements of a schlieren system for photographing impinging waterdrops.*

mation could be obtained. A sketch of the elements of the arrangement that was used is shown in figure 4. The arrangement was planned by Roland V. Shack of the NBS Optical Instruments Section.

a. Schlieren Arrangement for Photographing an Impinging Waterdrop

The light source was a carbon arc searchlight that operated on a 40-amp current. The light was collimated by a parabolic mirror and was directed down the tube, through which the waterdrops fell, by means of a front-surface plane mirror. The tube was dyed black on the inside to reduce light scattering. The degree of collimation of the light was further improved by a circle of cardboard that was fastened to the exit of the tube and that allowed only the central core of the collimated beam to pass through to the glass plate.

The collimated light was transmitted through the glass plate and was focused by a lens. The sharp spot of light, which formed at the focal point of the lens, was received on an opaque barrier that had the same size and shape as the spot of light itself. This barrier was made by allowing the spot of light to fall on a spectroscopic plate that was rigidly mounted at the focal point of the lens in complete darkness. The opaque barrier served the purpose of a schlieren knife edge. The camera was mounted below the opaque barrier and was focused on the upper surface of the glass plate. Theoretically, only the light that was scattered by the impinging waterdrop would be deflected so as to enter the lens of the camera.

b. Interpretation of the Schlieren Patterns

To show how the light that was scattered by an impinging waterdrop would appear in pictures taken with the schlieren arrangement, four glass models of waterdrops were fashioned by L. Testa of the NBS Glassb lowing Shop. The models ranged

337361 55 3

from a solid glass sphere to an almost flattened glass disk. They are shown in figure 5, along with the corresponding photographs that were made when they were placed on the glass plate of the schlieren arrangement. The pictures numbered 1 through 4 in figure 5 are the glass models. The pictures having the corresponding primed numbers are the schlieren patterns that the models produced. A 50-mm lens was used to photograph the schlieren patterns. The lens was kept at its widest aperture so that the depth of field was very short.

In picture 1 of figure 5 a hollow glass bead (black pointer) is shown with the solid glass bead. The schlieren patterns obtained from these beads show how difficult it is to tell the difference between a bubble in water and a protuberance from the water surface. The hollow bead produces only a somewhat larger high light in the schlieren pattern than the solid bead produces. Picture 2 of figure 5 shows a glass model of a waterdrop in the first stage of radial flow. The schlieren pattern produced by it is the same as that produced by the solid glass sphere but has a slightly larger diameter. A small difference in diameter is meaningful in this case because the geometry of the schlieren arrangement remained constant.

Pictures 3 and 4 of figure 5 show glass models of a waterdrop in more advanced stages of radial flow. The glass model in picture 4 has a ridge at the periphery of the radial flow, whereas that shown in picture 3 does not. Comparison of the structure of these models with their schlieren patterns shows that a flat area appears light in the schlieren pattern, regardless of whether it exists on a ridge or in a depression, whereas an area that has any degree of inclination to the reference plate on which the glass model is resting appears dark. Apparently the only way that the presence of a ridge or a depression can be identified is by the sloping area leading to it. The spherical residue in the center of the glass models in pictures 3 and 4 represents an inclined area and appears dark in pictures 3′ and 4′. In pictures 1′ and 2′ the schlieren patterns are also dark as is now expected because the glass models that produced them (pictures 1 and 2) have no area that does not have an inclination to the reference plane.

c. Increase in Size of the Central High Light

The schlieren patterns shown in pictures 1′ and 2′ of figure 5 have a central high light as do also those shown in pictures 3′ and 4′. This results because the glass sphere or spherical residue acts as a lens. If the spherical residue should become progressively more flattened, it should behave as a lens of longer focal length, and the high light should be seen to become larger and more diffuse. Although this effect is observed in schlieren pictures of the collision of real waterdrops with the glass plate, it is not observed in pictures 1′ through 4′ probably because the degree of curvature of the spherical residue in the glass models is not sufficiently different.

The first 10 frames of a collision incident of a real waterdrop impinging against a glass plate as photographed at a small oblique angle above the glass plate are shown in figure 6. As soon as the waterdrop contacts the glass and flows at all, it becomes a combination lens in which the lower lens has a small central flat area. Under this condition two foci exist, namely, that of the double-convex lens and that of the single planoconvex lens. As the solid surface moves further through the waterdrop the intensity at the focus for the double-convex lens decreases and that at the focus for the single planoconvex lens increases. When the head of water that

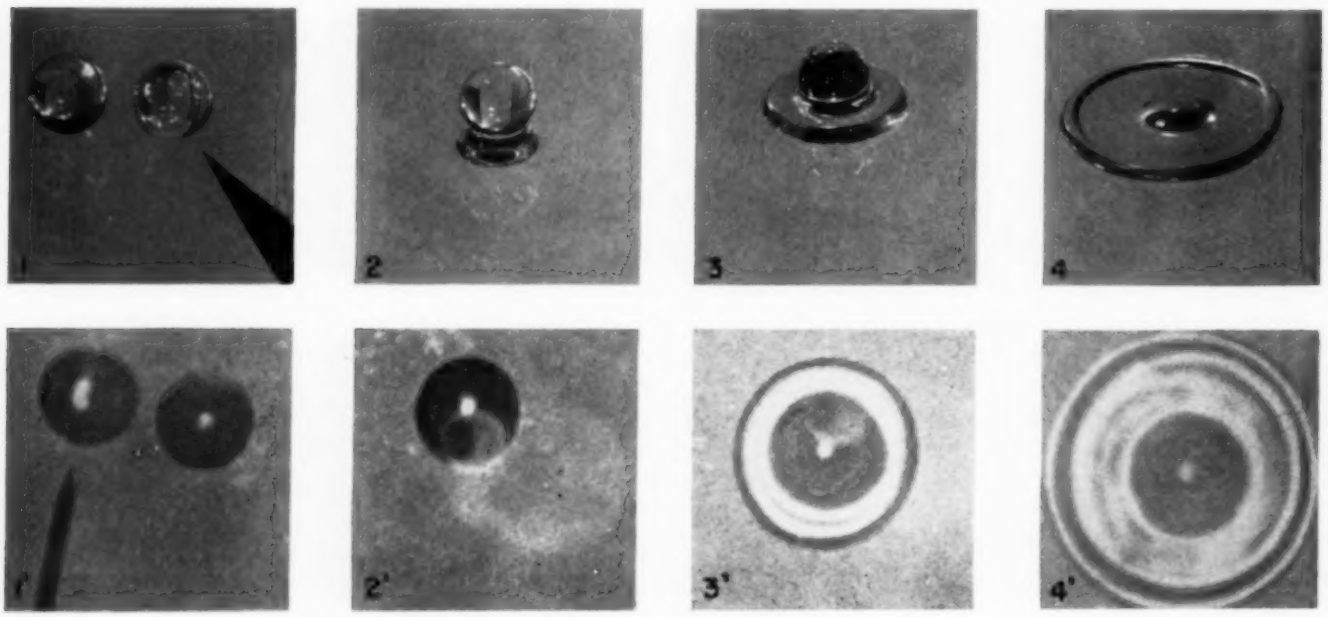

FIGURE 5. *Glass models of waterdrops and their schlieren patterns (primed numbers).*

remains of the drop has decreased to a hemisphere, only the focus for the single planoconvex lens exists.

The focal length of a sphere of water measured from the point of contact with the flat surface on which it is resting, for rays making a small angle with the axis, is equal to its radius. The radius of curvature of the top of the drop in the first frame of figure 6, as found by trial and error with dividers, was 0.36 cm. The focal length of a single planoconvex lens of water measured from the plane side, which is in contact with the flat surface on which it is resting, for light that is incident on the curved surface of it, is 2.25 times its radius of curvature. As the radius of curvature of the water hemisphere that remains of the drop in the fifth frame of figure 6 was 0.51 cm, its focal length at this stage of the collision was about 1.15 cm. The difference in the focal length of the water lens as it exists in frame 1 and in frame 5 is 0.79 cm. As the depth of field of the camera used to take the schlieren photographs was less than 0.2 cm, it seems reasonable that a perceptible increase in the size of the high light in the center of the schlieren patterns of a waterdrop should be observed during the course of a collision between the waterdrop and a glass plate. This effect can, indeed, be observed in frames 1 to 13 of figure 7.

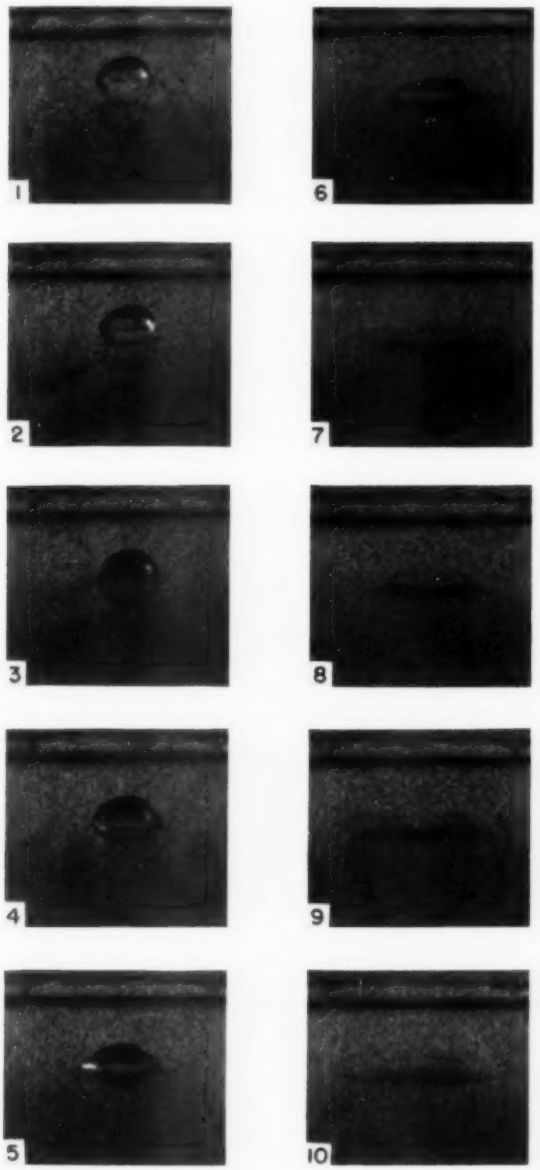

FIGURE 6. *Stages in the collision of a waterdrop with a glass plate.*

d. Lifetime of the Head of Water of a Drop That Collides at Its Terminal Velocity in Air With a Glass Plate

The glass models were placed directly in the center of the schlieren arrangement in line with the opaque barrier and with the center of the camera lens. The waterdrops were usually displaced from this position. This may explain why the schlieren patterns of the waterdrops show an additional high light on the side of the head of water of the drop as long as it exists as such. When the head of water just disappears so that only a disk of water in radial flow remains, the side high light and the central high light merge. For waterdrops impinging against a glass plate at their terminal velocity in air, the number of frames from the first point of impact to the merging of the two high lights indicates that the time required for the disappearance of the head of water of the drop is about 1 msec (millisecond).

The merging of the high lights seems to be accompanied by a flash of light, which unfortunately obscures the details in the radial flow for a space of 6 or 7 frames. The explanation of the light flash seems to be that the water lens at this stage of the flow of the drop acts in conjunction with the glass lens of the schlieren system to allow light to pass around the opaque barrier. The event occurs consistently.

e. Structures in the Radial Flow

On inspection of schlieren patterns produced by collision incidents between a glass plate and impinging drops, such as those shown in figure 7, it is seen that the radial flow of the liquid appears dark. With reference to the observations made in regard to the schlieren patterns produced by the glass models, this appears to indicate that the radial flow of the liquid has some degree of inclination with respect to the glass plate. Worthington [1] made observations with drops of milk and mercury for low heights of fall that show that the liquid in radial flow is deepest at the periphery (see fig. 15).

In the schlieren pictures the periphery of the radial flow is bounded by a beady white line. The beady character of the periphery of flow can be detected as early as frame 5 in figure 7. With reference to the schlieren patterns produced by the glass models, a white area is either the top of an elevation or the bottom of a depression. In the case of the white boundary of the radial flow it is most likely an elevated ridge. This conclusion seems to be supported in the pictures shown in figure 2.

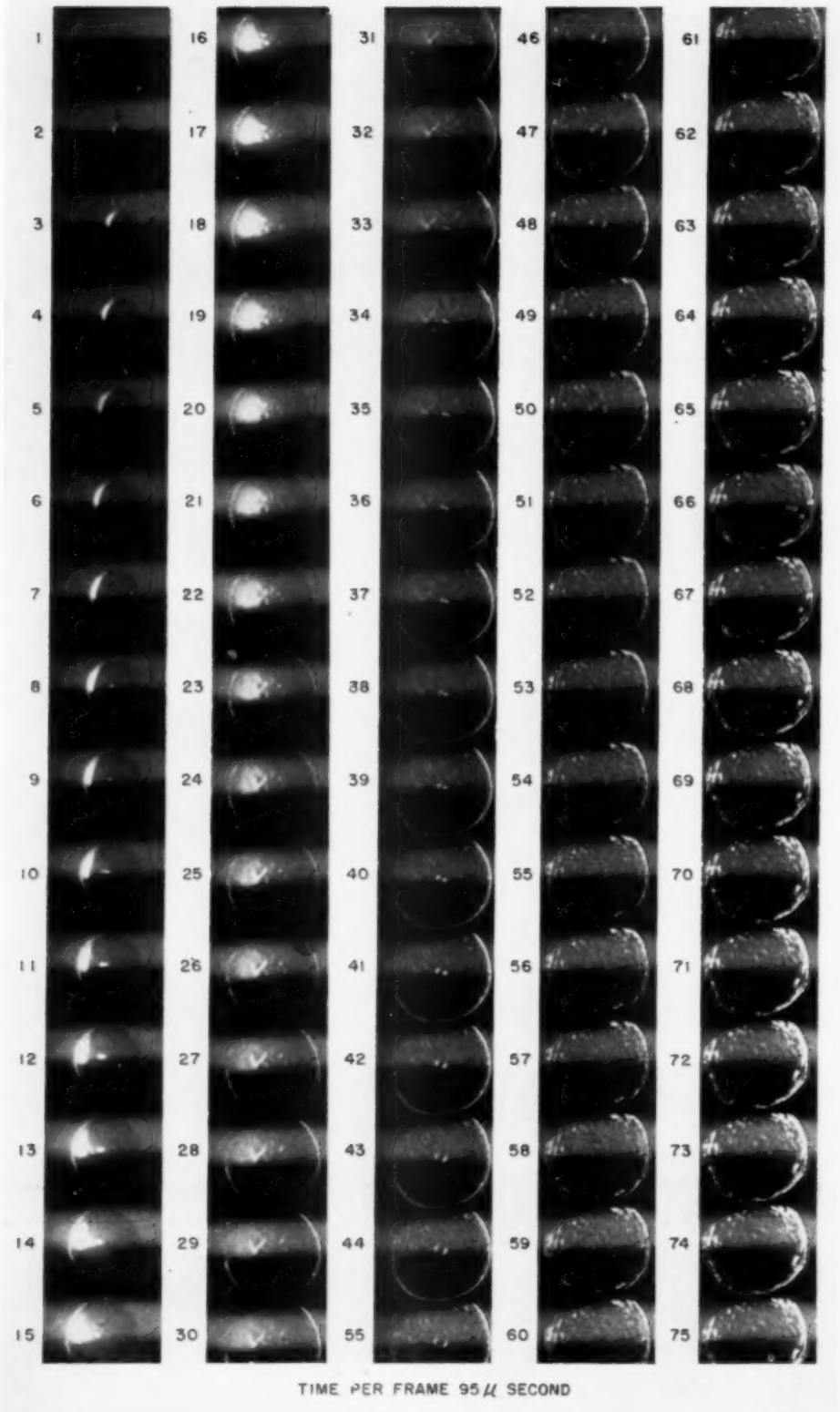

FIGURE 7. *Schlieren patterns produced by the collision of a waterdrop with a glass plate*

FIGURE 8. *Ridges formed in the flow of a deforming lead pellet after collision.*

Waves that run out over the radial flow can also be seen when high-speed pictures of a collision of a waterdrop with a glass plate are viewed with a projector. This effect is not visible in still enlargements.

Finally, inspection of pictures of various collision incidents between waterdrops and a glass plate shows that structures of some kind develop in the radial flow. The development of these structures follows the same general course. The central high light increases in size and finally takes on a definite structure. The structure grows in complexity and, after the central and side high lights of the drop merge, finally appears as separate white spots. That these white spots or areas are probably ridges and depressions can be seen from the flow that a deforming lead pellet undergoes after impact at very high speed against a metal plate. The flow of a deforming lead pellet is shown in figure 8. In the case of the radial flow of water after impact, these ridges eventually vanish.

The explanation of why these ridges should form is not clear. The compressional wave started by the impact moves through the drop at the speed of sound in water and reflects from the opposite side of it as a tension wave. Thereafter it changes from tension to compression and back to tension alternately at the end of each *round trip* through the head of water that remains of the drop. It is possible that a standing wave may be produced as a consequence of the boundary conditions imposed on this alternate wave of compression and tension. On the other hand, it is possible that a solution that would predict standing waves may result from the continuity equation and the boundary conditions of the radial flow in the impact plane.

f. Cavitation in the Radial Flow

One of the most difficult aspects to understand in the problem of the erosion of durable structural materials as a result of high-speed waterdrop impingement is how initiation centers develop. It has been suggested by Albrecht Herzog of the Wright Air Development Center that incipient cavitation erosion may provide a first surface roughness from which erosion that results from waterdrop impingement could progress. A first surface roughening is observed both in the case of cavitation erosion and in the case of erosion by waterdrop impact. From this standpoint it is of interest to know whether or not any evidence of cavitation can be detected in the radial flow of a waterdrop after collision with a solid surface.

Cavitation is the formation of bubbles in a liquid. It occurs when the pressure on a liquid or in a small volume in a liquid drops below the value of the vapor pressure of the liquid at the temperature in question. The cavitation process itself is the spontaneous growth of gas nuclei (which already exist in the liquid) due to vaporization of the liquid across the liquid-vapor interface that each growing nucleus provides. When the pressure on the liquid is raised, or when the bubbles move out of a local low-pressure region in the liquid to a region of high pressure, the bubble-cavities collapse. It is the collapse of the cavities that produces the type of damage known as cavitation erosion.

There are at least two ways by means of which it is possible to explain theoretically how the conditions that produce cavitation may develop in a liquid drop after it collides with a solid surface at a velocity of sufficient magnitude. The first possible explanation is based on the very rapid radial flow of the liquid. It suggests that when the head of liquid of the drop has just disappeared into radial flow, the continued outward flow of the liquid under its own monemtum will produce a drop in pressure at the center of the spreading liquid disk. If the pressure at the center of the spreading liquid disk should fall below the vapor pressure of the liquid in question, cavitation may occur. This explanation has been advanced by Dr. Herzog. That a liquid drop may break in the center of the radial flow is shown in the work of Worthington [1]. He found that impinging drops of mercury break in the center and form a ring rather than a solid disk of liquid.

The second possible explanation of how cavitation conditions may be realized is based on the alternating wave of compression and tension that exists in the head of liquid that has not yet become part of the radial flow of the drop. At the first instant of collision a wave of compression, which is initiated by the impact, moves through this head of liquid to the top of the drop. Here it reflects from the free liquid-to-air surface as a tension or negative pressure wave. This negative pressure wave moves back through the

drop to the impact surface. It must, in fact, be focused to a very small area of the impact surface by the curvature of the top of the drop in much the same way as ultrasonic waves in water may be focused by a watch glass. The returning negative pressure wave adds algebraically to the compressional wave that is still being initiated at the impact surface as a result of the collision. Since, however, the impact pressure has been decreasing steadily during the time interval in which the first compressional wave front made its round trip through the waterdrop and returned as a negative pressure wave, the net pressure is negative. The extent to which the net pressure is negative depends on the rate of decrease of the impact pressure with time. This explanation of how cavitation conditions may be produced in a liquid drop after collision with a solid surface is due to the late Francis E. Fox of the Catholic University.

Some slight evidence was found for what might be cavitation in schlieren pictures of a waterdrop collision with a glass plate. At the suggestion of Virginia Griffing of the Catholic University, waterdrops saturated with argon gas were used in an effort to show that the evidence that was observed was actually produced by bubbles in the water. Dr. Griffing has found that cavitation occurs readily in water that has been saturated with argon gas.

Enlarged pictures of 75 consecutive frames from one of the collisions of a drop of argon saturated water with the glass impact plate are shown in figure 9. In this figure the life cycle of a bubble can be followed from frame 19 to frame 33. The appearances, which are described here, are more readily seen in the original photographs than in the halftone reproductions. The bubble appears slightly to the right of and below the center of the radial flow in frame 19. It grows in size and distinctness, then diminishes, and eventually vanishes in frame 33. As the time per frame for this collision incident was 93 μsec, the lifetime of this bubble was 1.4 msec. This is a reasonable lifetime for a cavitation bubble [3]. This bubble made its appearance shortly after the head of water of the drop vanished into radial flow in frame 14.

A second bubble life cycle can also be followed in figure 9. This bubble appears in frame 24 on a level with the bubble that has just been discussed but about ⅛ in. from the periphery at the left side of the radial flow. It increases in brightness and then dims virtually to extinction in frame 34. The lifetime is 0.9 msec. In frame 42 a white spot, which may be the same bubble, starts to increase in brightness. It is about 1/16 in. from the left periphery of the radial flow. It continues to increase in brightness and, at frame 60, that is, 1.7 msec after its reappearance, it drifts into the left periphery of the radial flow.

Two bubbles slightly below and to the left of the center of the radial flow can be observed from frame 31 to frame 45. In frame 46 the characteristic white semicircle which seems to be associated with a surface bubble (possibly due to the raised rim of water that accompanies such a bubble) appears. One of the bubbles has broken by frame 52, as is seen by the train of ripples that forms from the white semicircle. The other bubble becomes obscure at about frame 59 or 60. A bubble floating on a liquid surface depresses the liquid level below it and is accompanied by a stable meniscus or raised rim of liquid at its periphery. If the bubble collapses, the differences in liquid level are no longer stable. This condition will produce waves. These waves are predominantly capillary waves since the wave length is small.

The collision incident for a drop of ordinary hydrant water against the glass impact plate is shown in figure 7. A small white spot can be seen very slightly to the right of the center of the radial flow in frame 14. This spot grows in brightness to about frame 25. It then becomes progressively dimmer until it disappears at about frame 40. This is a lifetime of about 2.5 msec. The rise of a bubble to the surface and its collapse in the surface can also be traced in this figure. The first evidence of this bubble is in frame 29 at about the center of the radial flow. By frame 42 it has developed into two white semicircles enclosing a small white spot. As has already been noted, this structure seems to be typical of a surface bubble. In frame 46 the tiny central white spot is more diffuse and the enclosing semicircular white spots have started to split into semicircular lines. In the succeeding frames these lines spread out. In frame 54 they are almost concentric circles such as are formed when a pebble is dropped in a pool. Some vestige of this configuration can still be seen in frame 73.

The fact that the bubble life cycles that have been pointed out seem to start after the head of water of the drop has vanished must not be construed as invalidating the second of the explanations of how cavitation conditions may be realized in a liquid drop after impact against a solid surface. This was called to my attention by Phillip Eisenberg of the Office of Naval Research. It may be necessary for the negative pressure wave to return to the impact surface many times before the bubble nuclei have sufficient time to grow to a size that can be seen.

In evaluating the evidence, which has just been presented, for the possible existence of cavitation in a waterdrop after collision with a solid surface, it is important that the effect of the impact velocity should be considered. The terminal velocity of a large waterdrop in air is [4] about 26.9 ft/sec (820 cm/sec). One can hardly extrapolate the evidence for cavitation found at this velocity to what may be found at airplane flight velocities, for example, which are of the order of 900 ft/sec. At the high impact velocities at which erosion is actually observed as a result of waterdrop impact the negative pressure would be very much increased and the possibility that cavitation may occur consequently much enhanced. This would follow from either of the explanations of how cavitation conditions may be produced as a result of the impact of a waterdrop against a solid surface.

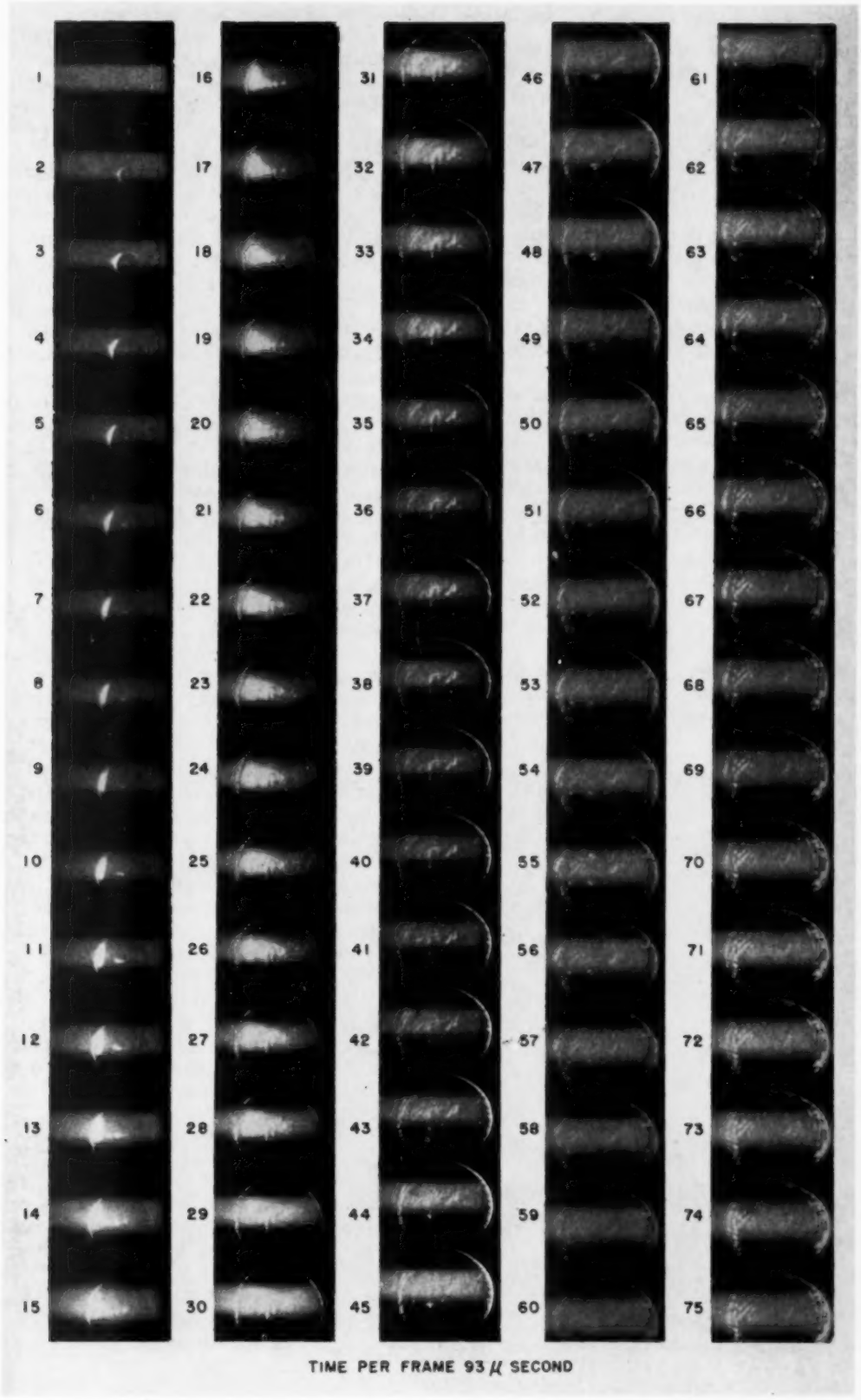

FIGURE 9. *Schlieren patterns of the collision of a drop of argon saturated water with a glass plate.*

2.4. Time Dependence of the Impact Force

It is of interest to know something about the order of time during which the impact force developed by the impingement of a freely falling waterdrop against a solid surface is effective. A preliminary attempt to measure this has recently been made by Lawrence Fleming of the Diamond Ordnance Fuze Laboratory, using a thin disk of barium titanate ceramic.

The barium titanate disk that was used was about 1 cm in diameter. It was coated with silver on both sides to make it conducting and was fastened with polystrene adhesive to a small metal base. The complete unit was then coated with polystyrene lacquer to prevent the water of the drop from short circuiting the silver layers. Leads from the silver layers were connected to a Dumont 304 oscilloscope.

The barium titanate unit was placed on a glass plate that was located below the exit of the tube through which the waterdrops were allowed to fall. The waterdrops struck the barium titanate disk after a free fall of approximately 40 ft. The traces that appeared on the oscilloscope screen as a result of the waterdrop collisions against the barium titanate were photographed directly. One of these traces with the time base marker is shown in figure 10. The time between cycles in the time base marker is 100 μsec.

It can be seen from the oscilloscope trace that the impact force is applied very suddenly. The movement of the point of light on the oscilloscope screen due to the increasing force was too rapid to leave a trace in the photograph. The decay curve only is visible. The force undergoes a rapid decay to zero in approximately the space of 1 msec. As has been noted in section 2.3, d, this is also approximately the time during which the head of water of the drop just vanishes.

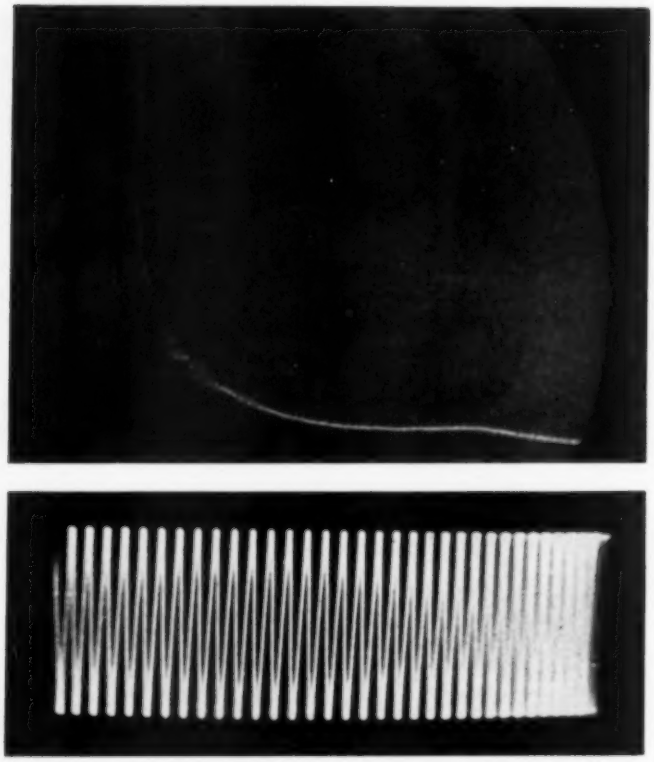

FIGURE 10. *Oscilloscope trace of the decay of the force produced by a waterdrop collision.*

2.5. Time Dependence of the Flow Velocity

The experimental values of radius of flow at regular intervals of time for the spread of a drop of water after impact at its terminal velocity in air against a glass plate are shown graphically in figure 11. The data for this graph, which are given in table 1, were secured from 50 consecutive pictures of the history of the collision of a waterdrop against a glass plate. The pictures were the first 50 frames of figure 7. The measurements of the diameter of the radial flow were made under low magnification with dividers and a steel rule graduated to 0.01 in. Each experimental diameter is the average of two measurements. The values plotted on the graph have been multiplied by a magnifying factor of 2.7. The magnifying factor was determined from a series of measurements of the diameter of the maximum spread of drops that were obtained from the same pipet and that fell approximately the same distance. The maximum radius of flow found in this way was 2.3 cm. The maximum radius of flow in the schlieren photographs occurred at frame 44 and was 0.85 cm. The quotient of these values of the maximum spread radius produced the magnifying factor.

Ambiguity exists as to the exact time at which the flow was initiated. Any radius of flow that is less than the radius of the drop itself is obscured by the drop. Extrapolation of the curve indicates that flow began not at time equal to zero on the graph but at a time equal to approximately 152 μsec. That is, the origin of the curve is translated 152 μsec along the abscissa because, of necessity, the radius of flow is zero at zero time, which is taken to be the first point of impact.

The slope of the curve of radius against time is the velocity of the radial flow. This curve is also shown in figure 11. The observed points are those obtained directly from the radius-against-time curve. The velocities are plotted in terms of the terminal

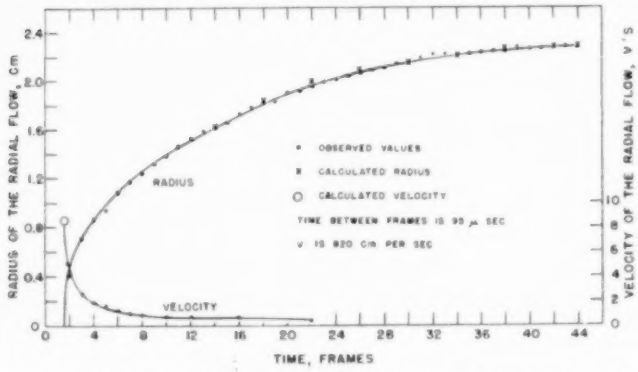

FIGURE 11. *Time dependence of the radius of flow and of the flow velocity of an impinging waterdrop.*

TABLE 1. *Values of the radius of flow for the waterdrop collision shown in figure 7*

Frame	Time	Experimental measured radius	Magnifying factor	Experimental real radius	Calculated real radius
	sec	*cm*		*cm*	*cm*
1	0	0.15$_2$	2.7	0.41$_2$	.....
2	.00003$_8$	.15$_7$	2.7	.41$_2$	.....
3	.00013$_4$	.26$_7$	2.7	.72$_0$	.....
4	.00022$_8$	.32$_1$	2.7	.87$_1$	.....
5	.00032$_1$	.35$_0$	2.7	.94$_6$	.....
6	.00041$_6$	0.40$_1$	2.7	1.08	.....
7	.00051$_1$	.43$_2$	2.7	1.1$_7$	.....
8	.00060$_8$	.45$_7$	2.7	1.2$_3$	.....
9	.00070$_3$	.49$_2$	2.7	1.3$_3$	.....
10	.00079$_8$	.51$_2$	2.7	1.3$_8$	.....
11	.00089$_3$	.54$_3$	2.7	1.4$_7$	.....
12	.00098$_8$	.56$_9$	2.7	1.5$_3$	.....
13	.0010$_8$	.58$_9$	2.7	1.5$_9$	.....
14	.0011$_8$	.59$_8$	2.7	1.6$_1$	1.6$_1$
15	.0012$_7$	.61$_7$	2.7	1.6$_7$	.....
16	.0013$_7$	.64$_3$	2.7	1.7$_4$	.....
17	.0014$_6$	.66$_5$	2.7	1.7$_9$	.....
18	.0015$_6$	.67$_3$	2.7	1.8$_2$	1.8$_4$
19	.0016$_5$	.67$_8$	2.7	1.8$_3$	.....
20	.0017$_5$	.70$_7$	2.7	1.9$_1$	.....
21	.0018$_4$	.71$_1$	2.7	1.9$_2$	.....
22	.0019$_4$	.72$_6$	2.7	1.9$_6$	1.9$_9$
23	.0020$_3$	.73$_9$	2.7	2.0$_0$	.....
24	.0021$_3$	.74$_8$	2.7	2.0$_2$	.....
25	.0022$_2$	.75$_7$	2.7	2.0$_4$	.....
26	.0023$_2$	.76$_1$	2.7	2.0$_5$	2.1$_0$
27	.0024$_1$	.77$_7$	2.7	2.1$_0$	.....
28	.0025$_1$	.78$_4$	2.7	2.1$_2$	.....
29	.0026$_0$	.79$_3$	2.7	2.1$_5$	.....
30	.0027$_0$	.80$_3$	2.7	2.1$_7$	2.1$_7$
31	.0027$_9$	.81$_3$	2.7	2.1$_9$	.....
32	.0028$_9$	.82$_0$	2.7	2.2$_1$	.....
33	.0029$_8$	.82$_0$	2.7	2.2$_1$	.....
34	.0030$_8$	.82$_0$	2.7	2.2$_2$	2.2$_2$
35	.0031$_7$	.82$_7$	2.7	2.2$_3$	.....
36	.0032$_7$	.82$_8$	2.7	2.2$_4$	.....
37	.0033$_6$	.83$_3$	2.7	2.2$_5$	.....
38	.0034$_6$	.83$_6$	2.7	2.2$_6$	2.2$_6$
39	.0035$_5$	.84$_6$	2.7	2.2$_8$	.....
40	.0036$_5$	.84$_1$	2.7	2.2$_7$	.....
41	.0037$_4$	.83$_8$	2.7	2.2$_6$	.....
42	.0038$_4$	.84$_6$	2.7	2.2$_9$	2.2$_9$
43	.0039$_3$	.84$_8$	2.7	2.2$_9$	.....
44	.0040$_3$	.85$_1$	2.7	2.3$_0$	2.3$_0$

velocity, V, of the waterdrop, which was approximately 26.9 ft/sec (820 cm/sec). Expressing the radial flow velocity in terms of velocity V that the drop had acquired at the instant at which it impinged against the glass plate makes it possible to see at a glance how much larger the radial flow velocity is than the impact velocity, for times just after the collision incident. It can also be seen at a glance that the radial flow velocity has dropped to the value of the impact velocity in less than 1 msec, that is, before the head of water that remains of the drop has disappeared into the radial flow. To express the values of the radial flow velocity in feet per second or in centimeters per second it is only necessary to multiply the values of the ordinate by 26.9 or by 820, respectively.

The central and side high lights for this waterdrop merged, that is, the head of water of the drop vanished, at the end of 1.2 msec. Furthermore, the oscilloscope trace of force as a function of time shown in figure 10 for a waterdrop, that was obtained from the same pipet and that fell through the same distance, indicates that the impact force vanished at the end of 1 msec. The velocity-against-time curve shown in figure 11 has the same shape as the oscilloscope trace of the force as a function of time shown in figure 10. This seems to indicate that the radial flow is propelled outward by the force of the impact. After the impact force vanishes the outward flow must continue, although at a much reduced velocity, under its own momentum.

2.6. Collisions of Waterdrops Against Surfaces Having Different Degrees of Resilience or Smoothness

That the flow characteristics of an impinging waterdrop depend strongly on the type of surface against which the collision occurs as well as on the velocity of the impact can be seen by comparing figures 2, 3, and 6. For the study of this effect the high-speed camera was placed at a slight angle above the surface against which the waterdrop would impinge. The camera was placed rather far from the area on the surface where the waterdrop was expected to hit in order to increase the probability of getting a picture of the collision incident. Unfortunately, this resulted in a loss of detail so that enlargements of a few frames from the film in the region where the collision occurred proved to be of little value. The films were therefore studied in motion, using a motion-picture projector.

a. Natural Rubber and GR–I Synthetic Rubber

Impingement of a waterdrop on a sheet of natural rubber about 80 mils thick and on a sheet of GR–I synthetic rubber of the same approximate thickness resulted in flow configurations of the same general appearance. Quite a bit of spray in upward motion was produced in the first stage of the impact. This spray moved out with the periphery of the radial flow of the waterdrop. See, for example, the comparable configuration that resulted in the case of waterdrop impingement against wet filter paper shown in figure 3. The upward splash was more nearly vertical in the case of waterdrop impingement against natural rubber than in the case of waterdrop impingement against the synthetic rubber. Natural rubber is much more resilient than GR–I rubber. A steel sphere dropped on a sheet of natural rubber undergoes a considerable rebound. The same steel sphere dropped on a sheet of GR–I synthetic rubber hardly rises from the surface. It is possible that the difference in resilience of the two rubbers may explain the more nearly vertical spray in the case of the natural rubber. On the other hand, it is possible that the depression formed in the natural rubber as a result of the impact of the waterdrop was deeper and that the spray was directed up the more nearly vertical sides of the depression to produce the configuration of spray that was observed. The Shore "A" hardness of the natural rubber was about 30, whereas that of the GR–I synthetic rubber was about 20. Although this static hardness measurement would seem to indicate that the greatest deformation should occur in the GR–I

synthetic rubber, it cannot be taken as a certain indication of what to expect under dynamic conditions of loading.

b. Dry Clean Glass

The collision and radial flow of a waterdrop on a dry clean glass plate was smooth. There was a slight spray formation around the head of water of the drop as it was driven into radial flow (see fig. 6). The glass plates that were used for this study contained scratch blemishes.

c. Iron Buffed and Iron as Received

One side of an iron plate was buffed, the other side was retained in the as-received condition. Comparison of the flow configurations that resulted from the impingement of a waterdrop on each of these iron surfaces showed marked differences. In the case of the buffed surface there was essentially no upward splash of the water as a result of the collision. There was only a slight disturbance around the vanishing head of water of the drop with a very smooth outward radial flow of the water. Impingement of a waterdrop on the iron plate in the as-received surface condition resulted in considerable upward splash of the water. The amount of spray that is formed as a result of a waterdrop-to-solid collision seems to be a function of the smoothness of the surface. The spray formation probably occurs at the time of maximum pressure.

d. Fine Sand in a Petri Dish

The collision of a waterdrop against fine moist sand in a petri dish appeared like an underground explosion of dynamite in diminutive. A crown of upward moving water splash and sand grains was produced by the impact. The print made in the sand by the collision consisted of a circular trench around a more or less undisturbed mound of sand in the center. The central mound of sand probably marked the stagnation point of the water flow from the drop. The circular trench was dug by the radial flow of the water. The configuration is quite interesting from the standpoint of how impinging waterdrops may dig pits in soft materials.

3. Equation for the Impact Pressure Resulting From Waterdrop-to-Solid Collisions

An early estimate of the mean pressure that results from the collision of a solid surface with a water sphere was made by Honegger [5]. In his treatment the velocity of the center of gravity is the impact velocity, V, when the time, t, is zero (at the first point of impact). The velocity of the center of gravity is $V/2$ at a time Δt later. He assumed that the center of gravity during the time Δt was displaced by the distance $d/4$, where d is the drop diameter. He then applied the impulse momentum equation in the form[2]

$$M\,V/2=Pf\Delta t, \tag{1}$$

where M is the mass of the drop, P is the pressure, and f is the mean contact area between the drop and the surface. He obtained in this way the equation for the pressure

$$P=4\times10^{-6}V^2, \tag{2}$$

where P is given in kilograms per square centimeter, if V is expressed in centimeters per second.

De Haller [6] has written as an estimate of the impact pressure when a solid surface strikes a cylinder of water from the side the equation for the collision of two flat elastic bars. This is

$$P=\frac{V\rho_1c_1}{1+(\rho_1c_1/\rho_2c_2)}, \tag{3}$$

where ρ_1 and ρ_2 are the density of the flat water bar and of the solid bar, respectively; c_1 and c_2 are the speed of sound in water and in the material of the solid bar, respectively; and V is the relative speed of the water bar with respect to the bar of solid material. This equation neglects the curvature of the water cylinder.

From the results of the experimental work, which have been discussed in section 2, it seems reasonable to think that a treatment similar to that of the elastic impact of solids may provide a reliable estimate of the impact pressure. However, the spherical shape of the waterdrop, which imposes the condition that compressional waves initiated in it by the collision are not all started simultaneously, must be taken into account.

Let the following assumptions be made:

(A) The first effect of the collision is the initiation of a compressional wave that starts to spread through the water sphere (see fig. 12). The water molecules of the spherical drop in the region traversed by the compressional wave attain a velocity in the direction in which the impinging solid surface is moving. This region of the drop consequently becomes slightly flattened. The velocity taken on by the water molecules in this region of the drop is dependent on the velocity of the impinging solid surface, but it is less than this velocity. Only a thin layer of water in direct contact with the impinging solid surface takes on a velocity that is identical with that of the solid

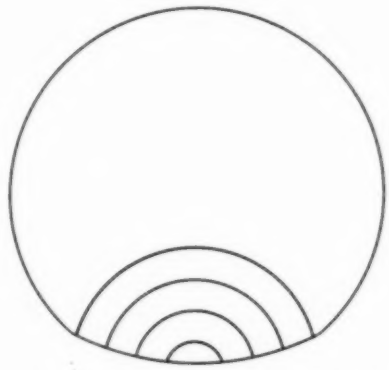

FIGURE 12. *Schematic drawing indicating that the water sphere is flattened as a result of compressional wavelets initiated in it.*

[2] The notation of other authors has been transcribed into the notation used in this paper.

surface. There is, furthermore, a velocity distribution among the water molecules in this region of the waterdrop. The following treatment is restricted to a consideration of the average velocity given to the water molecules in this region. Only the velocity in the direction in which the impinging solid surface is moving is considered.

(B) Maximum pressure, which is assumed to be reached at the end of the time interval Δt, is defined by the condition that the radiating compressional wavelet initiated at a point in the first instant of impact should just reinforce the compressional wavelet that is started at time Δt later in producing momentum in the water sphere (see fig. 13). That is, the rate of change of momentum of the water molecules in the region where this reinforcement occurs is greater than that of any other of the water molecules of the drop because it is produced by the combined effect of the wavelets.

(C) The second effect of the collision is that the first liquid of the drop that encounters the solid surface during the time interval Δt is displaced to form a thin cylinder under the drop (see fig. 14). The water of the shaded cap of the flattened drop of figure 14 is displaced into the ring the triangular cross section of which is bounded by the solid surface, the vertical boundary of the cylinder of water, and the curved boundary of the flattened waterdrop. The thin cylinder of water that forms and the region of the drop that is traversed by the compressional wave during the time interval Δt are stippled in figure 14. The thin cylinder of water is assumed to be in radial flow. The upper surface of it is termed the λ-plane. The head of water that remains of the drop (and which is separated from the surface of the impinging solid by the radially flowing thin cylinder of water) retains its shape except for a slight flattening (see figs. 2 and 3).

(D) As the collision continues, compressional wavelets are initiated at points of contact of the remaining water sphere with the λ-plane. In this sense the λ-plane, or upper boundary of the radial flow, may be considered as an effective striking surface.

Consider that the flat surface of a massive solid, moving with velocity V in the z-direction, is just at the point of collision with a stationary water sphere. If the first point of contact between the water sphere and the flat solid surface is made the origin of a rectangular coordinate system, the equation of the sphere at the origin of the coordinates is

$$x^2+y^2+(z-r')^2=r'^2 \tag{4}$$

where the x- and y-coordinates are in the plane of the colliding surface, and r' is the radius of the water sphere before the collision. For all points for which $y=0$, eq (4) reduces to the circle

$$x^2+(z-r')^2=r'^2 \tag{5}$$

in the xz-plane. The first point of collision between the solid surface and the water sphere is given by the equation for the circle of contact during the collision

$$x^2+y^2=[R'(z)]^2, \tag{6}$$

with $R'(z)$ equal to zero.

Consider that the first result of the collision is the initiation of a compressional wave that immediately begins to spread through the water sphere (see fig. 12 and assumption A). The water through which the compressional wave passes is given a velocity in the z-direction in which the surface of the massive solid was moving. As a result of this, the region of the water sphere that has been traversed by the compressional wave is slightly flattened in this direction. The radius of this flattened portion of the water sphere is r, and r is greater than r'.

The average velocity of the water in the region of the water sphere that has been traversed by the compressional wave may be written as αV, where α

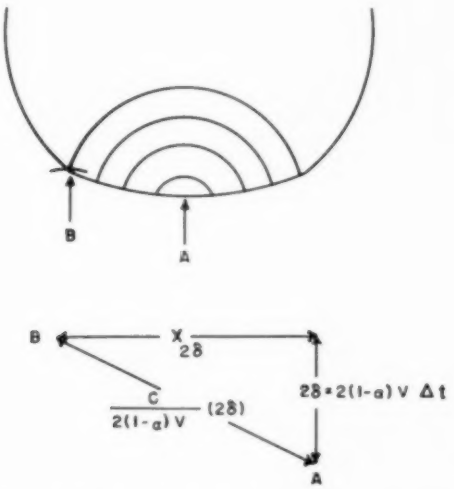

FIGURE 13. *Schematic drawing that illustrates the assumption made in regard to the maximum pressure.*

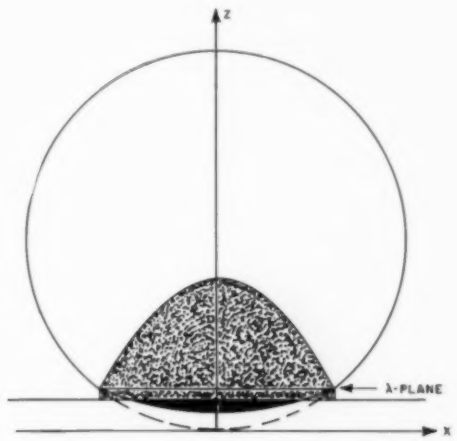

FIGURE 14. *Cross section of the water sphere that shows schematically the locus of the vertical components of the compressional wave and the formation of the thin cylinder of water that is in radial flow.*

is a coefficient that tells what fraction of velocity V is imparted to the water molecules on the average. As there is no marked attenuation of the amplitude of a compressional wave in water, the coefficient α must be governed mainly by the extent of divergence of the compressional wave as it spreads through the spherical drop. As the impact velocity increases for a series of waterdrop-to-solid collisions, the extent of flattening in the region of the drop that has been traversed by the compressional wave increases, the amount of divergence of the wave decreases, and the value of the coefficient α approaches unity.

Consider that the second result of the collision in the time interval Δt, during which the pressure reaches a maximum, is the displacement of the first water of the sphere that encountered the solid surface into a very thin cylinder of water that is in radial flow (see fig. 14 and assumption C). The average velocity at which this displacement occurs is $(1-\alpha)\,V$. It can readily be shown that in the limit the volume of a very thin slice cut off a sphere is one-half the volume of a cylinder that has the same height and base area. Consequently, in the time Δt in which the solid surface moving at the displacement velocity $(1-\alpha)V$ has moved a distance δ through the water sphere, where δ is the thickness of the cap of the flattened portion of the water sphere that is shaded in figure 14, the λ-plane has moved a distance 2δ. If the displacement velocity is constant, then the velocity $\overline{v}$ of the λ-plane is given by

$$\overline{v}=2(1-\alpha)V. \tag{7}$$

The massive striking surface is not at all slowed down as a result of the collision. It continues to move at the velocity V in the fixed coordinate system. In the fixed coordinate system, therefore, it has traveled the distance δ', where

$$\delta'=V\Delta t \tag{8}$$

through space in the time interval Δt. It has, however, only displaced the water of the drop which has been traversed by the compressional wave (and which is moving in the same direction that it is moving) the distance

$$\delta=(1-\alpha)V\Delta t. \tag{9}$$

Hence

$$\delta=(1-\alpha)\delta'. \tag{10}$$

It can, furthermore, be shown that the radius, r, of the flattened portion of the water sphere, through which the compressional wave has passed and in which the water has the average velocity αV in the z-direction, is given by

$$r=r'/(1-\alpha). \tag{11}$$

After the short time Δt the solid surface has moved a distance δ through that part of the water sphere that has been traversed by the compressional wave, the λ-plane has moved a distance 2δ, and the compressional wavelet that was started at the impact instant at point A of figure 13 has moved $c/\overline{v}$ times a far as the λ-plane has moved, that is, $2\delta c/\overline{v}$, and has reached point B. Here c is the speed of the compressional wave in water. The radius of the circle of contact that is given by eq (6) with $R'(z)$ replaced by $R(z)$ is now $x_{2\delta}$. This, on assumption B, is the point of maximum pressure because at this instant water molecules are being accelerated both by their own impact in the collision direction z and by the compressional wavelet that was started at the impact instant and that has just arrived in their locality.

It is possible to solve for δ, the thickness both of the shaded cap of water in figure 14 and of the disk of water in radial flow in the impact plane after the time Δt, in terms of the radius, r, of the flattened portion of the water sphere, the velocity of the striking surface, V, and the speed of the compressional wave, c. That is, using the right triangle shown in figure 13,

$$x^2_{2\delta}=\frac{4c^2\delta^2}{\overline{v}^2}-4\delta^2 \tag{12}$$

and from eq (5) with r' replaced by r,

$$x^2=r^2-(z-r)^2=2rz-z^2, \tag{13}$$

so that

$$x^2_{2\delta}=4r\delta-4\delta^2. \tag{14}$$

By subtracting eq (12) from eq (14), it is seen that

$$\delta=r\left[\frac{\overline{v}}{c}\right]^2. \tag{15}$$

According to assumption B, maximum pressure occurs after time Δt. It is noteworthy that this maximum of pressure has been defined by an arbitrary assumption and is not to be regarded as necessarily coincident with the maximum of total force in figure 10. Actually, since the time Δt as evaluated in section 4 for a collision of a waterdrop at its terminal velocity in air is 0.04 μsec, and since the time between cycles of the time base marker in figure 10 is 100 μsec, it is conceivable that it may exist at the left of this maximum. Furthermore, the maximum pressure as it is evaluated at the time Δt in the following treatment is not an instantaneous maximum pressure. To obtain it the total mass of water set in motion during the time interval Δt, and consequently all the force that has acted to produce water momentum over the time interval Δt, is considered. The instantaneous force that is acting at the last instant of this time interval is not considered.

The average rate of change of momentum of water in that portion of the drop that has been traversed by the compressional wave over the time interval Δt is $m\alpha V/\Delta t$, where m is the total mass of water in the drop that is set into motion as a result of the collision. If all of the force that has acted to produce water momentum over the time interval Δt, at the end of which the radius of the circle of contact between the drop and the surface is $x_{2\delta}$, is written as $\pi x_{2\delta}{}^2 P$, then

$$P=m\alpha V/[\pi x_{2\delta}{}^2\Delta t]. \tag{16}$$

It is necessary to evaluate the mass of water, m, that was set in motion in the z-direction as a result of the collision. After the time Δt, part of this total mass of water, the mass m', is moving in horizontal flow in the impact plane as a result of the impact pressure. The mass moving horizontally is given by

$$m'=\frac{1}{2}\,x^2_{2\delta}\pi\rho(2\delta)=x^2_{2\delta}\pi\rho\delta \tag{17}$$

because in the limit, as has already been noted, a slice of thickness 2δ and radius $x_{2\delta}$ cut off a sphere is just one-half the volume of a cylinder of the same height and base radius. Although the mass of water, m', is moving horizontally after the time Δt, it was given a velocity in the collision direction z during this time interval because it was traversed by the compressional wave.

There is also the mass of water m'' in the head of water remaining of the drop that has a velocity in the z-direction because it has been traversed by the compressional wave. After the time Δt the λ-plane has moved distance 2δ, and the compressional wave has moved to the curved boundary of the stippled area of figure 14. It may be assumed that this volume of water has received the signal that collision has occurred. The lower boundary of this volume of water is the plane $z=2\delta$, where the flattened sphere is at the origin of the coordinates. From eq (5) the z-coordinate of the points on the circle of radius r from which wavelets of compression originated is

$$z=r-(r^2-x^2)^{1/2}. \tag{18}$$

Δz is the distance the λ-plane moved up since the time that a compressional wavelet was started at the corresponding value of x. Then

$$\Delta z=2\delta-r+(r^2-x^2)^{1/2}. \tag{19}$$

Let z' be the distance traveled above the plane $z=2\delta$ by the compressional wavelet. Then

$$z'=\left[\frac{c}{2(1-\alpha)V}-1\right]\Delta z=\left[\frac{c}{\overline{v}}-1\right]\Delta z. \tag{20}$$

The locus of the points z' gives the envelope of the components of the compressional wavelets in the collision direction z. Substituting the value of Δz from eq (19) into eq (20),

$$z'=\left[\frac{c}{\overline{v}}-1\right][2\delta-r+(r^2-x^2)^{1/2}]. \tag{21}$$

Rearranging,

$$\left[\frac{\overline{v}}{c-\overline{v}}\right]z'-2\delta+r=(r^2-x^2)^{1/2}. \tag{22}$$

Letting

$$\frac{\overline{v}}{c-\overline{v}}=1/\beta \tag{23}$$

and squaring both sides of the equation

$$x^2=-\left[\frac{z'}{\beta}\right]^2+\frac{4\delta z'}{\beta}-\frac{2rz'}{\beta}-4\delta^2+4\delta r. \tag{24}$$

Equation (24) is an expression for x^2 in terms of z'; the enclosed volume of water, on substituting this value of x^2, is

$$\pi\int_{z'=0}^{z'=\beta(2\delta)}x^2dz'=\beta\pi\left[-\frac{8}{3}\,\delta^3+4\delta^2r\right]. \tag{25}$$

The limit of the ratio of this volume over the volume of a cylinder of the same height and base area is also found to be one-half. Consequently, the mass of water m'' having the average velocity αV in the collision direction z after the time Δt is

$$m''=\frac{\rho\pi\beta}{2}\,x^2_{2\delta}(2\delta)=\rho\pi\beta x^2_{2\delta}\delta, \tag{26}$$

and the total mass of water that was set into motion in the z-direction through having been traversed by the compressional wave is from eq (17) and (26)

$$m=m'+m''=(1+\beta)\,x^2_{2\delta}\pi\rho\delta. \tag{27}$$

The pressure, P, is then from eq (16)

$$P=\frac{[(1+\beta)\,x^2_{2\delta}\,\pi\rho\delta]\,\alpha V}{x^2_{2\delta}\,\pi\Delta t}. \tag{28}$$

Since

$$2\delta=2(1-\alpha)V\Delta t=\overline{v}\Delta t \tag{29}$$

and since

$$\beta=\left[\frac{c-\overline{v}}{\overline{v}}\right]$$

so that $(1+\beta)=c/\overline{v}$,

$$P=\frac{\alpha}{2}\,[c\rho V]. \tag{30}$$

This is the well-known water-hammer equation multiplied by the factor $\alpha/2$, which comes from the spherical shape of the waterdrop. It is noteworthy that the result that the pressure is some multiple of the water hammer pressure because of the spherical shape of the waterdrop could have been written down at once. There would, however, be no rational basis for guessing at the value of the multiple. The value of the coefficient α can be found empirically for waterdrop-to-solid collisions that can be stopped by high-speed motion pictures as is shown in section 4. For collisions at very high impact velocities, the coefficient α is probably close to unity. Consequently, for these collisions a reliable estimate of the impact pressure can also be made from eq (30).

Equation (30) has been verified indirectly by de Haller [6], who has measured the impact pressure between a flat surface and a jet of water struck from the side, using a piezoelectric pressure gage having a piston diameter of 1.5 mm. With his experi-

mental arrangement he was really measuring the pressure under short water cylinders struck from the side. Since the side of a cylinder contains both the element of circle of a sphere and the element of straight line of a plane, the pressure under such water shapes should be greater than that given by eq (30) but less than that given by eq (3), which is the equation de Haller was using for the impact pressure. With his piezoelectric pressure gage de Haller found the highest pressure value for a velocity of 35 m/sec to be 310 kg/cm^2. For this velocity eq (3) would predict a pressure of 490 kg/cm^2 if one assumes that the denominator on the right-hand side is essentially unity, that the speed of sound in water is 5,000 ft/sec, and that V is αV, where α is about 0.9. Equation (30) would predict a pressure of 245 kg/cm^2, assuming again that α is about 0.9. The pressure that is developed when a flat solid surface strikes a cylindrical water surface should be between that which is developed when it strikes a flat water surface and that which results when it strikes a spherical water surface. De Haller's experimental measurement shows that this is essentially the case.

4. Equation for the Flow Velocity at Maximum Pressure

Experimental measurements of the radius of flow of a waterdrop at regular intervals of time after collision at its terminal velocity in air with a glass surface were discussed in section 2.5. Figure 11 contains the curve of radial flow velocity against time. The data from which this curve was plotted are given in table 1. With eq (30) of section 3 the radial flow velocity at the time of maximum pressure can be calculated.

Assume that the radial flow from an impinging waterdrop has axial symmetry and that the effect of viscosity may be neglected. Because the pressure at the periphery of the radial flow is atmospheric and may be taken as zero, and because the center of the flowing disk is a stagnation point, the equation of flow in cylindrical coordinates is

$$P=\frac{\rho}{2}\int_0^{v_0} v\,dv+\rho\int_0^{r_0}\frac{\partial r}{\partial t}\,dr, \tag{31}$$

where P is the pressure at the center of the disk, ρ is the density of the liquid, v_0 is the observed velocity of spread, and r_0 is the observed radius of spread. It may be assumed that at the instant of maximum pressure $\partial r/\partial t$ is zero. Integration and substitution of the expression for P given by eq (30) then yields

$$v_0=[\alpha c V]^{1/2}. \tag{32}$$

The value of α can be calculated from the velocity at which the glass surface moved through the waterdrop. This velocity is $(1-\alpha)V$. The central and side high lights on the waterdrop for the collision incident shown in figure 7 merged in frame 14, which was 0.0011$_8$ sec from the point of impact or time zero. As the average waterdrop from the pipet that was used is 0.57 cm in diameter, the velocity at which the glass moved through the waterdrop was 484 cm/sec. The terminal velocity for a large waterdrop [4] is about 26.9 ft/sec (820 cm/sec). Hence,

$$(1-\alpha)820=484,$$

$$\alpha=0.4.$$

From eq (32), assuming that c is about 5,000 ft/sec, V about 26.9 ft/sec, and using the value of 0.4 for α, the radial flow velocity for this waterdrop at the time of maximum pressure was 232 ft/sec, or 8.6V. In order to plot this point on the velocity-against-time curve shown in figure 11 it is necessary to know the time at which maximum pressure existed, that is, Δt must also be evaluated. From eq (9),

$$\delta=(1-\alpha)V\Delta t.$$

From eq (7) and (15)

$$\delta=4r(1-\alpha)^2[V/c]^2.$$

From eq (7), (9), and (15)

$$\Delta t=4r(1-\alpha)V/c^2. \tag{33}$$

The radius r' of the waterdrop was about 0.29 cm, so that the radius of the flattened waterdrop from eq (11) was about 0.5 cm. Using the value of 0.4 for α, $\Delta t=0.04$ μsec. The calculated velocity is plotted on the velocity-against-time curve shown in figure 11 and is enclosed in a circle to distinguish it from the measured values.

The radial flow of the waterdrop is a direct consequence of the impact force. This force goes to zero in about 1 msec as is apparent from figure 16. The head of water of the drop also goes to zero in approximately this same time interval, and the radial flow velocity drops from 8.6 times the value of the impact velocity, V, to less than V. After this, the water in radial flow continues to move outward under its own momentum until the flow is completely checked by its internal resistance and by surface tension.

5. Equation for the Time Dependence of the Flow Radius

The observed values of the radius of flow at regular intervals of time for the spread of a drop of water after collision at its terminal velocity in air against a glass plate are shown graphically in figure 11. It is possible to calculate the radius of flow.

At the instant at which it just collides with the glass plate, the energy of the falling waterdrop consists of its kinetic energy and its potential surface energy. As soon as it begins to spread on the glass, the kinetic energy begins to be transformed into potential energy of surface and into dissipated energy. As long as any part of the head of water remains, the

terms of the energy equation are (1) the energy (kinetic and potential) remaining in the head of water, (2) the potential energy of surface of the radial flow, (3) the kinetic energy of the radially flowing water, and (4) the dissipated energy. At any instant of time the sum of these energy terms must be equal to the total energy of the falling drop at the instant of its collision with the glass plate.

The first of these energy terms would be difficult to evaluate. However, for all times after the head of water has vanished, that is, for all times during which the radial flow is moving outward under its own momentum, this energy term is zero. This is the case that will be considered.

At any instant at which an observation is made, the potential energy of surface of the radial flow, PE, is given by

$$PE=(\gamma_a+\gamma_g)\pi r_0^2, \tag{34}$$

where γ_a is the surface tension of water against air, γ_g is the interfacial tension between water and glass, and r_0 is the observed value of the radius of spread.

To develop an expression for the kinetic energy it is necessary to make some assumption about the shape of the cross section of the radial flow. From the work of Worthington [1] it appears that the flow of a drop of milk is shallowest in the center and deepest at the periphery. Figure 15 (a) is an enlarged reproduction of one of the sketches given by Worthington. As a simple approximation to this shape the assumption has been made that the radial flow is an extremely flat cylinder except for an empty cone that extends through half the thickness of the cylinder. The assumed cross section of the flow is shown in figure 15 (b).

The kinetic energy, KE, at the instant when the radius is r_0 is given by

$$KE=\frac{\rho}{2}\int_0^{r_0}2\pi r' h dr' v^2, \tag{35}$$

where h and v are the thickness of the flow and the radial flow velocity, respectively, and ρ is the density of the water. As v is zero at the center of the flow, and v is v_0 at the periphery of the flow,

$$v=\frac{r}{r_0}v_0, \tag{36}$$

where

$$v_0=r_0/t. \tag{37}$$

Thickness goes from $h_0/2$ at the center of the flow to h_0 at the periphery, so that

$$h=\frac{r}{r_0}\frac{h_0}{2}+\frac{h_0}{2}. \tag{38}$$

In terms of the mass, M, of the drop,

$$h_0=6M/[5\pi\rho r_0^2], \tag{39}$$

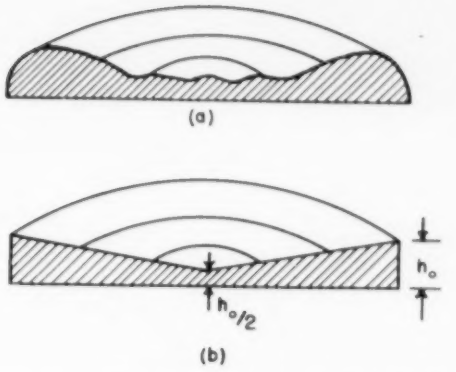

FIGURE 15. *Cross section of the flow of a liquid drop.*

(a) Cross section of the flow of a drop of milk as observed by Worthington; (b) assumed cross section of the flow of a drop of water.

since the volume of water is $\frac{5}{6}(\pi r_0^2 h_0)$. Substituting the expressions for v, h, and h_0 in the expression for the kinetic energy,

$$KE=\frac{54}{200}M\frac{r_0^2}{t^2}\sim\frac{M}{4}\frac{r_0^2}{t^2}. \tag{40}$$

At any instant of observation the dissipated energy, DE, is the accumulated dissipation during the time interval t. This dissipation is

$$DE=2\pi\int_0^t\int_0^{\Omega}\Phi d\Omega dt. \tag{41}$$

where Φ is the rate of dissipation of energy per unit time per unit volume, and Ω is the volume of the boundary layer attached to the solid. The thickness of this layer is σ, and σ is roughly less than h_0. Since in an axially symmetrical flow it suffices to consider only the variation of the radial flow velocity v with the flow thickness z, for this case

$$\Phi=\mu\left(\frac{\partial v}{\partial z}\right)^2, \tag{42}$$

where μ is the viscosity. Resorting to dimensional analysis and eq (41) and (42), it is seen that

$$DE=C\int_0^t\left(\frac{v_0}{\sigma}\right)^2 r_0^2\sigma dt, \tag{43}$$

where r_0 is the observed radius of flow and C is a constant containing the viscosity μ and having the dimensions of viscosity. It may be supposed that σ varies linearly with t, and, since v_0 is r_0/t,

$$DE=k\int_0^t\frac{r_0^4}{t^3}dt, \tag{44}$$

where k is a new constant.

The energy equation after the head of water remaining of the drop has vanished is

$$\pi(\gamma_a+\gamma_g)r_0^2+\frac{M}{4}\frac{r_0^2}{t^2}+k\int_0^t\frac{r_0^4}{t^3}dt=\frac{MV^2}{2}+4\pi r'^2\gamma_a, \tag{45}$$

where r' is the radius of the original drop, and V is the velocity at which the waterdrop strikes the surface. Differentiation with respect to time produces

$$2\pi(\gamma_a+\gamma_g)r_0\frac{dr_0}{dt}+\frac{M}{2}\frac{r_0}{t^2}\frac{dr_0}{dt}-\frac{M}{2}\frac{r_0^2}{t^3}+\frac{kr_0^4}{t^3}=0. \quad (46)$$

The solution of this equation is

$$\frac{r_0^2}{\frac{M}{2}-kr_0^2}=\frac{t^2}{\frac{M}{2}+2\pi(\gamma_a+\gamma_g)t^2}K, \quad (47)$$

where K is an integration constant. The expression for the integration constant is found from the condition that when $r_0=r_{max}$, $t=t_{max}$, where r_{max} indicates the maximum spread of the drop and t_{max} the corresponding time. Substituting the expression for the integration constant in eq (47), the equation for r_0 in terms of the time and constants is

$$r_0^2=\frac{t^2\left(\frac{M}{2}-kr_0^2\right)}{\frac{M}{2}+2\pi(\gamma_a+\gamma_g)t^2}\left[\frac{r_{max}^2\left\{\frac{M}{2}+2\pi(\gamma_a+\gamma_g)t_{max}^2\right\}}{t_{max}^2\left\{\frac{M}{2}-kr_{max}^2\right\}}\right]. \quad (48)$$

The equation is valid for all times after the head of water of the drop has vanished until the maximum spread is reached. It is necessary to evaluate the constant k from the data. For the collision incident shown in figure 7 the central and side high lights on the waterdrop merge, that is, the head of water remaining of the drop has vanished at frame 14. At frame 14, $r_0=1.6_1$ cm, $t=0.0011_8$ sec. The mass M of an average drop from the pipet that was used is 0.0989 g. The maximum spread was reached at frame 44, where $r_0=r_{max}=2.3_0$ cm and $t=t_{max}=0.0040_1$ sec. At present there is no way of measuring directly the interfacial tension between water and glass experimentally, and the value of $2\pi(\gamma_a+\gamma_g)$ can only be estimated roughly. Measurements of the surface tension of liquid glass against air have been made. Morey [7] lists the following values for a commercial soda-lime-silica glass: 404.3 d/cm at 1,225° C, 406.2 d/cm at 1,125° C, and 407.8 d/cm at 1,025° C. From these data it appears that the value may be about 420 d/cm at room temperature. It is impossible to know and hence to take into account any change that may be associated with the increased rigidity of the glass on cooling. Antonow's rule states [8] that for two liquids that are mutually saturated with each other, the interfacial tension is equal to the difference between the surface tensions of the two liquids separately. To this degree of approximation, $2\pi(\gamma_a+\gamma_g)\sim 2{,}638$ d/cm. This method of approximating the value of $(\gamma_a+\gamma_g)$ was suggested by William W. Walton of NBS Surface Chemistry Section.

To evaluate k, eq (48) was put in the form

$$\frac{\frac{M}{2r_{max}^2}-k}{\frac{M}{2r_0^2}-k}=\frac{\frac{M}{2t_{max}^2}+2\pi(\gamma_a+\gamma_g)}{\frac{M}{2t^2}+2\pi(\gamma_a+\gamma_g)}. \quad (49)$$

Substitution of the values of M, r_{max}, r_0 at frame 14, t_{max}, t at frame 14, and $2\pi(\gamma_a+\gamma_g)$ produced the result, $k=0.0076_7$ cgs units.

The values of r_0 calculated by use of eq (48) are listed in table 1 with the measured values. The measured values have been multiplied by a magnifying factor. The method of determining this factor is discussed in section 2.5. The calculated values are in almost perfect agreement with the empirical values, which appears to justify, a posteriori, the assumptions that were made. The calculated values of r_0 are indicated with crosses in figure 11.

In addition to specific acknowledgments that have been made in the text, the author thanks J. H. McMillan of the National Science Foundation, V. G. Szebehely of the David Taylor Model Basin, and George Irwin of the Naval Research Laboratory for conversations in which valuable suggestions were made.

The work described in this paper was sponsored by the Wright Air Development Center and was taken from reports submitted to them. Their assistance and interest are gratefully acknowledged.

6. References

[1] A. M. Worthington, On the forms assumed by drops of liquids falling vertically on a horizontal plate, Proc. Roy. Soc. **25**, 261 (1877); **25**, 498 (1877).
[2] A. M. Worthington, A study of splashes (Longmans, Green, and Co., New York, N. Y., 1908).
[3] R. T. Knapp and A. Hollander, Laboratory investigations of the mechanism of cavitation, Trans. ASME **70**, 419 (1948).
[4] D. C. Blanchard, General Electric Research Laboratory Occasional Report No. 7, Project Cirrus (November 1948).
[5] E. Honegger, Tests on erosion caused by jets, Brown Boveri Rev. **14**, 95 (1927).
[6] P. de Haller, Untersuchungen über die durch Kavitation hervorgerufenen Korrosionen, Schweiz. Bauztg. **101**, 243 (1933); **101**, 260 (1933).
[7] George W. Morey, Properties of glass, p. 201 (Reinhold Publishing Corp., New York, N. Y., 1945).
[8] N. K. Adam, Physics and chemistry of surfaces, p. 215 (Oxford University Press, London, 1941).

Washington, September 30, 1954.

Journal of Research of the National Bureau of Standards Vol. 54, No. 5, May 1955 Research Paper 2592

Effect of Darling-Dennison and Fermi Resonance on Thermodynamic Functions

Harold W. Woolley

The effect on thermodynamic functions due to resonance of the Darling-Dennison type for water and of the Fermi type for carbon dioxide is calculated working directly with the elements of the secular determinants that define the energy levels.

1. Introduction

In calculating thermodynamic functions for various molecular systems, the complication is sometimes encountered that the energy levels are expressed indirectly by means of a determinantal equation. In many cases, the determinant will have nonzero elements only along and quite near to the principal diagonal. Frequently, no explicit general solution for the positions of the levels as affected by the off-diagonal elements may be known, so that an explicit determination of the related thermodynamic properties as influenced by the effect in question would seem difficult at best. In some of these cases, useful results can be obtained in a general form from the secular equation without making use of explicit individual solutions.

2. Secular Determinant Method

If the secular determinant, $|E_{ij}-\delta_{ij}W|$, is expanded in polynomial form, beginning with the highest power of the unknown, W, then the successive coefficients for the different powers of W give the sum of roots and sums of products of the roots, such as $\sum_i W_i$, $\sum\sum_{i<j} W_iW_j$, $\sum\sum\sum_{i<j<k} W_iW_jW_k$, etc., when allowance is made for alteration of signs in the successive terms.

In the calculation of thermodynamic functions, the intermediate step of obtaining partition functions involves the evaluation and addition of a large number of Boltzmann factors, using the energies of the various levels. This factor, $e^{-W_i/kT}$, is expressible as a series so that the summation over a set of energy levels

$$\sum_i e^{-W_i/kT}=\sum_{m=0}\frac{(-kT)^{-m}}{m!}\sum_i W_i^m \tag{1}$$

may be found if the individual sums of powers of energy ΣW_i, ΣW_i^2, ΣW_i^3, etc., are known. It is possible to find these quantities in terms of sums of products of the roots and hence in terms of the coefficients of the polynomial expansion of the secular determinant. In this process several algebraic steps are involved including the application of the multinomial theorem. The result can thus be put in the form

$$\sum_i W_i^2=(\sum_i W_i)^2-2\sum\sum_{i<j} W_iW_j \tag{2}$$

$$\sum_i W_i^3=(\sum_i W_i)^3-3(\sum_i W_i)(\sum\sum_{j<k} W_jW_k)+3\sum\sum\sum_{i<j<k} W_iW_jW_k \tag{3}$$

$$\begin{aligned}\sum_i W_i^4=(\sum_i W_i)^4-4(\sum_i W_i)^2(\sum\sum_{j<k} W_jW_k)+4(\sum_i W_i)(\sum\sum\sum_{j<k<l} W_jW_kW_l)\\ +2(\sum\sum_{i<j} W_iW_j)^2-4\sum\sum\sum\sum_{i<j<k<l} W_iW_jW_kW_l\end{aligned} \tag{4}$$

$$\begin{aligned}\sum_i W_i^5=(\sum_i W_i)^5-5(\sum_i W_i)^3(\sum\sum_{j<k} W_jW_k)+5(\sum_i W_i)^2(\sum\sum\sum_{j<k<l} W_jW_kW_l)\\ +5(\sum_i W_i)(\sum\sum_{j<k} W_jW_k)^2-5(\sum_i W_i)(\sum\sum\sum\sum_{j<k<l<m} W_jW_kW_lW_m)\\ -5(\sum\sum_{i<j} W_iW_j)(\sum\sum\sum_{k<l<m} W_kW_lW_m)+5\sum\sum\sum\sum\sum_{i<j<k<l<m} W_iW_jW_kW_lW_m\end{aligned} \tag{5}$$

337361—55——4

$$\sum W_i^6=(\sum_i W_i)^6-6(\sum_i W_i)^4(\sum_{j<k}\sum W_jW_k)+6(\sum_i W_i)^2(\sum_{j<k<l}\sum\sum W_jW_kW_l)$$
$$+9(\sum_i W_i)^2(\sum_{j<k}\sum W_jW_k)^2-6(\sum_i W_i)^2(\sum_{j<k<l<m}\sum\sum\sum W_jW_kW_lW_m)$$
$$-12(\sum_i W_i)(\sum_{j<k}\sum W_jW_k)(\sum_{l<m<n}\sum\sum W_lW_mW_n)$$
$$+6(\sum_i W_i)(\sum_{j<k<l<m<n}\sum\sum\sum\sum W_jW_kW_lW_mW_n)$$
$$-2(\sum_{i<j}\sum W_iW_j)^3+6(\sum_{i<j}\sum W_iW_j)(\sum_{k<l<m<n}\sum\sum\sum W_kW_lW_mW_n)$$
$$+3(\sum_{i<j<k}\sum\sum W_iW_jW_k)^2-6\sum_{i<j<k<l<m<n}\sum\sum\sum\sum\sum\sum W_iW_jW_kW_lW_mW_n). \quad (6)$$

These coefficients for the various terms of the polynomial expansion, $\sum_{i<j}\sum W_iW_j$, $\sum_{i<j<k}\sum\sum W_iW_jW_k$, etc., can be obtained in the case of a specific secular determinant and introduced into eq (2) to (6). If the secular equation

$$|E_{ij}-\delta_{ij}W|=0 \quad (7)$$

involves a determinant of the nth order with nonzero elements along the principal diagonal and along diagonals immediately adjacent to it, then it is possible to represent the coefficients explicitly and introduce them into eq (2) to (6) so as to represent the quantities ΣW_i^m directly in terms of the elements of the determinant. Thus for the symmetric determinant with $E_{ii}=k_i$, $E_{i,i+1}=E_{i+1,i}=a_i$, $E_{i,i+2}=E_{i+2,i}=b_i$, $E_{i,i+3}=E_{i+3,i}=c_i$, and with all other elements equal to zero, one may with considerable algebra transform from the previous equations to the following:

$$\sum_i W_i=\sum_i k_i \quad (8)$$

$$\sum_i W_i^2=\sum_{i=1}^{n}k_i^2+2\sum_{i=1}^{n-1}a_i^2+2\sum_{i=1}^{n-2}b_i^2+2\sum_{i=1}^{n-3}c_i^2 \quad (9)$$

$$\sum_i W_i^3=\sum_{i=1}^{n}k_i^3+3\sum_{i=1}^{n-1}a_i^2(k_i+k_{i+1})+3\sum_{i=1}^{n-2}b_i^2(k_i+k_{i+2})+3\sum_{i=1}^{n-3}c_i^2(k_i+k_{i+3})$$
$$+6\sum_{i=1}^{n-2}a_ia_{i+1}b_i+6\sum_{i=1}^{n-3}a_ib_{i+1}c_i+6\sum_{i=1}^{n-3}a_{i+2}b_ic_i, \quad (10)$$

including terms involving a's, b's and c's. If the c's are zero, then

$$\sum_i W_i^4=\sum_{i=1}^{n}k_i^4+4\sum_{i=1}^{n-1}a_i^2(k_i^2+k_ik_{i+1}+k_{i+1}^2)+4\sum_{i=1}^{n-2}b_i^2(k_i^2+k_ik_{i+2}+k_{i+2}^2)$$
$$+8\sum_{i=1}^{n-2}a_ia_{i+1}b_i(k_i+k_{i+1}+k_{i+2})+2\sum_{i=1}^{n-1}a_i^4+2\sum_{i=1}^{n-2}b_i^4+4\sum_{i=1}^{n-2}a_i^2a_{i+1}^2+4\sum_{i=1}^{n-3}a_i^2b_{i+1}^2$$
$$+4\sum_{i=1}^{n-2}a_i^2b_i^2+4\sum_{i=1}^{n-2}a_{i+1}b_i^2+4\sum_{i=1}^{n-3}a_{i+2}^2b_i^2+8\sum_{i=1}^{n-3}a_ia_{i+2}b_ib_{i+1}+4\sum_{i=1}^{n-4}b_i^2b_{i+2}^2, \quad (11)$$

and if the b's also are zero

$$\sum_i W_i^5=\sum_1^n k_i^5+5\sum a_i^2(k_i^3+k_i^2k_{i+1}+k_ik_{i+1}^2+k_{i+1}^3)$$
$$+5\sum_1^{n-1}a_i^4(k_i+k_{i+1})+5\sum_1^{n-2}a_i^2a_{i+1}^2(k_i+2k_{i+1}+k_{i+2}) \quad (12)$$

and

$$\sum_i W_i^6 = \sum_1^n k_i^6 + 6\sum_1^{n-1} a_i^2(k_i^4 + k_i^3 k_{i+1} + k_i^2 k_{i+1}^2 + k_i k_{i+1}^3 + k_{i+1}^4) + 3\sum_1^{n-1} a_i^4(3k_i^2 + 4k_i k_{i+1} + 3k_{i+1}^2)$$

$$+ 6\sum_1^{n-2} a_i^2 a_{i+1}^2(k_i^2 + 2k_i k_{i+1} + k_i k_{i+2} + 3k_{i+1}^2 + 2k_{i+1}k_{i+2} + k_{i+2}^2)$$

$$+ 2\sum_1^{n-1} a_i^6 + 6\sum_1^{n-2} a_i^2 a_{i+1}^4 + 6\sum_1^{n-2} a_i^4 a_{i+1}^2 + 6\sum_1^{n-3} a_i^2 a_{i+1}^2 a_{i+2}^2. \tag{13}$$

Equations (8) to (13) may also be obtained by a matrix method with less effort. This is based on a theorem of Borchardt [1][1] and of Sylvester [2] which states that if A is a matrix then the characteristic roots of A^n are the nth powers of the characteristic roots of A. Then if H is the energy matrix, the sum of nth powers of roots W_i of the secular equation is given by the trace of the nth power of the matrix H:

$$\sum_i W_i^n = \text{trace } H^n. \tag{14}$$

so that eq (1) may also be written as

$$\sum_i e^{-W_i/kT} = \text{trace } e^{-H/kT} \tag{15}$$

and, in effect, include all the results of eq (8) to (13).

3. Application of the Method

Among cases in which molecular energy is given by a secular equation are resonances of the Darling-Dennison type and the Fermi type. In the case found by Darling and Dennison [3] for the H_2O molecule, occurring also in some other cases, the energy W is given by the secular equation

$$\begin{vmatrix} W_1^0 - W & W_{12} & 0 & 0 & \cdots \\ W_{21} & W_2^0 - W & W_{23} & 0 & \cdots \\ 0 & W_{32} & W_3^0 - W & W_{34} & \cdots \\ 0 & 0 & W_{43} & W_4^0 - W & \cdots \\ \cdots & \cdots & \cdots & \cdots & \cdots \end{vmatrix} = 0, \tag{16}$$

where the energies for the individual interacting levels would have been W_i° if the perturbation had been negligible. The magnitude of the perturbation is indicated by the off-diagonal terms

$$W_{i,i+1} = W_{i+1,i} = W^{v_1,v_2,v_3}_{v_1-2,v_2,v_3+2} = \tfrac{1}{2}\gamma\sqrt{v_1(v_1-1)(v_3+1)(v_3+2)}. \tag{17}$$

Any state indicated by v_1, v_2, v_3 with $v_1 > 1$ is perturbed appreciably by a state v_1-2, v_2, v_3+2, because of the approximate equality of ν_1 and ν_3. For higher quantum numbers, large groups of levels will be perturbing each other, and the secular equation will involve a secular determinant of correspondingly high order as indicated by eq (16). In the discussion which follows, the number of levels perturbing each other in a single group will be indicated by n, which will also be the order of the determinant. The mean value of the energy for the group of levels expressed as wave numbers will be indicated as G. The increment in the vibrational partition function due to the presence of the perturbation for a group of interacting levels is given by

$$\Delta Q = e^{-hcG/kT}\left[-\frac{hc}{kT}\Delta\sum_i W_i + \frac{1}{2}\left(\frac{hc}{kT}\right)^2 \Delta\sum_i W_i^2 - \frac{1}{6}\left(\frac{hc}{kT}\right)^3 \Delta\sum_i W_i^3 \ldots\right]. \tag{18}$$

[1] Figures in brackets indicate the literature references at the end of this paper.

According to the formulas derived and the definition of G, the various increments in the sums of powers of the energy W measured from the mean value G will be given by

$$\left.\begin{aligned}
&\Delta\sum_i W_i = 0 \\
&\Delta\sum_i W_i^2 = 2\sum_i W_{i,i+1}^2 \\
&\Delta\sum_i W_i^3 = 3\sum_i W_{i,i+1}^2 (W_i^\circ + W_{i+1}^\circ), \text{ etc.}
\end{aligned}\right\} \tag{19}$$

In the remainder of the treatment for this case of resonance, only the effect of $\Delta\sum_i W_i^\circ$ on the partition function and derived quantities will be considered. There is a basis for regarding higher order effects, as of $\Delta\sum_i W_i^3$, etc., as negligible. The levels which are involved in a given perturbing set have the same value of v_1+v_3 and are subject to the additional restriction that either v_1 or v_3 is only odd or only even within a single group. There are thus four cases to consider:

I. v_1 ranges from $2n-2$ to 0 while v_3 ranges from 0 to $2n-2$.
II. v_1 ranges from $2n-1$ to 1 while v_3 ranges from 0 to $2n-2$.
III. v_1 ranges from $2n-2$ to 0 while v_3 ranges from 1 to $2n-1$.
IV. v_1 ranges from $2n-1$ to 1 while v_3 ranges from 1 to $2n-1$.

These four cases give, respectively, for $W_{i,i+1}^2$

$$\text{I.} \quad W_{i,i+1}^2 = \frac{\gamma^2}{4}(2n-2i)(2n-2i-1)(2i-1)(2i) \tag{20}$$

$$\text{II.} \quad W_{i,i+1}^2 = \frac{\gamma^2}{4}(2n+1-2i)(2n-2i)(2i-1)(2i) \tag{21}$$

$$\text{III.} \quad W_{i,i+1}^2 = \frac{\gamma^2}{4}(2n-2i)(2n-2i-1)(2i)(2i+1) \tag{22}$$

$$\text{IV.} \quad W_{i,i+1}^2 = \frac{\gamma^2}{4}(2n+1-2i)(2n-2i)(2i)(2i+1), \tag{23}$$

where in each case i ranges from 1 to $n-1$. The evaluation $\sum_{i=1}^{n-1} W_{i,i+1}^2$ is quite straightforward and gives for these cases, respectively,

$$\frac{\gamma^2}{4}\cdot\frac{2n(n-1)(n+1)}{15}(4n^2-10n+9) \tag{24}$$

$$\frac{\gamma^2}{4}\cdot\frac{2n(n-1)(n+1)}{15}(2n-1)(2n+1) \tag{25}$$

$$\frac{\gamma^2}{4}\cdot\frac{2n(n-1)(n+1)}{15}(2n-1)(2n+1) \tag{26}$$

and

$$\frac{\gamma^2}{4}\cdot\frac{2n(n-1)(n+1)}{15}(4n^2+10n+9). \tag{27}$$

Considering the molecular vibrational energy as if it were due to harmonic oscillators having frequencies ω_1 and ω_3 wave numbers, for the two vibrations it is found that G, the average energy for the group of n levels is given in the various cases by

$$\text{I.} \quad G = (n-1)(\omega_1+\omega_3) \tag{28}$$

$$\text{II.} \quad G = n\omega_1 + (n-1)\omega_3 \tag{29}$$

III. $G=(n-1)\omega_1+n\omega_3$ (30)

IV. $G=n(\omega_1+\omega_2)$ (31)

The expressions are now at hand to permit the estimate of the relative increase in the partition function due to the perturbation. Continuing to treat the various cases separately, there are obtained for case I,

$$\left(\frac{\Delta Q}{Q}\right)_1=\frac{\sum_{n=2} e^{-\frac{hc}{kT}(\omega_1+\omega_3)(n-1)}\left(\frac{hc}{kT}\right)^2\frac{\gamma^2}{4}\frac{2n(n-1)(n+1)}{15}(4n^2-10n+9)}{\sum_{v_3=0}\sum_{v_1=0} e^{-\frac{hc}{kT}\omega_1 v_1} e^{-\frac{hc}{kT}\omega_3 v_3}}$$

$$=\gamma^2\left(\frac{hc}{kT}\right)^2\frac{\left(1-e^{-\frac{hc}{kT}\omega_1}\right)\left(1-e^{-\frac{hc}{kT}\omega_3}\right)}{\left[1-e^{-\frac{hc}{kT}(\omega_1+\omega_3)}\right]^6}\left[e^{-\frac{hc}{kT}(\omega_1+\omega_3)}+6e^{-2\frac{hc}{kT}(\omega_1+\omega_3)}+9e^{-3\frac{hc}{kT}(\omega_1+\omega_3)}\right], \quad (32)$$

for case II,

$$\left(\frac{\Delta Q}{Q}\right)_2=\frac{e^{\frac{hc}{kT}\omega_3}\sum_{n=2} e^{-\frac{hc}{kT}(\omega_1+\omega_3)n}\left(\frac{hc}{kT}\right)^2\frac{\gamma^2}{4}\frac{2n(n^2-1)(4n^2-1)}{15}}{\sum_{v_3=0}\sum_{v_1=0} e^{-\frac{hc}{kT}\omega_1 v_1} e^{-\frac{hc}{kT}\omega_3 v_3}}$$

$$=\gamma^2\left(\frac{hc}{kT}\right)^2\frac{\left(1-e^{-\frac{hc}{kT}\omega_1}\right)\left(1-e^{-\frac{hc}{kT}\omega_3}\right)e^{\frac{hc}{kT}\omega_3}}{\left[1-e^{-\frac{hc}{kT}(\omega_1+\omega_3)}\right]^6}\left[3e^{-2\frac{hc}{kT}(\omega_1+\omega_3)}+10e^{-3\frac{hc}{kT}(\omega_1+\omega_3)}+3e^{-4\frac{hc}{kT}(\omega_1+\omega_3)}\right], \quad (33)$$

for case III,

$$\left(\frac{\Delta Q}{Q}\right)_3=\frac{e^{-\frac{hc}{kT}\omega_1}\sum_{n=2} e^{-\frac{hc}{kT}(\omega_1+\omega_3)n}\left(\frac{hc}{kT}\right)^2\frac{\gamma_2^2}{4}\frac{2n(n^2-1)(4n^2-1)}{15}}{\sum_{v_3=0}\sum_{v_1=0} e^{-\frac{hc}{kT}\omega_1 v_1} e^{-\frac{hc}{kT}\omega_3 v_3}}$$

$$=\gamma^2\left(\frac{hc}{kT}\right)^2\frac{\left(1-e^{-\frac{hc}{kT}\omega_1}\right)\left(1-e^{-\frac{hc}{kT}\omega_3}\right)e^{-\frac{hc}{kT}\omega_1}}{\left[1-e^{-\frac{hc}{kT}(\omega_1+\omega_3)}\right]^6}\left[3e^{-2\frac{hc}{kT}(\omega_1+\omega_3)}+10e^{-3\frac{hc}{kT}(\omega_1+\omega_3)}+3e^{-4\frac{hc}{kT}(\omega_1+\omega_3)}\right], \quad (34)$$

and for case IV,

$$\left(\frac{\Delta Q}{Q}\right)_4=\frac{\sum_{n=2} e^{-\frac{hc}{kT}(\omega_1+\omega_3)n}\left(\frac{hc}{kT}\right)^2\frac{\gamma^2}{4}\frac{2n(n^2-1)}{15}(4n^2+10n+9)}{\sum_{v_3=0}\sum_{v_1=0} e^{-\frac{hc}{kT}\omega_1 v_1} e^{-\frac{hc}{kT}\omega_3 v_3}}$$

$$=\gamma^2\left(\frac{hc}{kT}\right)^2\frac{\left(1-e^{-\frac{hc}{kT}\omega_1}\right)\left(1-e^{-\frac{hc}{kT}\omega_3}\right)}{\left[1-e^{-\frac{hc}{kT}(\omega_1+\omega_3)}\right]^6}\left[9e^{-2\frac{hc}{kT}(\omega_1+\omega_3)}+6e^{-3\frac{hc}{kT}(\omega_1+\omega_3)}+e^{-4\frac{hc}{kT}(\omega_1+\omega_3)}\right]. \quad (35)$$

Then, in lowest order of approximation, the total effect of the perturbation is indicated by the sum of the separate $(\Delta Q/Q)_i$ for the four cases, to give as the approximate value of $\Delta \ln Q$

$$\Delta \ln Q = \sum_i (\Delta Q/Q)_i = \gamma^2 \left(\frac{hc}{kT}\right)^2 \frac{\left(1-e^{-\frac{hc}{kT}\omega_1}\right)\left(1-e^{-\frac{hc}{kT}\omega_3}\right)}{\left[1-e^{-\frac{hc}{kT}(\omega_1+\omega_3)}\right]^6} \Big[e^{-\frac{hc}{kT}(\omega_1+\omega_3)} + 15e^{-2\frac{hc}{kT}(\omega_1+\omega_3)} + 15e^{-3\frac{hc}{kT}(\omega_1+\omega_3)} + e^{-4\frac{hc}{kT}(\omega_1+\omega_3)} + \left(e^{-\frac{hc}{kT}\omega_1}+e^{-\frac{hc}{kT}\omega_3}\right)\left(3e^{-\frac{hc}{kT}(\omega_1+\omega_3)}+10e^{-2\frac{hc}{kT}(\omega_1+\omega_3)}+3e^{-3\frac{hc}{kT}(\omega_1+\omega_3)}\right)\Big]. \quad (36)$$

If the approximate equality of ω_1 and ω_3 is now taken into account, then letting $u = hc\omega/kT$ represent either $hc\omega_1/kT$ or $hc\omega_3/kT$ or their average value, it is found that

$$\Delta \ln Q = \frac{\gamma^2}{\omega^2} \frac{u^2(1-e^{-u})^2}{(1-e^{-2u})^6} [e^{-2u}+6e^{-3u}+15e^{-4u}+20e^{-5u}+15e^{-6u}+6e^{-7u}+e^{-8u}]$$

$$= \frac{\gamma^2}{\omega^2} \frac{u^2 e^{-2u}}{(1-e^{-u})^4}. \quad (37)$$

This is the approximate contribution to the Gibbs free-energy function, $-F^\circ/RT$, due to the effect of the perturbation. The corresponding contributions to H°/RT and C_p°/R are $-u\frac{d}{du}\Delta \ln Q$ and $u^2\frac{d^2}{du^2}\Delta \ln Q$, which give

$$\Delta(H^\circ/RT) = \frac{\gamma^2}{\omega^2} u^2 \frac{e^{-2u}}{(1-e^{-u})^4} \cdot 2 \left\{ u \frac{(1+e^{-u})}{(1-e^{-u})} - 1 \right\} \quad (38)$$

and

$$\Delta(C_p^\circ/R) = \frac{\gamma^2}{\omega^2} u^2 \frac{e^{-2u}}{(1-e^{-u})^4} \cdot 2 \left\{ 1 - 4u \frac{(1+e^{-u})}{(1-e^{-u})} + 2u^2 \frac{(1+3e^{-u}+e^{-2u})}{(1-e^{-u})^2} \right\}. \quad (39)$$

A value of γ of 77.52 cm^{-1} has recently been given by Benedict [4] with higher order constants and has been used in the present calculation. For the present case, ω may be taken as about 3,650 cm^{-1}. As should be expected, the total effect is found to be small. This is due largely to the fact that the lowest levels showing this type of resonance are at about 7,300 cm^{-1} so that a relatively high temperature is required before the levels in question are appreciably excited. The magnitude of the effect is indicated in table 1 for several temperatures.

One may inquire as to the approximate behavior of the effect in the limiting condition of high temperatures. If one neglects higher order effects in the manner of the foregoing derivation, which would neglect an appreciable relative effect due to anharmonicity, then when the functions are expanded in increasing powers of u, the leading term gives the approximate values

$$-\Delta F^\circ/RT \approx \frac{\gamma^2}{\omega^2 u^2}, \quad \Delta H^\circ/RT \approx 2\frac{\gamma^2}{\omega^2 u^2}, \text{ and } \Delta C_p^\circ/R = 6\frac{\gamma^2}{\omega^2 u^2} \quad (40)$$

or

TABLE 1. *Effect of Darling-Dennison resonance on thermodynamic functions for* H_2O

Temperature	$\Delta(-F^\circ/RT)$	$\Delta(H^\circ/RT)$	$\Delta C_p^\circ/R$
$^\circ K$			
1,000	2.6×10^{-7}	24×10^{-7}	206×10^{-7}
2,000	1.88×10^{-5}	7.81×10^{-5}	33.1×10^{-5}
3,000	0.784×10^{-4}	2.37×10^{-4}	8.01×10^{-4}
4,000	1.75×10^{-4}	4.52×10^{-4}	14.2×10^{-4}
5,000	3.03×10^{-4}	7.23×10^{-4}	22.1×10^{-4}

$$-\Delta F^\circ/RT \approx \frac{\gamma^2}{\omega^4}\left(\frac{kT}{hc}\right)^2, \quad \Delta H^\circ/RT \approx 2\frac{\gamma^2}{\omega^4}\left(\frac{kT}{hc}\right)^2 \quad \text{and} \quad \Delta C_p^\circ/R \approx 6\frac{\gamma^2}{\omega^4}\left(\frac{kT}{hc}\right)^2. \quad (41)$$

The quadratic power of temperature is a result of the fourth power dependence of $\Delta\Sigma W_i^2$ upon the quantum numbers, which supplies a fourth power of T as a factor in the summation. This is cut down to the second power by the inverse second power in the coefficient of this term.

Another case of resonating levels for which details have been worked out is that of Fermi resonance in the case of CO_2. While the effect of the perturbation upon the thermodynamic functions can be expected to be fairly small in this case also, since the perturbation, as in the previous case, involves the displacement of some levels upward and some downward in such a way as to nearly compensate, it is nevertheless a larger effect than in the case of H_2O, mainly because the energy of the lowest resonating levels is near 1330 cm^{-1} for CO_2 as compared with the 7,300 cm^{-1} for H_2O, so that comparable excitation takes place at a lower temperature.

It was shown by Dennison [5] and Adel and Dennison [6] that a satisfactory representation of the CO_2 spectrum could be obtained if account were taken of perturbations within groups of levels with equal values of l, the azimuthal quantum number, and with equal values of $2v_1+v_2$. Then the effect of the perturbation within a group of n levels of this kind is indicated by the shifts of roots of such a secular equation as (16) with corresponding effects on the thermodynamic functions indicated in terms of the partition function according to eq (18) and (19). In each group of n levels, the value of v_1 ranges from zero to $n-1$, with v_2 going from its maximum value to its minimum value which is equal to $|l|$. The number of levels interacting within one group is given by $n=\frac{1}{2}(V-|l|)-1$. The elements of the determinant which are adjacent to the main diagonal were presented by Dennison in a form which can be so converted as to indicate that

$$W^2_{i,\,i+1}=W_0^2 i(n-1)(V+2-n-i), \tag{42}$$

where i ranges from 1 to $n-1$. For the evaluation of the principal contribution to the partition function according to eq (18), there is needed a knowledge of the distribution of the unperturbed vibrational levels. It is assumed that these are given in the somewhat unconventional form

$$G_v=\sum\omega_i v_i+\sum X_{ii}v_i(v_i-1)+\sum X_{ij}v_iv_j. \tag{43}$$

Then the average value of G for a given group of levels is given by

$$\begin{aligned} G=\omega_2 V+\omega_3 v_3+\omega_n(n-1)+X_{22}(V^2-V)+X_{33}(v_3^2-v_3)+X_{nn}(n-1)^2 \\ +X_{23}Vv_3+X_{Vn}V(n-1)+X_{n3}(n-1)v_3, \end{aligned} \tag{44}$$

where

$$\left.\begin{aligned} \omega_n&=\frac{1}{2}\omega_1-\omega_2-\frac{1}{3}X_{11}+\frac{5}{3}X_{22}-\frac{1}{3}X_{12} \\ X_{nn}&=\frac{1}{3}X_{11}+\frac{4}{3}X_{22}-\frac{2}{3}X_{12} \\ X_{vn}&=\frac{1}{2}X_{12}-2X_{22} \\ X_{n3}&=\frac{1}{2}X_{13}-X_{23}. \end{aligned}\right\} \tag{45}$$

By simple summation,

$$\sum_{i=1}^{n-1} W^2_{i,\,i+1}=W_0^2\frac{n(n^2-1)}{2}\left[\frac{1}{3}(V+2)-\frac{1}{2}n\right] \tag{46}$$

and for the next term of (18)

$$\sum_{i=1}^{n-1} W^2_{i,\,i+1}(W^0_i+W^0_{i+1})=W_0^2\frac{n(n^2-1)(4-n^2)}{30}[\omega_n-\delta_n V-X_{n3}v_3], \tag{47}$$

where $\delta_v=\frac{1}{3}X_{11}-\frac{2}{3}X_{22}-\frac{1}{6}X_{12}$. After multiplying by the exponential Boltzmann factor for the average vibrational energy, the summation over V and n follow, but with the requirement that half values of the summand are to be used when V has its lowest value, $2(n-1)$, in order to take account of the absence of l degeneracy for $l=0$. The choice of doing this rather than multiplying by 2 for $l\neq 0$ comes about as the result of the fact that half of the rotational levels are absent due to the symmetry of the molecule and the zero nuclear spin for oxygen. Then this is compared with a total approximate Q similarly omitting any factor for l doubling. If the effects for anharmonicity are disregarded, the leading term is obtained as

$$\frac{\Delta Q}{Q}\approx\frac{1}{2}\left(\frac{hc}{kT}\right)^2\frac{W_0^{*2}e^{-\frac{2hc\omega_2}{kT}}\left(1-e^{-\frac{hc\omega_1}{kT}}\right)}{\left(1-e^{-\frac{2hc\omega_2}{kT}}\right)^2\left(1-e^{-\frac{hc\omega_2}{kT}}\right)^2}. \tag{48}$$

The effect of Fermi resonance, using $u=hc\omega_2/kT$ and disregarding the distinction between ω_1 and $2\omega_2$, is thus given approximately [7] by

$$\Delta(-F^\circ/RT)=\frac{1}{2}\frac{W_0^{*2}}{\omega_2^2}\frac{u^2e^{-2u}}{(1-e^{-2u})(1-e^{-u})^2}, \tag{49}$$

$$\Delta H^\circ/RT=\Delta(-F^\circ/RT)\cdot 2\left[u\left(1+\frac{e^{-u}}{1-e^{-u}}+\frac{e^{-2u}}{1-e^{-2u}}\right)-1\right], \tag{50}$$

and

$$C_p^v/R=\Delta(-F^\circ/RT)\cdot 2\left\{2\left[u\left(1+\frac{e^{-u}}{1-e^{-u}}+\frac{e^{-2u}}{1-e^{-2u}}\right)-1\right]^2-u^2\left[\frac{e^{-u}}{(1-e^{-u})^2}+\frac{2e^{-2u}}{(1-e^{-2u})^2}\right]-1\right\}. \tag{51}$$

The effect can be obtained in more detail by including an additional contribution from eq (46). Using $u_i=hc\omega_i/kT$ and using $\omega_1=2\omega_2$ after the first term, eq (48) is replaced by

$$\begin{aligned}
\Delta\ln Q=&\frac{1}{2}\left(\frac{hc}{kT}\right)^2\frac{W_0^{*2}e^{-2u_2}(1-e^{-u_1})}{(1-e^{-2u_2})^2(1-e^{-u_2})^2}\\
&-\left(\frac{hc}{kT}\right)^3W_0^{*2}\left\{\frac{\omega_n}{2(1-e^{-2u_2})^4}[e^{-2u_2}+2e^{-3u_2}+6e^{-4u_2}+6e^{-5u_2}+3e^{-6u_2}]\right.\\
&+\frac{X_{nn}}{2(1-e^{-2u_2})^5}[e^{-2u_2}+2e^{-3u_2}+17e^{-4u_2}+20e^{-5u_2}+33e^{-6u_2}+18e^{-7u_2}+9e^{-8u_2}]\\
&+\frac{X_{Vn}}{(1-e^{-2u_2})^5}[e^{-2u_2}+4e^{-3u_2}+19e^{-4u_2}+30e^{-5u_2}+39e^{-6u_2}+24e^{-7u_2}+9e^{-8u_2}]\\
&+\frac{X_{23}e^{-u_3}}{(1-e^{-u_3})(1-e^{-2u_2})^4}[e^{-2u_2}+4e^{-3u_2}+8e^{-4u_2}+8e^{-5u_2}+3e^{-6u_2}]\\
&+\frac{X_{n3}e^{-u_3}}{2(1-e^{-u_3})(1-e^{-2u_2})^4}[e^{-2u_2}+2e^{-3u_2}+6e^{-4u_2}+6e^{-5u_2}+3e^{-6u_2}]\\
&+\frac{X_{22}}{(1-e^{-2u_2})^5}[e^{-2u_2}+10e^{-3u_2}+43e^{-4u_2}+88e^{-5u_2}+103e^{-6u_2}+70e^{-7u_2}+21e^{-8u_2}]\\
&-\frac{B+g_{22}}{6(1-e^{-2u_2})^5}[e^{-3u_2}+8e^{-4u_2}+41e^{-5u_2}+104e^{-6u_2}+119e^{-7u_2}+92e^{-8u_2}+19e^{-9u_2}]\\
&-\frac{X_{11}e^{-6u_2}}{(1-e^{-2u_2})^3(1-e^{-u_2})^2}-\frac{3X_{22}e^{-4u_2}}{(1-e^{-2u_2})(1-e^{-u_2})^4}-\frac{X_{12}e^{-5u_2}}{(1-e^{-2u_2})^2(1-e^{-u_2})^3}\\
&\left.-\frac{X_{13}e^{-u_3}e^{-4u_2}}{2(1-e^{-u_3})(1-e^{-2u_2})^2(1-e^{-u_2})^2}-\frac{X_{23}e^{-u_3}e^{-3u_2}}{(1-e^{-u_3})(1-e^{-2u_2})(1-e^{-u_2})^3}\right\}.
\end{aligned} \tag{52}$$

A calculation was made for CO_2 using as values for the constants (in cm^{-1})

$$\omega_1=1342.86 \qquad \omega_2=666.27 \qquad \omega_3=2349.15$$

$$X_{11}=-2.20 \qquad X_{22}=-0.75 \qquad X_{33}=-12.46$$

$$X_{12}=3.76 \qquad X_{13}=-18.54 \qquad X_{23}=-12.48$$

with $B+g_{22}=1.42$ and $W_0=51.01\ cm^{-1}$, giving $\omega_n=3.39$, $X_{nn}=-4.24$, $X_{Vn}=3.38$, and $X_{n3}=3.21$. With these constants, the magnitude of the effect as given by eq (48) is indicated in table 2 as the first column under each heading while the combined effect consistent with eq (52) is shown as the second column under each of the headings, $\Delta(-F^\circ/RT)$, $\Delta(H^\circ/RT)$ and $\Delta C_p^\circ/R$. The entire effect for CO_2 is rather small and in many computations could be neglected. For elevated temperature, the leading term in this case is roughly linear in the absolute temperature rather than quadratic as was found to be the case for H_2O. This is due to the essentially cubic dependence of $W^2_{i,i+1}$ upon quantum numbers in the present case, as compared with the quartic dependence in the case of H_2O. It is also seen that this simple dependence upon temperature is modified greatly by the effect of anharmonicity. The large effect of anharmonicity at high temperature can be regarded as due to its lowering of entire groups of resonating levels with a resultant increased population in such groups, which provides an increase in thermodynamic effect.

This treatment does not make any adjustment for the effect of resonance on the compositions of states, since the rotational perturbation is quite small, and, in addition, the resonance shifts have compensating effects in first approximation as has been noted in deriving the larger contributions due to perturbation which have been taken into account. They would thus be quite negligible.

TABLE 2. *Effect of Fermi resonance on thermodynamic functions for* CO_2

Temperature	$\Delta(-F^\circ/RT)$		$\Delta(H^\circ/RT)$		$\Delta(C_p/R)$	
°K						
200	5×10^{-6}		36×10^{-6}		27×10^{-5}	
250	22×10^{-6}		12×10^{-5}		70×10^{-5}	
300	5×10^{-5}		26×10^{-5}		11×10^{-4}	
400	18×10^{-5}		56×10^{-5}		17×10^{-4}	
500	33×10^{-5}		85×10^{-5}		22×10^{-4}	
	eq(49)	eq(52)	eq(50)	eq(52)	eq(51)	eq(52)
1,000	0.0012	0.0012	0.0018	0.0018	0.0033	0.0035
2,000	.0029	.0030	.0033	.0036	.0062	.0073
3,000	.0045	.0048	.0048	.0056	.0093	.0119
4,000	.0061	.0067	.0063	.0078	.0124	.0173
5,000	.0077	.0087	.0078	.0103	.0155	.0233

Equations (49), (50), and (51) also represent approximately the effect of Fermi resonance in H_2O involving levels for which $2v_1+v_2$ is a constant, even though v_2 is not degenerate as for CO_2. Benedict [4] gives the matrix element $(v_1, v_2+2|v_1+1, v_2)=\frac{1}{2}\{200(v_1+1)(v_2+2)(v_2+1)\}^{\frac{1}{2}}$, indicating that $W_0^2=200\ cm^{-2}$. A few values for the Fermi resonance effect for H_2O are given in table 3. The effect is much smaller than the Darling-Dennison resonance effect at the higher

TABLE 3. *Effect of Fermi resonance on thermodynamic functions for* H_2O

Temperature	$\Delta(-F^\circ/RT)$	$\Delta(H^\circ/RT)$	$\Delta C_p^\circ/R$
°K			
500	8×10^{-8}	10^{-6}	4×10^{-6}
1,000	3×10^{-6}	8×10^{-6}	2×10^{-5}
2,000	10^{-5}	2×10^{-5}	4×10^{-5}
3,000	2×10^{-5}	3×10^{-5}	5×10^{-5}
4,000	3×10^{-5}	4×10^{-5}	7×10^{-5}
5,000	4×10^{-5}	4×10^{-5}	9×10^{-5}

temperatures although it is the larger at 1,000° K and below. Its earlier rise is partly due to the resonance occurring first near 3,400 cm^{-1} as compared with 7,300 cm^{-1} for the Darling-Dennison resonance. The magnitude of the resonance effects for H_2O and CO_2 are shown in figures 1 and 2, respectively.

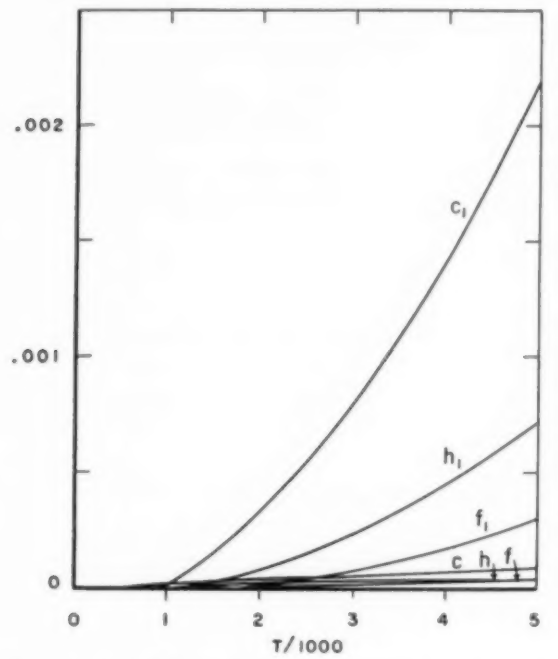

FIGURE 1. *Effect of resonance on thermodynamic functions for* H_2O.

c_1, h_1, f_1: Contribution of Darling-Dennison resonance to C_v/R, $(H^\circ - E_0^\circ)/RT$, and $-(F^\circ - E_0^\circ)/RT$. c, h, f: Contribution of Fermi resonance to C_v°/R, $(H^\circ - E^\circ)/RT$, and $-(F^\circ - E_0^\circ)/RT$.

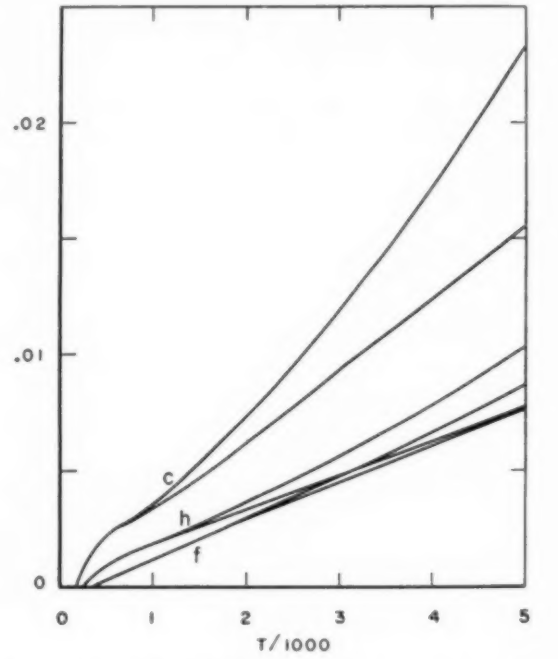

FIGURE 2. *Effect of Fermi resonance on thermodynamic functions for* CO_2.

c, h, f: Contributions to C_v/R, $(H^\circ - E_0^\circ)/RT$, and $-(F^\circ - E_0^\circ)/RT$. Upper branches with anharmonicity, lower branches neglecting anharmonicity.

4. Conclusion

A useful method of calculation of thermodynamic effects for levels defined by a secular determinant equation has been demonstrated.

Many other instances with similar perturbations are known and their effects on thermodynamic functions should be calculable by similar methods if the theoretical description of the perturbation has been worked out and the spectra fitted in the detail that has been achieved for H_2O and CO_2. In particular, C_2H_2 gives an example of Darling-Dennison resonance for which eq (37), (38), and (39) would apply. Other molecules with Fermi resonance similar to that for CO_2 to which eq (49), (50) and (51) apply include CS_2, C_2H_6, C_2D_6 and N_2O.

5. References

(1) C. W. Borchardt, J. Reine Angew. Math. **30**, 38 (1846); J. Math. Pures Appl. [I] **12**, 50 (1847).
(2) J. J. Sylvester, Nouv. Ann. math. **11**, 439 (1852).
(3) B. T. Darling and D. M. Dennison, Phys. Rev. **57**, 128 (1940).
(4) W. S. Benedict, unpublished data.
(5) D. M. Dennison, Phys. Rev. **41**, 304 (1932).
(6) A. Adel and D. M. Dennison, Phys. Rev. **43**, 716 (1933).
(7) Harold W. Woolley, The effect of Fermi resonance on the thermodynamic functions of gaseous CO_2, Phys. Rev. **72**, 183 (1947).

WASHINGTON, February 11, 1954.

U. S. GOVERNMENT PRINTING OFFICE: 1955

Recent Publications of the National Bureau of Standards

Journal of Research of the National Bureau of Standards, volume **54**, number 3, March 1955 (RP2572 to RP2578 incl.). Annual subscription $4.00.

Technical News Bulletin, volume **39**, number 3, March 1955. 10 cents. Annual subscription $1.00.

CRPL–127. Basic Radio Propagation Predictions for June 1955. Three months in advance. Issued March 1955. 10 cents. Annual subscription $1.00.

Research Papers

Journal of Research, volume 54, number 3, March 1955. Single copies of the Journal vary in price. Single copies of Research Papers appearing in the Journal are not available for sale. The Superintendent of Documents, U. S. Government Printing Office, Washington 25, D. C., will reprint 100 or more copies of a Research Paper. Request for the purchase price should be mailed promptly to that office.

RP2572. A method for the numerical integration of differential equations of second order without explicit first derivatives. Rene de Volgelaere.

RP2573. Selected positive and negative ions in the mass spectra of the monohalomethanes. Vernon H. Dibeler and Robert M. Reese.

RP2574. Variation in distortion with magnification. Arthur A. Magill.

RP2575. Heats of combustion and isomerization of six pentadienes and spiropentane. Frances Maron Fraser and Edward J. Prosen.

RP2576. Solid-state reactions and dielectric properties in the system magnesia-lime-tin oxide-titania. L. W. Coughanour, R. S. Roth, S. Marzullo, and F. E. Sennett.

RP2577. Chromatographic method for the fractionation of asphalt into distinctive groups of components. Lawrence R. Kleinschmidt.

RP2578. Nature of stark rubber. Donald E. Roberts and Leo Mandelkern.

Applied Mathematics Series

AMS42. Experiments in computation of conformal maps. 40 cents.

Circular

C539. Vol. IV. Standard X-ray diffraction powder patterns. H. E. Swanson, Ruth Fuyat, and G. M. Ugrinic. 45 cents.

Publications in Other Journals

Capacity of plumbing stacks. Robert S. Wyly and Herbert N. Eaton. The Plumber and J. of Heating (32 Finsbury Sq., London, E. C. 2.) **76**, No. 912, 26 (Jan. 1955).

The preparation of some aryl silanes. M. Maienthal, M. Hellmann, C. P. Haber, L. A. Hymo, S. Carpenter, and A. J. Carr. J. Am. Chem. Soc. (1155 16th St. NW., Washington 6, D. C.) **76**, 6392 (1954).

Pyrolysis of α- and β-deuterostyrene polymers. L. A. Wall, D. W. Brown, and V. E. Hart. J. Polymer Sci (250 5th Ave., New York 1, N. Y.) **15**, No. 79, 157 (1955).

Geographic and temporal distribution of Polar blackouts. Vaughn Agy. J. Geophys. Res. (The Johns Hopkins Press, Baltimore 18, Md.) **59**, No. 4, 499 (1954).

Plate separation requirements for standard free-air ionization chambers. Frank H. Attix and LeRoy DeLaVergne. Radiology (713 E. Genesee St., Syracuse 2, N. Y.) **63**, No. 6, 853 (Dec. 1954).

Viscometric and turbidimetric measurements on dilute aqueous solutions of a nonionic detergent. L. M. Kushner and W. D. Hubbard. J. Phys. Chem. (1155 16th St. NW., Washington 6, D. C.) **58**, 1163 (1954).

The International geophysical year, a progress report. Joseph Kaplan and Alan H. Shapley. News Report (National Academy of Sciences, Constitution Ave. NW., Washington 25, D. C.) **4**, No. 6, 1 (Nov.–Dec. 1954).

Thick target bremsstrahlung spectra for 1.00-, 1.25-, and 1.40-Mev electrons. William Miller, J. W. Motz, and Carmen Cialella. Phys. Rev. (57 E. 55th St., New York 22, N. Y.) **96**, No. 5, 1344 (Dec. 1954).

Color and turbidity of sugar products. R. W. Liggett and Victor R. Deitz. Advances in Carbohydrate Chem. (Academic Press Inc., 125 E. 23d St., New York 10, N. Y.) **9**, 247 (1954).

Weights and measures approval seals. M. W. Jensen. Scale J. (1241 Broadway, Hamilton, Ill.) **41**, No. 5, 2 (Feb. 1955).

Publications for which a price is indicated are available only from the Superintendent of Documents, U. S. Government Printing Office, Washington 25, D. C. (foreign postage, one-third additional). Reprints from outside journals are not available from the National Bureau of Standards but can often be obtained from the publishers.

UNITED STATES
GOVERNMENT PRINTING OFFICE
DIVISION OF PUBLIC DOCUMENTS
WASHINGTON 25, D. C.

OFFICIAL BUSINESS

PENALTY FOR PRIVATE USE TO AVOID PAYMENT OF POSTAGE, $300 (GPO)

Journal of Research of the National Bureau of Standards Vol. 54, No. 5 May 1955

Contents

		Page
Astigmatism of skew pencils in optical systems containing toric surfaces. Walter Weinstein.	RP2586	251
Osculatory interpolation in the complex plane. Herbert E. Salzer.	RP2587	263
Macromethods for reducing aldonic lactones to sugars: The preparation of L-glucose. Harriet L. Frush and Horace S. Isbell.	RP2588	267
Stress-strain relationships in yarns subjected to rapid impact loading: 1. Equipment, testing procedure, and typical results. Walter K. Stone, Herbert F. Schiefer, and George Fox.	RP2589	269
Stress-strain relationships in yarns subjected to rapid impact loading: 2. Breaking velocities, strain energies, and theory neglecting wave propagation. Frank L. McCrackin, Herbert F. Schiefer, Jack C. Smith, and Walter K. Stone.	RP2590	277
Waterdrop collisions with solid surfaces. Olive G. Engel.	RP2591	281
Effect of Darling-Dennison and Fermi resonance on the thermodynamic functions. Harold W. Woolley.	RP2592	299

Single copies of the above Research Papers are not available for sale, but the Superintendent of Documents, U. S. Government Printing Office, Washington 25, D. C., will reprint 100 or more copies, and request for the purchase price should be mailed promptly to that office.

For sale by the Superintendent of Documents, U. S. Government Printing Office, Washington 25, D. C. Price 60 cents (single copy) Subscription Price: $4.00 a year; $1.25 additional for foreign mailing. Single copies vary in price.

UNITED STATES GOVERNMENT PRINTING OFFICE, WASHINGTON : 1955